

# Experimental and CFD Studies of Coolant Flow Mixing within Scaled Models of the Upper and Lower Plenums of NGNP Gas-Cooled Reactors

---

Reactor Concepts  
Research Development and Demonstration

Yassin Hassan  
Texas A&M University

Steven Reeves, Federal POC  
Carl Stoots, Technical POC

## FINAL REPORT

**Title:** Experimental and CFD Studies of Coolant Flow Mixing within Scaled Models of  
the Upper and Lower Plenums of NGNP Gas-Cooled Reactors

Covering Period September 1, 2012 to September 1, 2015

Date of Report: March 30, 2016

Recipient: Texas A&M University

Project Number: 12-3759

Principal Investigators: Yassin Hassan: y-hassan@tamu.edu

Co-PI's: NK Anand (TAMU), James Wolf (INL).

**Objectives:** The goal of this project is to investigate the fundamental physical phenomena associated with internal coolant flow in a prismatic core VHTR vessel during normal operation and under accident scenarios. Previous studies have revealed the importance of complex jet/plume flows in each plenum, with potential to generate recirculation zones that can lead to formation of hot spots within the lower plenum. It is therefore of interest to ensure that adequate mixing is promoted, but the complexity of the internal flow fields (characterized by structures spanning multiple orders of magnitude in time and length scales) makes rational design challenging. These difficulties are further compounded by limited availability of data for validation of predictive models.

Here we propose to overcome these limitations by uniquely combining state-of-the-art experimental and computational capabilities of the project team. Experimentally, a geometrically scaled test facility incorporating a faithful 3D representation of the prismatic core VHTR vessel upper and lower plenum will be constructed to overcome difficulties encountered in previous attempts to capture the complex flow field using configurations incorporating a symmetry plane. This facility will be supplemented by the use of innovative high-speed high-resolution imaging capabilities that enable the multiscales of fluid motion (velocity and temperature) to be probed with unprecedented spatial and temporal resolution. Computationally, we will employ the use of high performance cluster computing to simulate the flows using advanced computational fluid dynamics (CFD) techniques to capture the velocity and temperature fields, both globally and locally in recirculation zones. Current modeling approaches typically rely on multi-scale averaging processes that impose serious constraints when unsteady phenomena must be captured. This limits the ability of commercial CFD codes to capture unsteady turbulence multiscales encountered here. We will deal with these complexities by employing large eddy simulation (LES) methods that enable large scales of motion to be directly calculated while finer scales are characterized by a physics-based model.

## EXECUTIVE SUMMARY

A 1/16th scaled VHTR experimental model was constructed and the preliminary test was performed in this study. To produce benchmark data for CFD validation in the future, the facility was first run at partial operation with five pipes being heated. PIV was performed to extract the vector velocity field for three adjacent naturally convective jets at statistically steady state. A small recirculation zone was found between the pipes, and the jets entered the merging zone at 3 cm from the pipe outlet but diverged as the flow approached the top of the test geometry. Turbulence analysis shows the turbulence intensity peaked at 41-45% as the jets mixed. A sensitivity analysis confirmed that 1000 frames were sufficient to measure statistically steady state. The results were then validated by extracting the flow rate from the PIV jet velocity profile, and comparing it with an analytic flow rate and ultrasonic flowmeter; all flow rates lie within the uncertainty of the other two methods for Tests 1 and 2. This test facility can be used for further analysis of naturally convective mixing, and eventually produce benchmark data for CFD validation for the VHTR during a PCC or DCC accident scenario.

Next, a PTV study of 3000 images (1500 image pairs) were used to quantify the velocity field in the upper plenum. A sensitivity analysis confirmed that 1500 frames were sufficient to precisely estimate the flow. Subsequently, three (3, 9, and 15 cm) Y-lines from the pipe output were extracted to consider the output differences between 50 to 1500 frames. The average velocity field and standard deviation error that accrued in the three different tests were calculated to assess repeatability. The error was varied, from 1 to 14%, depending on Y-elevation. The error decreased as the flow moved farther from the output pipe. In addition, turbulent intensity was calculated and found to be high near the output. Reynolds stresses and turbulent intensity were used to validate the data by comparing it with benchmark data. The experimental data gave the same pattern as the benchmark data.

A turbulent single buoyant jet study was performed for the case of LOFC in the upper plenum of scaled VHTR. Time-averaged profiles show that 3,000 frames of images were sufficient for the study up to second-order statistics. Self-similarity is an important feature of jets since the behavior of jets is independent of Reynolds number and a sole function of geometry. Self-similarity profiles were well observed in the axial velocity and velocity magnitude profile regardless of  $z/D$  where the radial velocity did not show any similarity pattern. The normal components of Reynolds stresses have self-similarity within the expected range. The study shows that large vortices were observed close to the dome wall, indicating that the geometry of the VHTR has a significant impact on its safety and performance. Near the dome surface, large vortices were shown to inhibit the flows, resulting in reduced axial jet velocity. The vortices that develop subsequently reduce the Reynolds stresses that develop and the impact on the integrity of the VHTR upper plenum surface. Multiple jets study, including two, three and five jets, were investigated

## **List of publications**

Kyle L. McVay, Jae-Hyung Park, Saya Lee, Yassin A. Hassan, N. K. Anand. "Preliminary Tests of Particle Image Velocimetry for the Upper Plenum of a Scaled Model of a Very High Temperature Gas Cooled Reactor." Progress in Nuclear Energy, (2015)

### **Refereed Conference Publications**

Jae Hyung Park, Anas Alwafi, Saya Lee, Yassin A. Hassan, N. K. Anand. "Particle Image Velocimetry on a Single Buoyant Plume of the Very High Temperature Gas-Cooled Reactor," 2015 the American Nuclear Society (ANS) Winter Meeting, Washington, DC, USA, November 8-12, (2015)

Anas Alwafi, Jae Hyung Park, Saya Lee, Carlos Estrada-Perez, N. K. Anand, Yassin A. Hassan. "Study of the Flow at the Upper Plenum of a Scaled VHTR using PTV," 17th International Conference on Emerging Nuclear Energy Systems (ICENES) 2015, Istanbul, Turkey, October 4-8, (2015)

Jae Hyung Park, Kyle L. McVay, Saya Lee, Yassin A. Hassan, N. K. Anand. "Experimental Design and Flow visualization for the Upper Plenum of a Scaled VHTR," The 10th International Tropical Meeting on Nuclear Thermal-Hydraulics, Operation and Safety (NUTHOS-10), Okinawa, Japan, December 14-18, (2014)

Kyle L. McVay, Jae Hyung Park, Saya Lee, Yassin A. Hassan, N. K. Anand. "An Experimental Study of Coolant Flow Mixing within Scaled Model of the Upper Plenum of VHTR," 2014 the American Nuclear Society (ANS) Winter Meeting, Anaheim, CA, USA, November 9-13, (2014)

Saya Lee, Kyle L. McVay, Jae Hyung Park, Yassin A. Hassan, N. K. Anand, "Measurement of Velocity Field in the Upper Plenum of a Scaled VHTR under PCC condition using PIV," 7th International Topical Meeting on High Temperature Reactor Technology (HTR2014), Weihai, China, October 27-31, (2014)

## **List of Thesis and Dissertations**

Kyle McVay, Experimental Design and Flow Visualization for the Upper Plenum of a Very High Temperature Gas Cooled Reactor for Computer Fluid Dynamics Validation", Master Thesis August 2014 (see Attachment 1)

Anas Mohammed Alwafi, Investigation of the Flow of the Upper Plenum of Scaled Very High Temperature Gas Cooled Reactor during a Depressurization Cooldown Conduction Accident", Master Thesis December 2015.

Jae Hyung Park, Studies of Natural Circulation in a Scaled Model of a VHTR Upper Plenum in the Event of LOFC", PhD Dissertation, In progress.



## **Acknowledgement**

Dr. Richard Schultz contributed to the scaling analysis of this project.

## NOMENCLATURE

$A_{\text{Coolant}}$	Coolant channel flow area (m <sup>2</sup> )
$c_p$	Specific heat capacity (J/kg·K)
$D_{\text{Hole}}$	Coolant channel diameter (m)
$D_{\text{CID}}$	Core barrel inner diameter (m)
$D_m$	Model hydraulic diameter (m)
$D_p$	Prototype hydraulic diameter (m)
$D_{\text{RV}}$	Reactor vessel inner diameter (m)
$d$	Pipe outlet diameter (m)
$g$	Gravity (m/s <sup>2</sup> )
$L_{\text{CB}}$	Bottom of the core (m)
$L_{\text{CT}}$	Top of the core (m)
$L_{\text{H}}$	Height of upper plenum (m)
$L_{\text{RB}}$	Bottom of the lower reflector (m)
$L_{\text{RT}}$	Top of the upper reflector (m)
$L_{\text{T}}$	Top of the upper plenum shield (m)
$n$	Maximum number of points in the PIV field ( $i, j$ )
$N$	Number of frames (number)
$N_{\text{coolant}}$	Number of coolant channels (number)
$M$	Number of tests (number)
$m$	Test number

$\dot{m}$	Mass flow rate (kg/s)
P	Coolant channel pitch (m)
P/D <sub>Hole</sub>	Pitch-to-Diameter ratio
$Q$	Heat input to core piping (W)
$r$	location vector (m)
Re	Reynolds number ( $= DV / \nu$ )
Ri	Richardson number ( $= g\alpha\Delta TD / V^2$ )
S	Jet spacing (m)
$T_i$	Temperature at core inlet (K)
$T_o$	Temperature at core outlet (K)
$\Delta T$	Temperature gradient ( $= T_o - T_i$ ) (K)
$\Delta t$	Time interval of successive images (s)
TI	Turbulence intensity ( $= v_{rms} / \bar{v}^N$ )
$u$	x-velocity (m/s)
$V_m$	Model velocity (m/s)
$V_p$	Prototype velocity (m/s)
$v$	y-velocity (m/s)
$\mathbf{v}$	velocity vector (m/s)
$v'$	Turbulent fluctuations of y-velocity (m/s)
$v_{ave}$	Average y-velocity between the Tests (m/s)
$v_{rms}$	Turbulence strength in y direction averaged between the Tests (m/s)

$\bar{v}^N$	Average y-velocity for $N$ frames (m/s)
$\Delta X$	Displacement of particle images (px)
$\alpha$	Magnification factor (mm/px)
$\beta$	Thermal expansion coefficient (1/K)
$\delta u$	Experiment uncertainty factor (mm/s)
$\xi_{\dot{m}}$	Mass flow rate uncertainty (kg/s)
$\sigma_{T_i}$	Thermocouple error at core inlet (K)
$\sigma_{T_o}$	Thermocouple error at core outlet (K)
$\rho$	Density of fluid (kg/m <sup>3</sup> )
$\rho_0$	Reservoir fluid density (kg/m <sup>3</sup> )
$\Delta\rho$	Density fluctuation ( $= \rho - \rho_0$ ) (kg/m <sup>3</sup> )
$\omega$	Vorticity ( $= \partial v / \partial x - \partial u / \partial y$ ) (1/s)
$\nu_m$	Model kinematic viscosity (m <sup>2</sup> /s)
$\nu_p$	Prototype kinematic viscosity (m <sup>2</sup> /s)

#### Subscripts

m	Model
p	Prototype

#### Acronyms

CFD	Computational Fluid Dynamics
DCC	Depressurized Conduction Cooldown
DOE	Department of Energy
FOV	Field of View
GIF	Generation IV International Forum
IEA	International Energy Agency
INEEL	Idaho National Engineering and Environmental Laboratory
INL	Idaho National Laboratory
LOCA	Loss of Coolant Accident
LOFA	Loss of Flow Accident
MHTGR	Modular High Temperature Gas-Cooled Reactor
NGNP	Next Generation Nuclear Plant
NRC	Nuclear Regulatory Commission
P2P	Plenum-to-Plenum
PCC	Pressurized Conduction Cooldown
PIRT	Phenomena Identification and Ranking Table
RCCS	Reactor Cavity-Cooling System
ROI	Region of Interest
RT	Rayleigh-Taylor
V&V	Verification and Validation
VHTR	Very High Temperature Reactor

## TABLE OF CONTENTS

	Page
NOMENCLATURE.....	II
TABLE OF CONTENTS .....	XI
LIST OF FIGURES.....	XIII
LIST OF TABLES .....	XVII
1. INTRODUCTION.....	1
1.1 Research Objectives .....	12
2. EXPERIMENTAL TEST FACILITY.....	14
2.1 The Very High Temperature Reactor .....	14
2.2 Scaling and Design .....	17
2.3 Fabrication and Construction.....	26
3. PRELIMINARY TEST .....	35
3.1 Experiment Method .....	35
3.2 Sensitivity Analysis .....	40
3.3 Experiment Result .....	50
3.4 CFD Validation.....	57
3.5 Summary.....	59
4. EXPERIMENT MODIFICATION .....	61
5. A SINGLE BUOYANT JET STUDY.....	66
5.1 Turbulent Vertical Buoyant Jet.....	67
5.2 Scaling of Mixing of Jet Flows entering the Upper Plenum .....	74
5.3 Experiment Method .....	76
5.4 Experiment Result .....	85
6. CONCLUTION AND FUTURE WORK.....	96
REFERENCES.....	97

APPENDICES .....	100
APPENDIX A    FACILITY DRAWINGS AND FIGURES.....	1

## LIST OF FIGURES

	Page
<b>Figure 1.1.</b> World primary energy consumption grew. X-axis=year; Y-axis=million tonnes oil equivalent [1]. .....	2
<b>Figure 1.2.</b> Nuclear energy consumption by region (TWh). X-axis represents year [1]. .....	2
<b>Figure 1.3.</b> Growth in nuclear power capacity and its share of global electricity production [2]. .....	3
<b>Figure 1.4.</b> Evolution of fission reactor technology [2]. .....	5
<b>Figure 1.5.</b> Schematics of Very High Temperature Reactor (VHTR) [5]. .....	6
<b>Figure 1.6.</b> MHTGR module (DOE 1986). .....	7
<b>Figure 1.7.</b> A typical prismatic VHTR concept: internal structure, core, control rod guide tubes [modified from KAERI]. .....	8
<b>Figure 1.8.</b> A validation pyramid approach [6]. .....	10
<b>Figure 1.9.</b> Thermal hydraulic phenomena experiment planning [6]. .....	11
<b>Figure 2.1.</b> Water flow natural circulation apparatus configured for the study of DCC event. ....	19
<b>Figure 2.2.</b> Water flow natural circulation apparatus configured for the study of PCC event. ....	19
<b>Figure 2.3.</b> Experimental facility schematic. ....	23
<b>Figure 2.4.</b> Core piping. ....	24
<b>Figure 2.5.</b> Cooling jacket design. ....	25
<b>Figure 2.6.</b> Exploded assembly cross section. ....	28
<b>Figure 2.7.</b> Thermocouple with tubing, epoxy, and ferrules (top) and its location for the temperature measurement inside the steel tubing (bottom). ....	29
<b>Figure 2.8.</b> Particle images for PIV with black and white inversion. ....	31
<b>Figure 2.9.</b> Optical distortion test. ....	32



<b>Figure 2.10.</b> Assembly procedure of the test facility: (a) upper plenum with the correction box, (b) internal core top view, (c) outer containment being lowered by a forklift, (d) 25 coolant channel pipes with heating tapes and thermocouples, (e) silicon tubings and core assembly, and (f) core insulation.	33
<b>Figure 2.11.</b> Completed test facility	34
<b>Figure 2.12.</b> Schematic view of facility	34
<b>Figure 3.1.</b> PIV schematic.	37
<b>Figure 3.2.</b> Analysis window geometry.	37
<b>Figure 3.3.</b> Flowmeter calibration line.	39
<b>Figure 3.4.</b> Velocity magnitude contour of 1,000 frames.	42
<b>Figure 3.5.</b> Streamline of 1,000 frames.	42
<b>Figure 3.6.</b> x-velocity contour of 1,000 frames.	43
<b>Figure 3.7.</b> y-velocity contour of 1,000 frames.	43
<b>Figure 3.8.</b> Vorticity contour and average velocity vector of 1,000 frames.	44
<b>Figure 3.9.</b> Percent error of y-velocity for different batch sizes of frames.	44
<b>Figure 3.10.</b> Test 1 sensitivity analysis at 3 cm from pipe outlet.	47
<b>Figure 3.11.</b> Test 2 sensitivity analysis at 3 cm from pipe outlet.	47
<b>Figure 3.12.</b> Test 1 sensitivity analysis at 7 cm from pipe outlet.	48
<b>Figure 3.13.</b> Test 2 sensitivity analysis at 7 cm from pipe outlet.	48
<b>Figure 3.14.</b> Test 1 sensitivity analysis at 11 cm from pipe outlet.	49
<b>Figure 3.15.</b> Test 2 sensitivity analysis at 11 cm from pipe outlet.	49
<b>Figure 3.16.</b> Average y-velocity at 3 cm from the pipe outlet with standard deviation between the tests.	51
<b>Figure 3.17.</b> Averaged turbulence strength at 3 cm from the pipe outlet with standard deviation between the tests.	51

<b>Figure 3.18.</b> Flow rate for a single pipe with different methods. ....	54
<b>Figure 3.19.</b> PIV and CFD comparison at different vertical location (a) each vertical location for the line extraction from the pipe outlet at, (b) 3 cm, (c) 7 cm, and (d) 11 cm for four cases. ....	58
<b>Figure 4.1.</b> The procedure of the repair process of the heating tapes and extension wires. (a) Damaged wires were burned due to a short circuit. This caused the heating tapes disconnected. (b) A transparent shrink tubing was installed to protect each individual wires. (c) An orange high temperature shrink tubing was installed to enhance the thermal barrier to the wire connections. ....	62
<b>Figure 4.2.</b> Surge protectors and variable voltage transformers. ....	62
<b>Figure 4.3.</b> The blackout window curtains with the double pulse laser, high speed camera, and modeled VHTR inside. (a) When curtains are opened (b) closed. ....	63
<b>Figure 4.4.</b> Fluorescent orange particle recycle system. (a) A pump connected with an exit hose from the test facility and stainless steel frame sieve. (b) A zoom in view of the sieve after collecting particles. ....	64
<b>Figure 4.5.</b> Overview of PIV laser system. ....	65
<b>Figure 5.1.</b> Buoyant jets in uniform surroundings [33]. ....	68
<b>Figure 5.2.</b> A cylindrical coordinate system and nomenclature. ....	71
<b>Figure 5.3.</b> Turbulent buoyant jet mixing. ....	75
<b>Figure 5.4.</b> Experiment test facility: 1/16 <sup>th</sup> scaled VHTR with the upper plenum. The PIV laser system with the high speed camera. The system inlet/outlet pipe lines. The water reservoir. ....	76
<b>Figure 5.5.</b> VHTR test cross section view. ....	77
<b>Figure 5.6.</b> Schematic of PIV laser and camera system. The origin of a cylindrical coordinate system is located at the center of the pipe outlet. ....	78
<b>Figure 5.7.</b> Schematics of the test section (solid and dotted line) and region of interest (solid line). ....	78
<b>Figure 5.8.</b> Real time experiment image (top) with the green laser sheet and orange fluorescent particles and filtered image (bottom) after the polarizer and orange bandpass filter in the field of view (red box). The color of orange fluorescent particles is orange (top) and white (bottom). ....	79

<b>Figure 5.9.</b> Pipe layout, test section and a center pipe (C1) plan view. ....	80
<b>Figure 5.10.</b> Experiment test procedure for PIV. ....	82
<b>Figure 5.12.</b> Contours of averaged single buoyant jet; (a) mean radial velocity; (b) mean axial velocity; (c) mean velocity magnitude with streamlines; (d) vorticity ( $\omega$ ). ....	87
<b>Figure 5.13.</b> Contours of averaged single buoyant jet; (a) standard deviation of radial velocity; (b) standard deviation of axial velocity; (c) Reynolds stress $\langle u' u' \rangle$ ; (d) Reynolds stress $\langle w' w' \rangle$ ; (e) Reynolds stress $\langle u' w' \rangle$ . ....	88
<b>Figure 5.14.</b> Contours of averaged single buoyant jet; (a) Turbulent kinetic energy ( $k$ ); (b) turbulent viscosity ( $\nu_t$ ); (c) turbulent intensity in radial direction; (d) turbulent intensity in axial direction. ....	89
<b>Figure 5.15.</b> Time series of temperature at location $r = 0$ cm, $z = -2.54$ cm in Test 8. The passage of 7 puff cycles is observed.....	90
<b>Figure 5.16.</b> The axial velocity distribution along the $z$ -direction at $r = 0$ cm. The maximum velocity is obtained at $z = 12.51$ cm. ....	90
<b>Figure 5.17.</b> Temperature data at each location for nine test results and averaged temperature data.....	91
<b>Figure 5.18.</b> Flowrate data at each location for nine test results and averaged flowrate data.....	91
<b>Figure 5.19.</b> The characteristics of a single buoyant jet. (a) jet boundary, (b) entrainment coefficient, and (c) speeding rate. The orange line indicates the left-hand side value while the blue line represents the right-hand side value. .	92
<b>Figure 5.23.</b> Radial profiles of non-dimensional (a) radial velocity, (b) axial velocity, (c) velocity magnitude within a single buoyant jet.....	94
<b>Figure 5.24.</b> Radial profiles of non-dimensional Reynolds stresses ((a) - (c)) within a single buoyant jet. ....	95

## LIST OF TABLES

	Page
<b>Table 1.1.</b> Key operating parameters for the MHTGR [6]. .....	7
<b>Table 2.1.</b> Dimensions of scaled VHTR geometry provided by INL and nomenclature. .....	18
<b>Table 3.1.</b> Flow rate uncertainties. ....	54
<b>Table 3.2.</b> Summary of PIV system uncertainties from VSJ method. ....	56
<b>Table 5.1.</b> PIV camera and laser test conditions. ....	81
<b>Table 5.2.</b> PIV computation settings. ....	81
<b>Table 5.3.</b> Dimensionless numbers of the present test condition .....	84

## 1. INTRODUCTION

Energy is the “ability of a system to perform work.” We use this energy to drive a car, cook a fancy dinner, run machines in a large factory, and do various other activities. There are numerous forms of energy such as chemical energy, mechanical energy, nuclear energy, thermal and heat energy. People in the world use these forms of energy constantly increasing the consumption/production rate every year (Figure 1.1). According to the ‘BP Statistical Review of World Energy June 2015 [1],’ global primary energy consumption increased by 0.9% in 2014. It was reported that the nuclear power was the only fuel to grow at an above-average rate (1.8%), which is significantly faster than the 10-year average of 0.8% (Figure 1.2). This was the second consecutive annual increase in nuclear power use and the first time it has gained global market share since 2009. In addition, consumption increased for all fuel types except nuclear power. Still, most of the world’s primary energy consumption comes from oil (most dominant), coal and natural gas. However, these fuel types emit significant amounts of carbon dioxide ( $\text{CO}_2$ ) while nuclear power produces almost no greenhouse gases and is considered form of clean, sustainable energy.

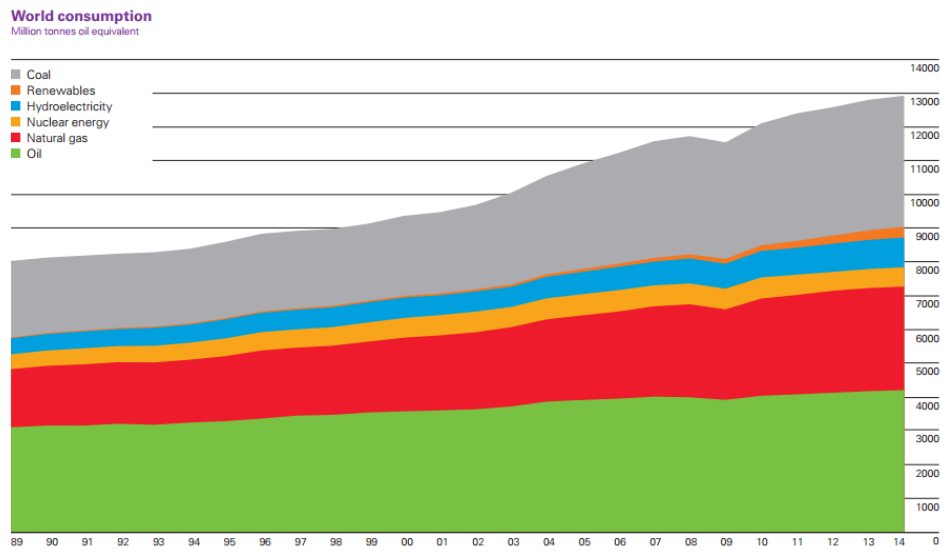


**Figure 1.1.** World primary energy consumption grew. X-axis=year; Y-axis=million tonnes oil equivalent [1].

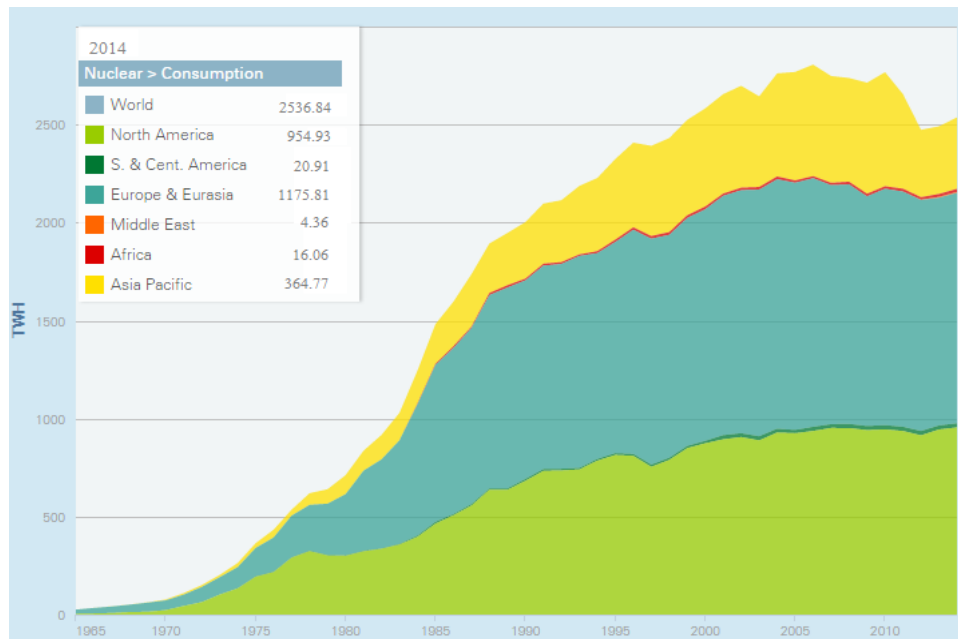


**Figure 1.2.** Nuclear energy consumption by region (TWh). X-axis represents year [1].

The gross US electricity generation was 4,092 TWh (million MWh) in 2014 according to International Energy Agency (IEA) data report where the dependency on nuclear power was 19.47% (797 TWh). Annual electricity demand is expected to increase to 5,000 TWh in 2030 with a corresponding increase in nuclear power. Today, 16 countries depend on nuclear power for at least 25% of its total electricity. IEA released a technology roadmap for nuclear energy in 2015 which provided the future vision of nuclear power deployment up to 2050 [2] (Figure 1.3). According to the report, growth in nuclear power capacity and its share of global electricity production continuously increases, reaching 1,200 GW in 2050 with annual electricity production of nearly 10,000 TWh. One of the key milestones during the next 10 years is to demonstrate the ability to build the latest nuclear plant designs on time and within budget where the regional investment needs for nuclear power from 2010 to 2050 are 883 USD bn for US and Canada, and 893 USD bn for China.

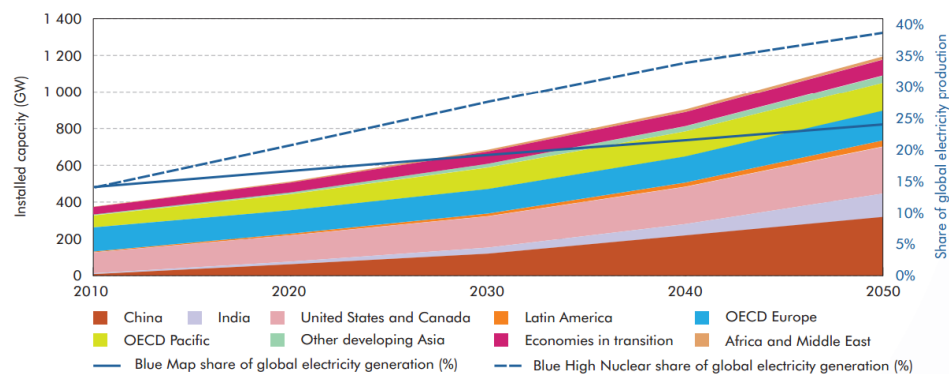


**Figure 1.3.** Growth in nuclear power capacity and its share of global electricity production [2].

In the near future, the US and other industrialized countries will need larger energy resources and an upgraded energy infrastructure to meet constant increasing demands for electricity. The Generation IV International Forum (GIF), an international research and development framework of the next generation nuclear energy system, was founded in 2001 by Argentina, Brazil, Canada, France, Japan, the Republic of Korea, South Africa, the United Kingdom and the United States. The goals of the GIF nuclear energy system is required to provide future energy demand as well as meet four goals of sustainability, safety and reliability, superior economics, and proliferation resistance and physical protection [3]. In 2002, GIF selected six nuclear energy systems with nearly 130 reactor concepts for further development as Generation IV technologies: Gas-cooled Fast Reactor (GFR), Lead-cooled Fast Reactor (LFR), Molten Salt Reactor (MSR), Supercritical Water-cooled Reactor (SCWR), Sodium-cooled Fast Reactor (SFR), and Very High Temperature Reactor (VHTR). Commercial construction, deployment, and operation of Generation IV prototypes is expected before 2030 as shown in Figure 1.4. Currently, the US and South Korea are signed to participate in developing SFR and VHTR as a Generation IV reactor.



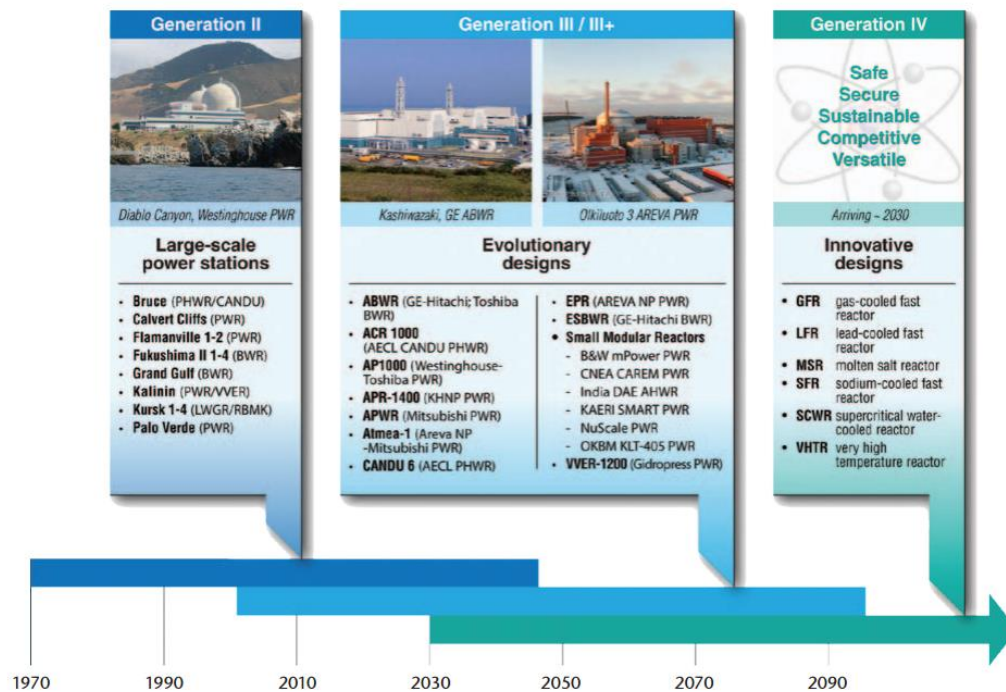
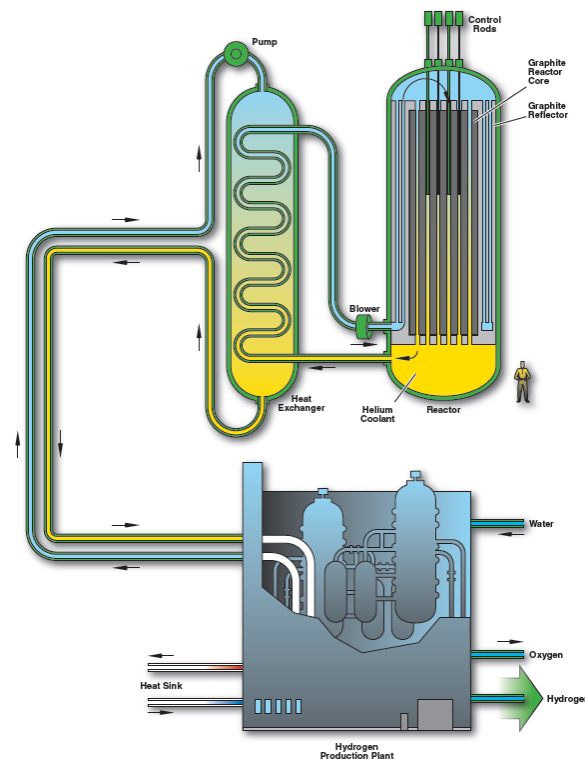


Figure 1.4. Evolution of fission reactor technology [2].

Among those Generation IV reactors, the Department of Energy (DOE) has selected the Very High Temperature Gas Cooled Reactor (VHTR) for the Next Generation Nuclear Power (NGNP) Project. The VHTR refers to any reactor design that has coolant outlet temperatures of at least 1000 °C. As shown in Figure 1.5, it is the one design variation of the high-temperature gas-cooled reactors (HTGRs) [4] (the terms commonly used interchangeably). The HTGR is a graphite-moderated nuclear reactor with a flexible uranium/plutonium fuel cycle using helium as a coolant. The reactor core can be designed either as a prismatic block or a pebble-bed core. The high temperature enables the application of high efficiency electricity production as well as process heat and hydrogen production through the thermochemical sulfur-iodine cycle. The core design inherently enables the safety characteristics of the reactor and an air-cooled Reactor Cavity-Cooling

System (RCCS) provides a passive safety system to remove the decay heat from the reactor vessel. The reference design of the VHTR is a Modular High Temperature Gas-Cooled Reactor (MHTGR) designed by General Atomics. The detail parameters and features of the MHTGR are listed in Table 1.1. Figure 1.6 shows the primary and secondary (steam generator) vessels, and annual reactor core of MHTGR. The Idaho National Engineering and Environmental Laboratory (INEEL) will construct the VHTR as a part of NGNP in the near future. However, the current stage of the development is conceptual and not ready to perform any validation process for computational simulations.



**Figure 1.5.** Schematics of Very High Temperature Reactor (VHTR) [5].

**Table 1.1.** Key operating parameters for the MHTGR [6].

Major Reactor Parameters	MHTGR
Thermal power (MWt)	350
Primary coolant	Helium
Moderator	Graphite
Average power density (MW/m <sup>3</sup> )	5.9
Core inlet temperature/pressure (°C/MPa)	259/6.4
Core outlet temperature/pressure (°C/MPa)	687/6.4
Total temperature rise (°C)	428
Core Geometry	Annular
Safety Design Philosophy	Passive
Fuel Max Temp – Normal Operation (°C)	1250
Fuel Max Temp – Emergency Conditions (°C)	1600

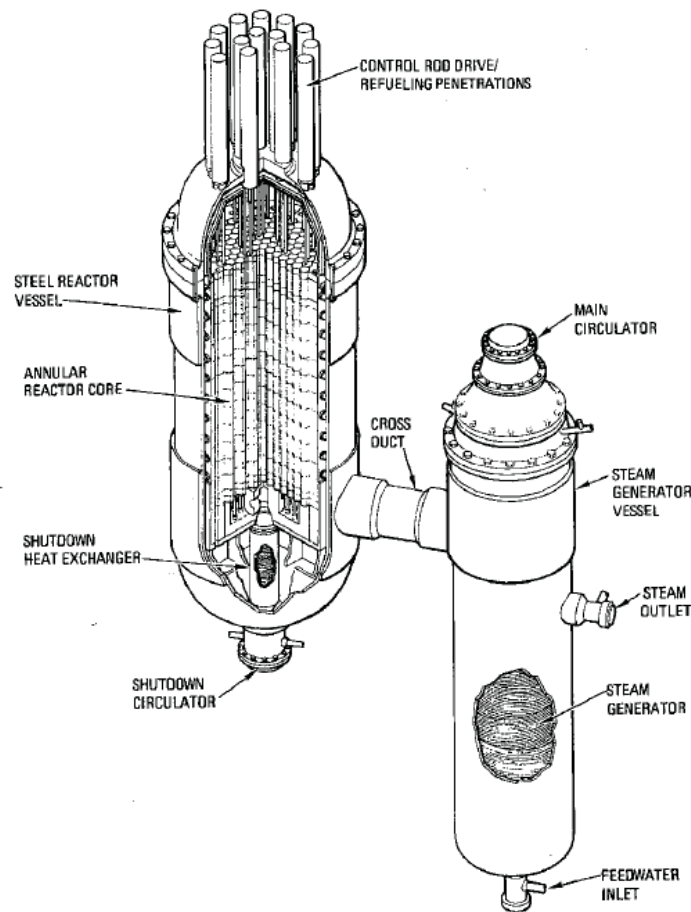


**Figure 1.6.** MHTGR module (DOE 1986).

The primary loop of the VHTR starts from the helium coolant entering the core, proceeding upward to the reactor vessel through an annular passage in the cross duct, and divided into distinct coolant inlet channels that exist between the peripheral duct wall of the core region and the inner diameter of the reactor vessel wall [6]. The helium coolant is redirected in the upper plenum by 180 degrees and enters the annular core and inner and outer reflector region and flows downward. The helium exits into the lower plenum and is gathered into a single stream which flows through the cross duct to the steam generator.

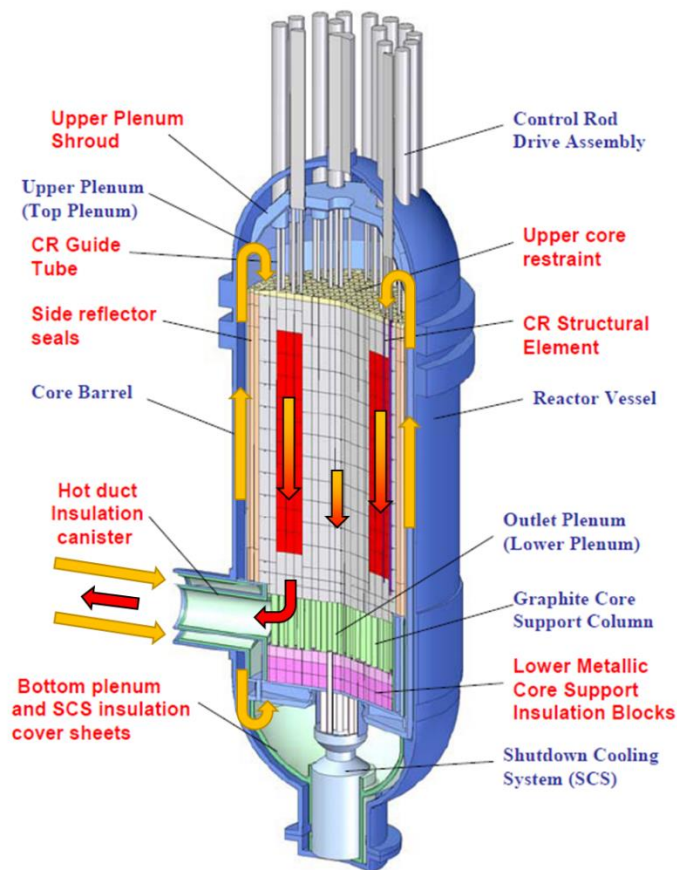


**Figure 1.7.** A typical prismatic VHTR concept: internal structure, core, control rod guide tubes [modified from KAERI].

The Phenomena Identification and Ranking Table (PIRT) provides identification on safety-relevant phenomena associated with the NGNP during normal operations, transients, and postulated accidents. Based on the relative importance of these phenomena and an assessment of the knowledge level, each phenomena is ranked and listed in table. The most important safety-related accident is loss-of-forced-cooling (LOFC) events and is classified into two categories: the Depressurized Conduction Cooldown (DCC) and Pressurized Conduction Cooldown (PCC) event. The PCC event assumes a flow coast-down and scram while the RCCS is operating constantly. Buoyancy forces do not significantly establish helium coolant recirculation while the chimney effect increases the core temperatures near the top. The DCC event assumes a rapid depressurization of the primary coolant and scram with the passive RCCS system operating and assuming no air ingress [7]. Once natural circulation is achieved during the DCC and PCC event, the reversal flow will arise and thermal stresses on the ceiling of the upper plenum and the control rods become a critical concern [8]. To understand how the plume/jet mixing in the upper plenum of the VHTR influences the structure of the reactor and provides for a better reactor design is the purpose of this study.

The experiments performed in this study will provide the validation data for the majority of the challenging accident analysis in the commercial CFD software and system analysis [6]. In general a validation pyramid approach is used for the basis of constructing the NGNP thermal-fluids validation matrix as shown in Figure 1.8. The foundation of the pyramid is made up with validation data from basic experiments designed to study fundamental phenomena which are ideal for the university environment [6]. In other

words, to study complex mixing behavior between numerous gas jets, the study of a single jet and the interaction between two jets should be delivered in advance for a basic experiment as a foundation of the validation pyramid.

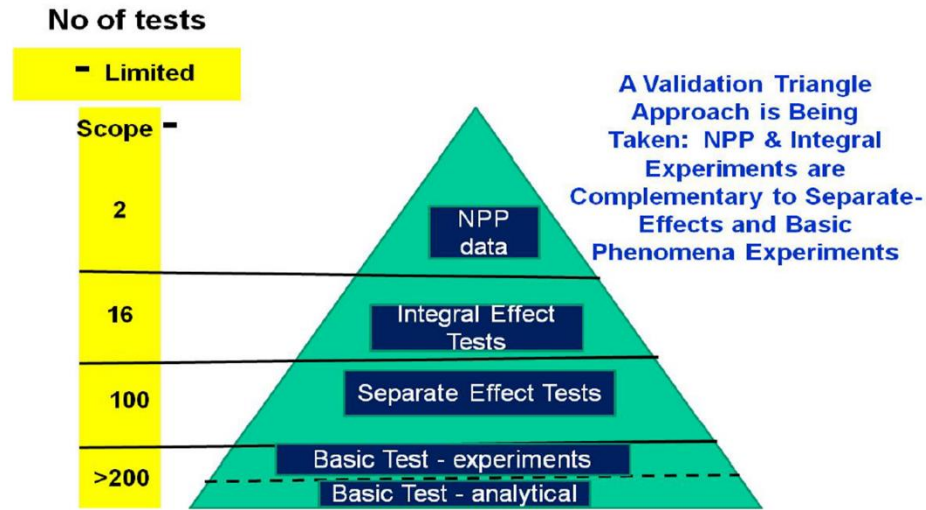


**Figure 1.8.** A validation pyramid approach [6].

The NGNP experimental verification and validation (V&V) program includes thermal-fluids experiments that will be used to provide validation data for systems analysis and Computational Fluid Dynamics (CFD) software for major accident scenarios [6, 9]. As a foundation of the validation pyramid approach, a relatively large number of basic experiments will be performed to better design the reactor system. Several experiment plans are proposed including integral facility, upper/lower plenum experiment, plenum-to-plenum experiment, MIR experiment, and air ingress experiments (Figure 1.9). Among those experiment plans, the study chosen is to design a plenum-to-plenum (P2P)

experiment. This P2P experiment will be used to study the natural convection heat transfer that will occur during the LOFC event.

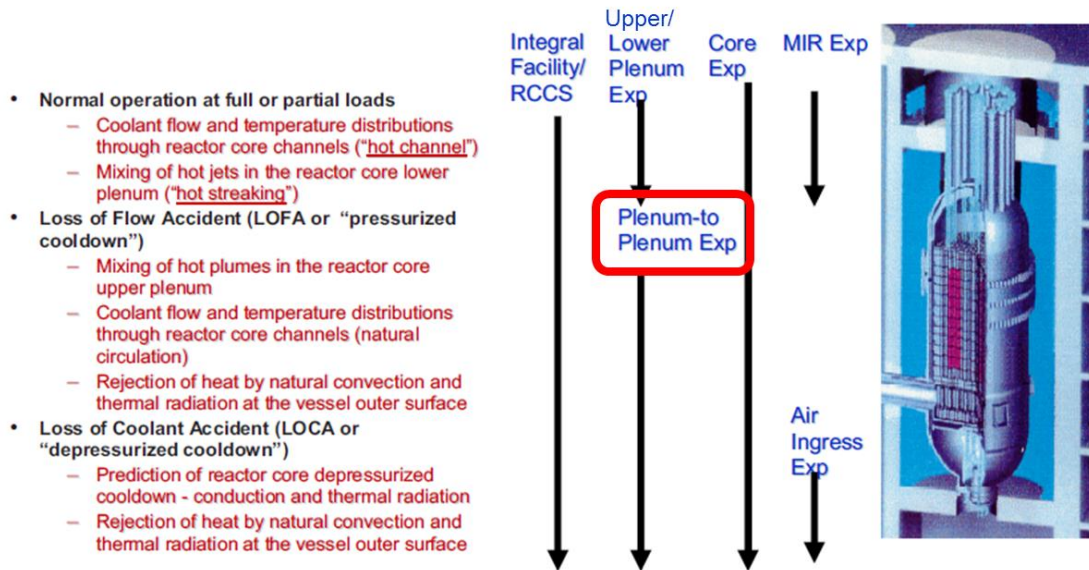


**Figure 1.9.** Thermal hydraulic phenomena experiment planning [6].

The primary goal of Texas A&M University (TAMU) VHTR facility is to perform the experiments to understand the phenomenon during both the PCC and DCC events. Starting from a single jet mixing behavior to the interactions between multiple jets, the P2P experiment will provide a basic understanding of the VHTR accident conditions. The particle image velocimetry (PIV), a non-intrusive optical measurement technique, will be performed to capture the complex behavior of the fluid flow which will happen in the upper plenum of the reactor vessel. The benchmark data will be compared to simulation results to determine the fidelity of particular turbulent models.

## 1.1 Research Objectives

The primary objective of this research is to investigate the fundamental physical phenomena associated with internal coolant flow in a prismatic core VHTR vessel during normal operation and under accident scenarios. Previous studies have revealed the importance of complex jet/plume flows in each plenum, with the potential to generate recirculation zones that can lead to formation of hot spots within the lower plenum. It is therefore of interest to ensure that adequate mixing is promoted, but the complexity of the internal flow fields (characterized by structures spanning multiple orders of magnitude in time and length scales) makes rational design challenging. These difficulties are further compounded by limited availability of data for validation of predictive models.

Here we propose to overcome these limitations by uniquely combining state-of-the-art experimental and computational capabilities of the project team. Experimentally, a geometrically scaled test facility incorporating a faithful 3D representation of the prismatic core VHTR vessel upper and lower plenum will be constructed to overcome difficulties encountered in previous attempts to capture the complex flow field using configurations incorporating a symmetry plane. This facility will be supplemented by the use of innovative high-speed high-resolution imaging capabilities that enable the multiscale of fluid motion (velocity and temperature) to be probed with unprecedented spatial and temporal resolution. Computationally, we will employ the use of high performance cluster computing to simulate the flows using advanced computational fluid dynamics (CFD) techniques to capture the velocity and temperature fields, both globally



and locally in recirculation zones. Current modeling approaches typically rely on multi-scale averaging processes that impose serious constraints when unsteady phenomena must be captured. This limits the ability of commercial CFD codes to capture unsteady turbulence multiscales encountered here. A distinguishing feature of this work will be the unique ability to perform direct cross-validation between experiment and simulation, enabling more accurate and rational prediction of the coolant flow field characteristics than is currently possible.

## **2. EXPERIMENTAL TEST FACILITY**

### **2.1 The Very High Temperature Reactor**

The Very High Temperature Reactor (VHTR) has been selected as one of the Next Generation Nuclear Plant (NGNP). It is an evolved Generation IV gas cooled reactor design that allows for a 1,000 °C coolant outlet temperature [4, 10-12]. The design has high fuel efficiency for electricity generation, and because of the high outlet temperature it is optimal for industrial applications or commercialized hydrogen production [13, 14]. There are two reactor designs being developed; the pebble bed and prismatic VHTR. Many studies are being performed for both normal operation and accident scenarios for both designs. There are two major accident scenarios of interest; Depressurized Conduction Cooldown (DCC), and Pressurized Conduction Cooldown (PCC) [8, 15]. A DCC event involves the depressurization of the main core coolant loop, generally through a Loss of Coolant Accident (LOCA). This results in an air ingress to the lower plenum where it slowly diffuses into the core and oxidizes with the fuel accelerating the heating of the core and releasing fission products [16]. As there is no heat sink for the core the primary heat removal is through radiation, and the core may reach the failure temperature of 1600 °C. In a PCC scenario there is loss of forced coolant but the main loop stays pressurized, this may be a result of a loss of power. During normal operation the helium is circulated into

the upper plenum and down through the core with a blower. Because the loop stays pressurized in a PCC scenario the helium coolant has a high density differential resulting in large buoyancy forces. Over time these forces will overcome the initial inertial forces, reversing the circulation of the coolant to go up through the core into the upper plenum, and down between the reflector and the core. This natural circulation removes sufficient heat from the core so the core will not reach the failing temperature of the fuel, but may cause thermal stresses on the internal support structures in the upper plenum.

There are several nuclear system codes currently being developed as computational tools to conduct performance and safety analyses of the VHTR. Experimental models are needed for the validation of these codes. Idaho National Laboratories (INL) has collaborated with Korean and American universities to develop codes as well as experimental models to validate them [15, 17]. Primarily normal operation and air ingress following a DCC scenario were evaluated. To model this, a multi-dimensional gas mixture analysis code was created to predict chemical reaction and thermo-fluid behaviors for an air ingress following a DCC scenario for both pebble bed and prismatic core designs. The Codes were validated with the water pool Reactor Cavity Cooling System (RCCS) test facility, and an inverse U-tube experiment that modeled the temperature and chemical reaction behavior of a gas mixture. Additionally Oregon State University has constructed a high temperature test facility that can model a VHTR during a DCC accident scenario which can provide benchmark data for existing safety analysis codes [16].

Currently there have been many studies and experimental models evaluating the core and lower plenum for normal operation [9, 12, 18] and DCC accident scenario [8, 16]. There has been CFD analysis for the upper plenum following a PCC Scenario [19]. As there are no experimental models to produce benchmark data for validation, a scaled experimental model of a VHTR is necessary to provide benchmark data in the upper plenum following a DCC or PCC accident scenario. The 1/16<sup>th</sup> scaled test facility constructed in this study can fulfill this deficiency of data. The test facility is a closed loop that uses heated pipes to induce natural circulation through the system without the use of pumps, this may be used to model a DCC event. A pump may be added along with a heat exchanger to simulate a PCC event. Particle Image Velocimetry (PIV) is used to obtain the velocity field in the upper plenum. In order to produce benchmark data, the PIV system must first be validated for simpler test conditions. This study uses PIV to record the turbulent mixing of three adjacent naturally convective jets. The results are validated by comparing the PIV vector field with an ultrasonic flowmeter analytic flow rates.

## 2.2 Scaling and Design

The reference prismatic reactor design is the Modular High Temperature Gas Reactor (MHGTR) designed from General Atomics (GA). Its reactor power is 350 MW and helium inlet/outlet temperatures of 258.6 °C and 687 °C, respectively. The coolant flow rate is 157.05 kg/s and its RCCS heat removal is 0.7 MW. As a part of the plenum to plenum experiment from INL, the current VHTR design is geometrically scaled down (1/16<sup>th</sup> scale) from the MHGTR. Detailed geometrical parameters are listed in Table 2.1. The total number of coolant channels was chosen to be 25 to maintain both the symmetrical hexagonal array pattern and the scale area ratio of the core flow area in the prototype.

The design obtained from INL is shown in Figure 2.1 and 2.2. The experiment facility is capable of operating at both PCC and DCC event under steady-state conditions. The objective of each accident scenario is following:

- 1) During the PCC event experiment, the natural circulation through the loop, i.e. from the reactor vessel to the steam generator and back to the reactor vessel, is investigated.
- 2) During the DCC event, the natural circulation between the reactor vessel and the containment is investigated.
- 3) In both PCC and DCC event, the natural circulation within the reactor vessel only, i.e., natural circulation between the lower and upper plena through the core region, is

investigated. The VHTR test facility is currently assembled to simulate the DCC event, therefore a water reservoir system was installed.

**Table 2.1.** Dimensions of scaled VHTR geometry provided by INL and nomenclature.

Variables	Nomenclature	MHTGR (m)	1/16 <sup>th</sup> scaled VHTR (m)
Bottom of the lower plenum	Reference	-2.88255	0
Bottom of the lower reflector	L <sub>RB</sub>	-1.9825	0.05625
Bottom of the core	L <sub>CB</sub>	0.0	0.18016
Top of the core	L <sub>CT</sub>	7.93	0.6758
Top of the upper reflector	L <sub>RT</sub>	9.516	0.7749
Top of the upper plenum shield	L <sub>T</sub>	12.6656	0.9718
Height of upper plenum	L <sub>H</sub>	3.1496	0.197
Reactor vessel inner diameter	D <sub>RV</sub>	6.534	0.4083 (= 16.07 in)
Core barrel inner diameter	D <sub>CID</sub>	5.95	0.370 (= 14.57 in)
Coolant channel diameter	D <sub>Hole</sub>	0.01588	0.01905 (= 0.75 in)
Number of coolant channels	N <sub>coolant</sub>	11000 5/8 in diameter	25
Coolant channel flow area (m <sup>2</sup> )	A <sub>Coolant</sub>	2.177 (considering only 5/8-in channels)	0.00713
Coolant channel pitch	P	0.0322	0.03861 (= 1.52 in)
Pitch-to-Diameter ratio	P/D <sub>Hole</sub>	2.03	2.03

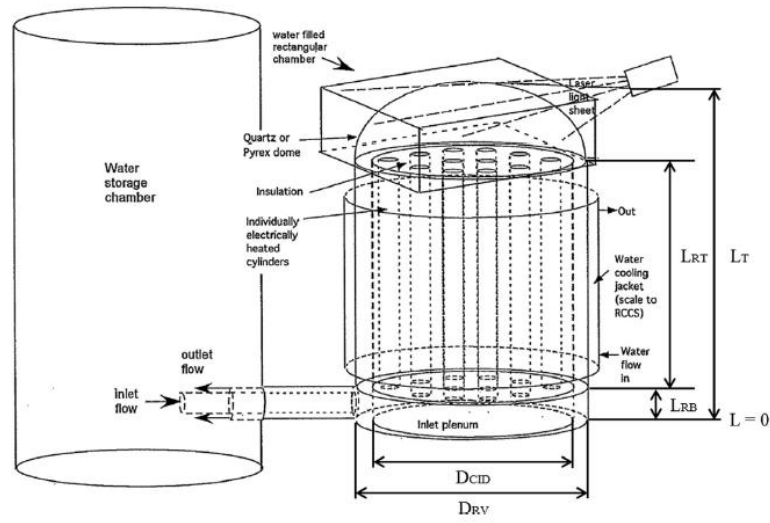


**Figure 2.1.** Water flow natural circulation apparatus configured for the study of DCC event.

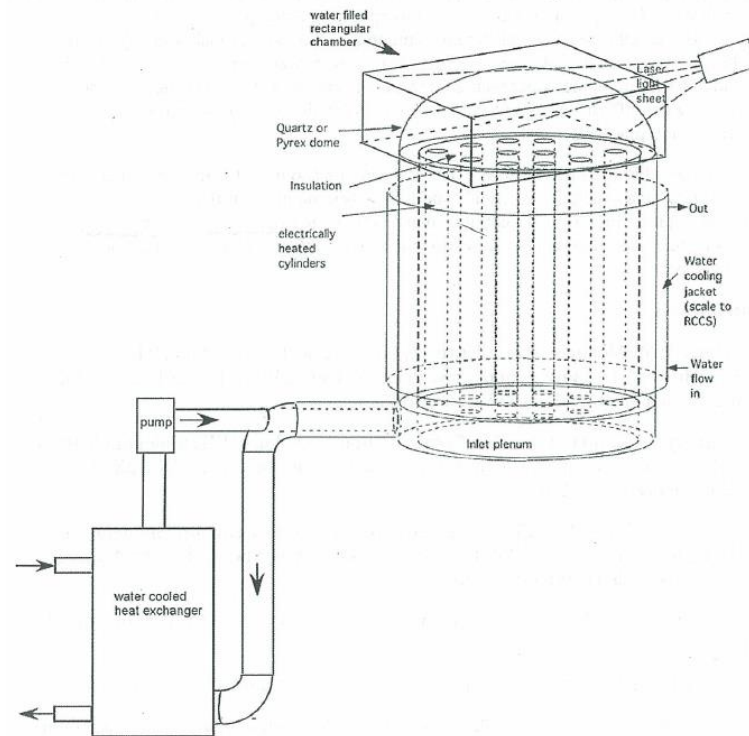


**Figure 2.2.** Water flow natural circulation apparatus configured for the study of PCC event.

This experiment is a preliminary testing of the PIV system, but is designed to have the capabilities to produce benchmark data for DCC and PCC accident scenarios after reaching steady state. The prototype fuel decay heat is modeled with individually electrically heated cylinders. When scaling an experiment to model the natural circulation in the prototype plenums, the main approach is matching the Richardson number (Ri), the ratio of the buoyancy force to inertial force, and the Reynolds number (Re), the ratio of inertial to viscous forces, for the model and the VHTR prototype [14]. This may be achieved once the systems have reached steady state. The Richardson ratio is shown in Equation (2.1).

$$\text{Ri} = \frac{g\beta\Delta TD}{V^2} \rightarrow \frac{\text{Ri}_m}{\text{Ri}_p} = \frac{\left(\frac{\Delta\rho}{\rho}\right)_m \frac{V_p^2 D_m}{V_m^2 D_p}}{\left(\frac{\Delta\rho}{\rho}\right)_p} \quad (2.1)$$

The ratio is currently in terms of density, but the Boussinesq approximation may be applied to set the ratio in terms of temperature. The Boussinesq approximation relates the density variation to be a function of temperature rise, as shown in Equation (2.2).

$$\rho = \rho_0 + \Delta\rho \rightarrow \Delta\rho = -\beta\rho_0\Delta T \quad (2.2)$$

$$\frac{\text{Re}_m}{\text{Re}_p} = \frac{V_m D_m \nu_p}{V_p D_p \nu_m} = \left[ \frac{\left(\frac{\Delta\rho}{\rho}\right)_m}{\left(\frac{\Delta\rho}{\rho}\right)_p} \right]^{1/2} \left[ \frac{D_m}{D_p} \right]^{3/2} \frac{\nu_p}{\nu_m} \quad (2.3)$$

If the Richardson numbers match then the velocity ratio may be extracted from Equation (2.1). This may be substituted into the Reynolds number ratio to make the ratio a function of density variation or temperature rise shown in Equation (2.3). Using these ratios the



independent variables of the experiment are determined. When modeling a DCC experiment, the independent variables would be the core heat input and distribution. For a PCC experiment a pump would be added, so the flowrate and core heat would act as the independent variables. Since this is just a preliminary testing maximum power was supplied to the active pipes. Since the model will be operating at much lower temperatures and pressures than the prototype, matching  $Re$  and  $Ri$  is not possible with the same working coolant. If the working coolant for the model was replaced with water, the density and viscosity for cold and hot water (approximately 20 and 46 °C) are appropriate to match the Richardson and Reynolds number of the high temperature and pressure helium in the prototype.

Using the scaled geometry in Table 2.1 and Figure 2.1 a design for the experimental facility was generated, shown in Figure 2.3. The grey parts are polycarbonate, and the blue parts are stainless steel chosen for high thermal conductivity. The dimensions without the wall thickness of the geometry were matched with the INL provided ones. The diameter of the main coolant inlet and outlet are 1 in and 3 in, respectively with a length of 1.94 m. The basis for the design was a closed loop system where the flow is driven purely by natural circulation. The coolant enters the lower plenum from the inlet pipe, and is drawn up through heated pipes by natural convection. The water then leaves the pipes as slow jets into the upper plenum, the region of interest. The water exits the upper plenum through the downcomer, the region between the core containment and outer containment. A heat sink would need to be built that removes heat as the flow goes through the downcomer to the outlet pipe of the system. The outlet pipe leads to a

reservoir tank which then leads back to the inlet pipe completing the coolant loop. Next the pipe layout for the core was needed. Through collaboration with INL a final design of 25 pipes with a 1.905 cm inner diameter arranged in an octagonal pattern equidistant from each other was chosen, shown in Figure 2.4. Initially an annular pattern was considered, but was overruled as having the pipes be equidistant was priority. The pipes would be heated with heating tapes which were sorted in groups of five. These five groups would then be connected to five voltage variable transformers which could control the power to the heating tapes, and the resulting heat input. For this study, only T group was run for the tests. Multiple design parameters were considered during the design process, the largest being: waterproof access to the core for wiring, ease of assembly and disassembly, data acquisition, and fabrication limitations.

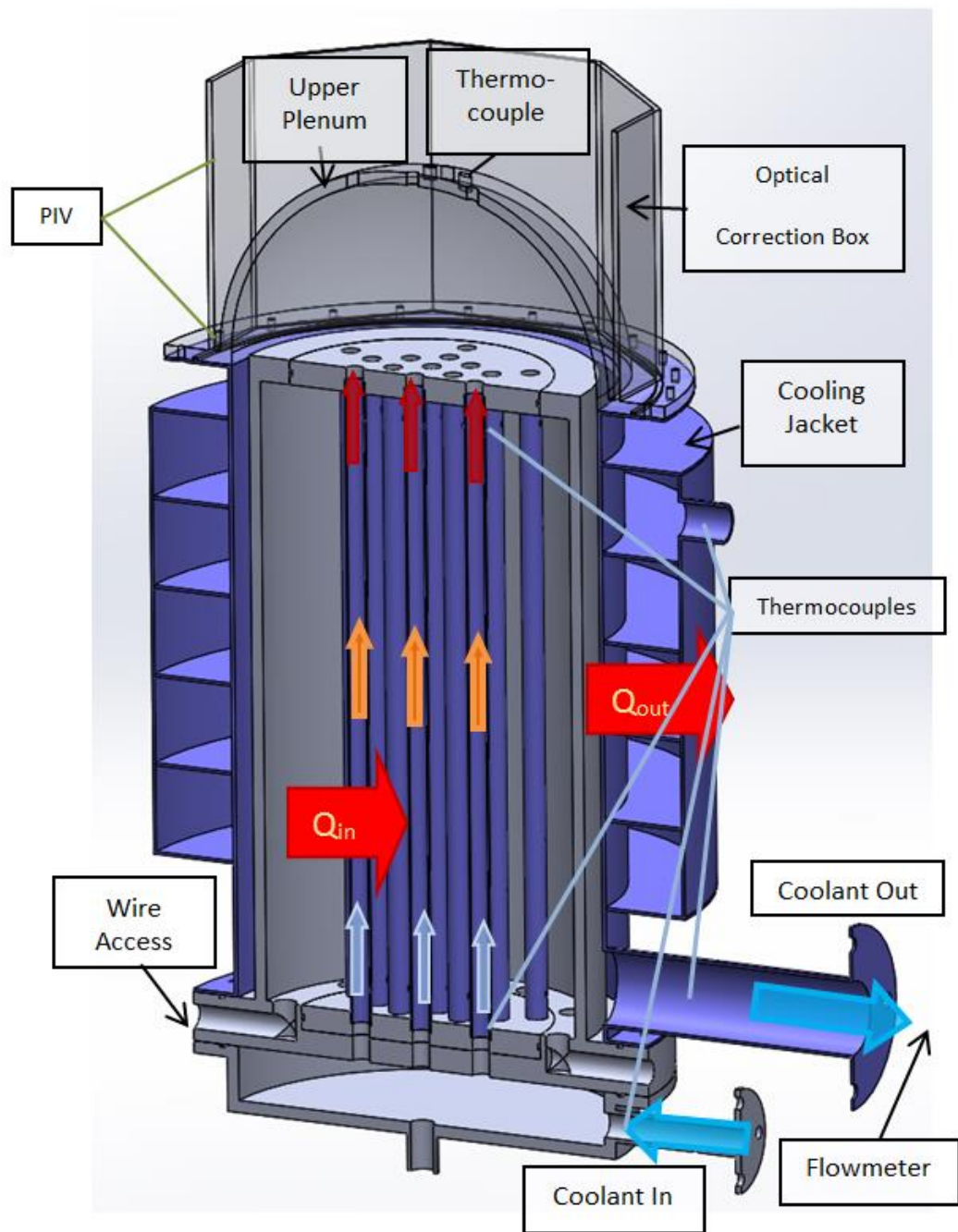


**Figure 2.3.** Experimental facility schematic.

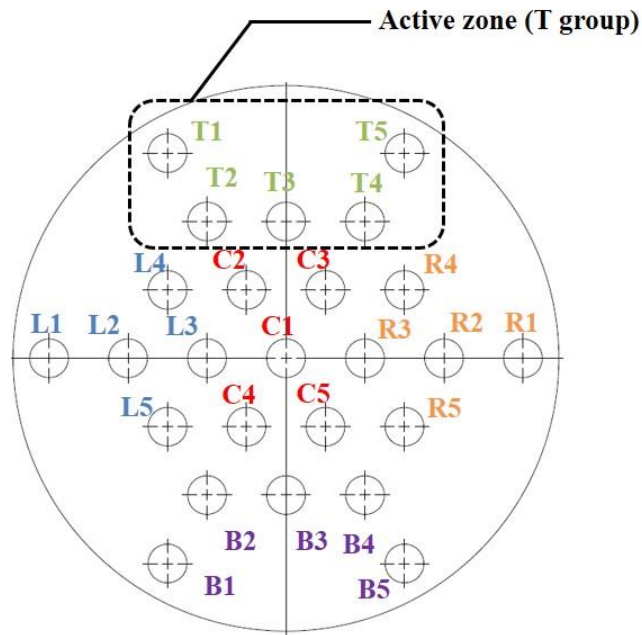


**Figure 2.4.** Core piping.

A heat sink is needed to remove the majority of the heat input to reach steady state and help induce natural circulation. Since the DCC simulation is driven through natural circulation any large pressure drops in the system would inhibit the flow rate and the resultant data may not be representative. Instead an external non-intrusive cooling jacket was needed that would be connected to the outer containment and remove heat. The cooling jacket and reservoir removes sufficient heat from the system so that it may achieve steady state, without impacting the flow in the upper plenum where data is recorded. This effectively acts as the RCCS for the prototype. Because the reservoir is much larger than the test vessel, there would be no significant reservoir temperature rise during a test. To simulate a PCC scenario, an in-line heat exchanger is needed to remove sufficient heat to reach steady state. The final cooling jacket design shown in Figure 2.5 has five rows of

baffles. Water is pumped into the lowest baffle where it circles the containment and then rises 8.89 cm. This process is repeated until it reaches the cooling jacket outlet.

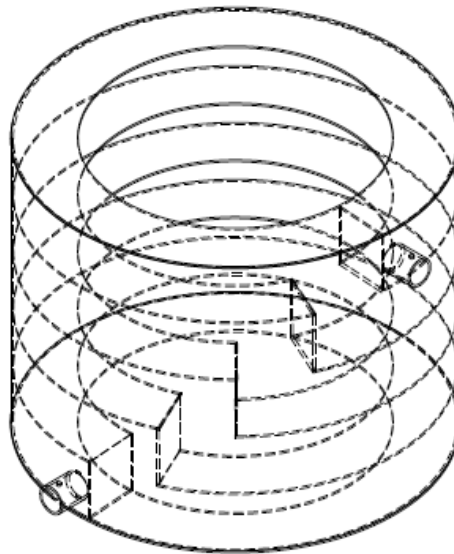


**Figure 2.5.** Cooling jacket design.

## 2.3 Fabrication and Construction

Figure 2.6 shows the assembly procedure. First the core containment and outer containment are lowered onto the lower plenum and their flange is bolted and sealed with O-rings. Next the core is assembled with the 25 pipes sealed into two plates with O-rings. The core is then dropped into the core containment where O-rings seal the plates with the containment. Finally the upper plenum is dropped and bolted onto the outer containment and sealed with either an O-ring or gasket. An arc welder was used to create T-type thermocouples which have an accuracy of  $\pm 0.5$  °C, that were then calibrated using a certified thermometer with an accuracy of  $\pm 0.3$  °C, installed at the centerline of the core piping and test vessel inlet and outlet. The combined accuracy of the measured temperature was calculated by taking the square root of the sum of the squares and was estimated  $\pm 0.58$  °C. As shown in Figure 2.3 the thermocouples will measure the temperature rise for each pipe in the core, the temperature rise of the main coolant loop, and the temperature rise in the cooling jacket. The thermocouples enter the fluid through compression fittings, which are welded to the 25 pipes. To prevent leaks through the thermocouple locations, the thermocouples were inserted into fine steel tubing and both ends were sealed with UV epoxy as shown in Figure 2.7 (top); this also protects the thermocouple tips from corrosion. The temperature was measured at the center of the steel tubing as shown in Figure 2.7 (bottom). There are nine ports for thermocouples in the upper plenum that may be inserted vertically above the pipe outlets to measure the temperature field. The thermocouples are connected to a National Instruments SCXI-1600

data acquisition system and measured with LabVIEW. An ultrasonic flowmeter, Krohne Optisonic 6400, measures the outlet flow rate of the main coolant loop with an accuracy of  $\pm 1\%$  reading value for flow greater than 0.5 m/s, and a paddlewheel flowmeter measures the cooling jacket flow rate with an accuracy of  $\pm 0.227$  L/min.

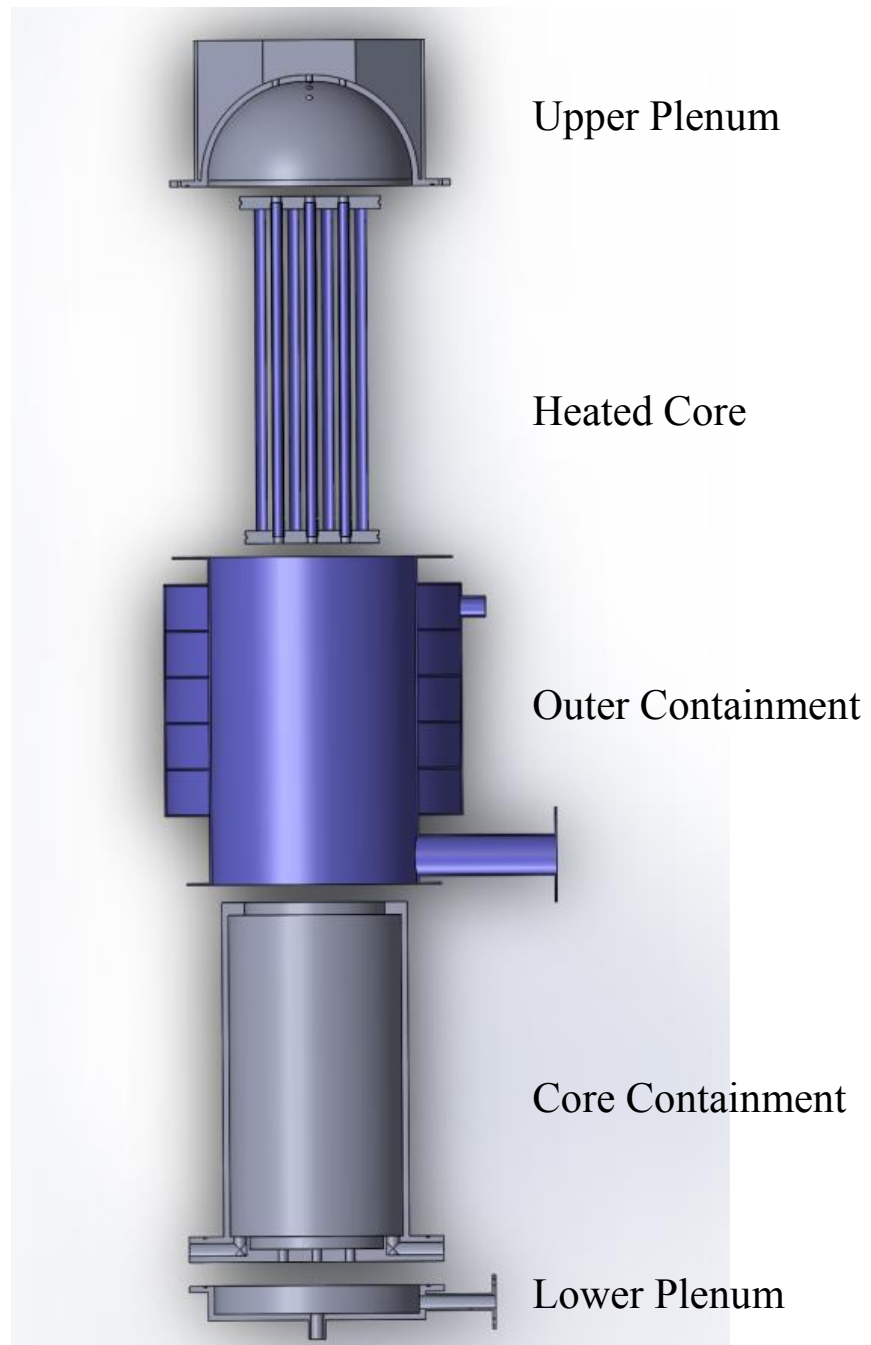


**Figure 2.6.** Exploded assembly cross section.



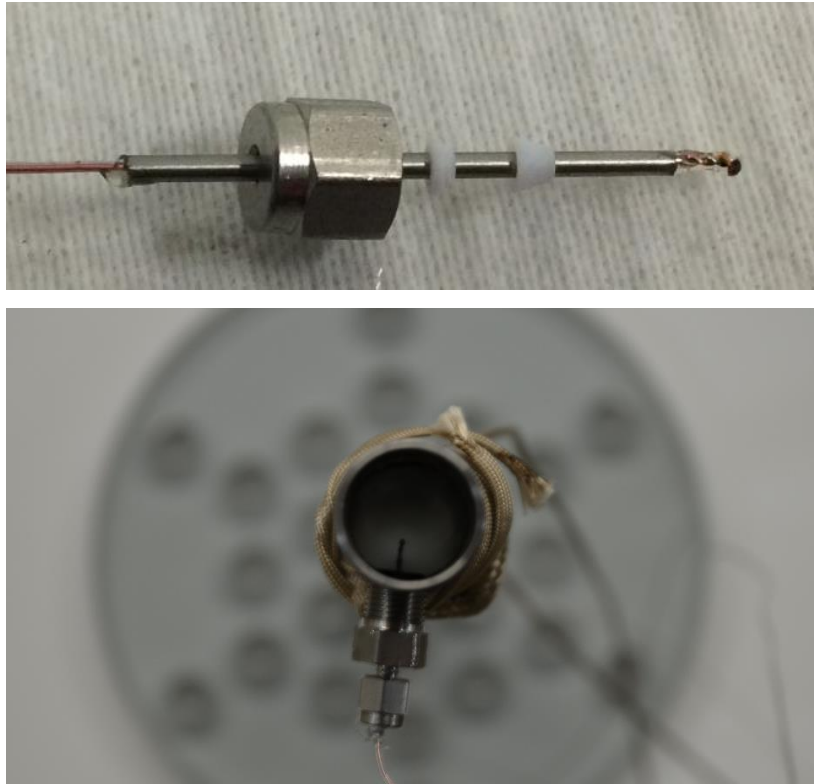
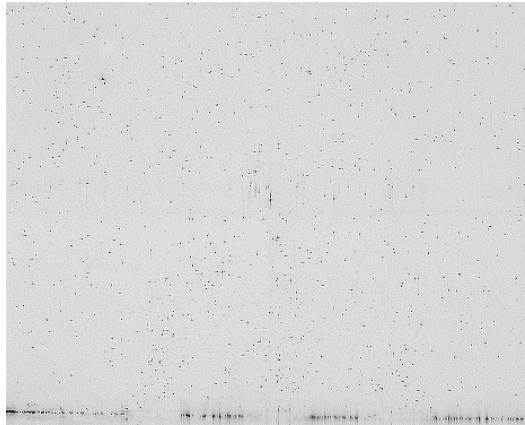


**Figure 2.7.** Thermocouple with tubing, epoxy, and ferrules (top) and its location for the temperature measurement inside the steel tubing (bottom).

PIV is used to measure a planar velocity field in the upper plenum. PIV involves seeding the working fluid with particles of equal density, and firing a laser sheet pulse that illuminates a plane of particles. The illuminated particles are then captured with a high speed camera in sync with the laser pulse; a sample is shown in Figure 2.8. Two laser pulses are fired in quick succession and both particle images are captured. A program then uses cross-correlation to track the patterns of particles between the two images, and using the time between the pulses a velocity vector field can be generated [15]. For this study a Vlite series dual laser pulse system was used, which operated at a wavelength of 532 nm with a pulse width of approximately 1 mm. A high speed camera MEMRECAM GX-3

was used for the imaging, and connected to the laser with a waveform generator. A lens Zeiss 2/50 Makro-Planar ZF.2 Macro Lens was used for the test. For the particle seeding fluorescent orange polyethylene microspheres were used. Their diameter ranged from 53-63  $\mu\text{m}$ , and had a density of  $1.002 \text{ g/cm}^3$ . Fluorescent particles reflect the laser light at a different wavelength, so an optical filter was used for the camera that blocked the wavelength of the laser and consequently removing all light noise and producing clear particle images. As shown in Figure 2.3 a correction box is built around the upper plenum; when a curved surface is filled with water there is an optical distortion caused by refraction. The correction box presents a flat viewing plane, and the medium between the plane and curved surface is filled with water so that the images may be recorded on a flat surface without refraction. An optical test was performed in Figure 2.9 to confirm there were no distortions. The heating tapes were sealed individually with silicon tubing for waterproofing and insulation. Figure 2.10 shows the assembly procedure of the test facility. Figure 2.11 and 2.12 show the completed test facility and its schematic design, respectively.



Test 1



Test 2



Test 3

**Figure 2.8.** Particle images for PIV with black and white inversion.

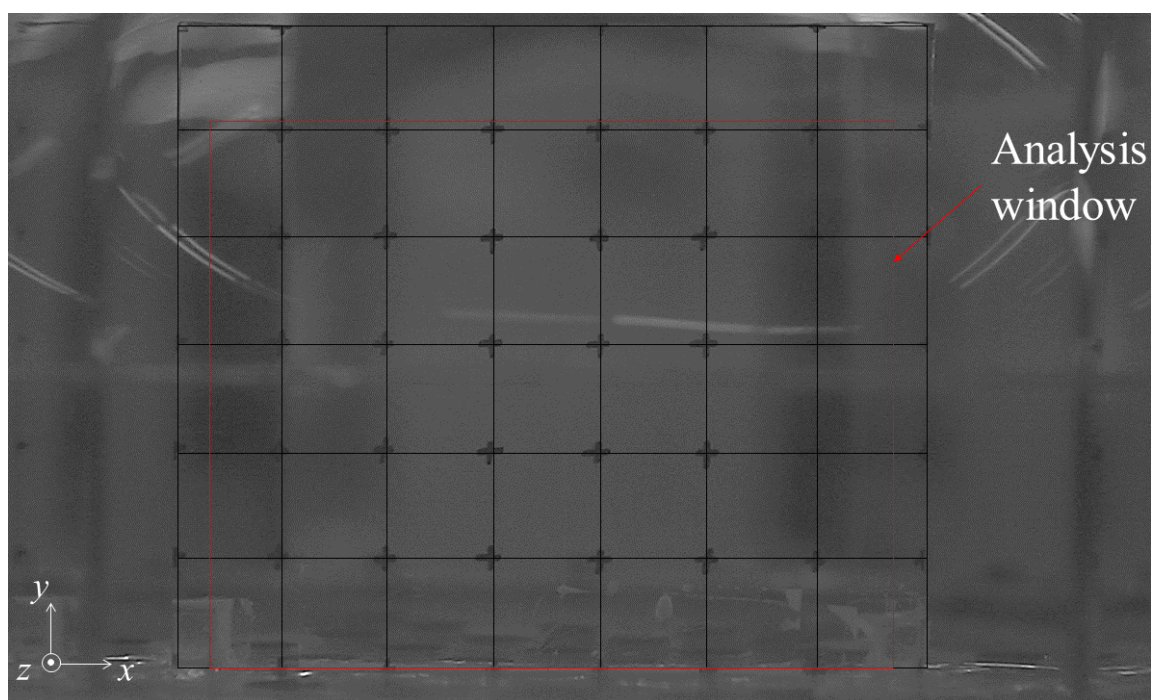


**Figure 2.9.** Optical distortion test.

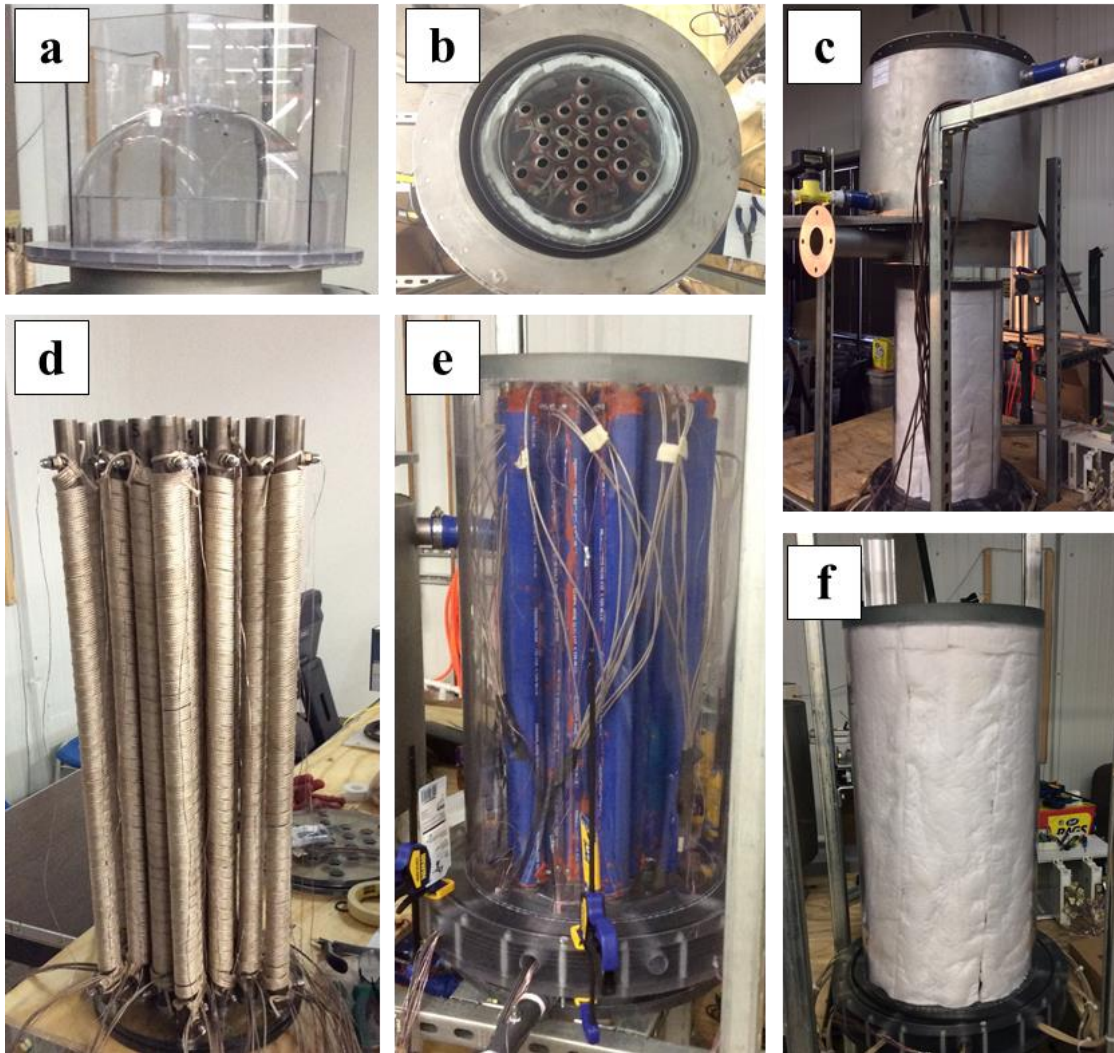


**Figure 2.10.** Assembly procedure of the test facility: (a) upper plenum with the correction box, (b) internal core top view, (c) outer containment being lowered by a forklift, (d) 25 coolant channel pipes with heating tapes and thermocouples, (e) silicon tubings and core assembly, and (f) core insulation.

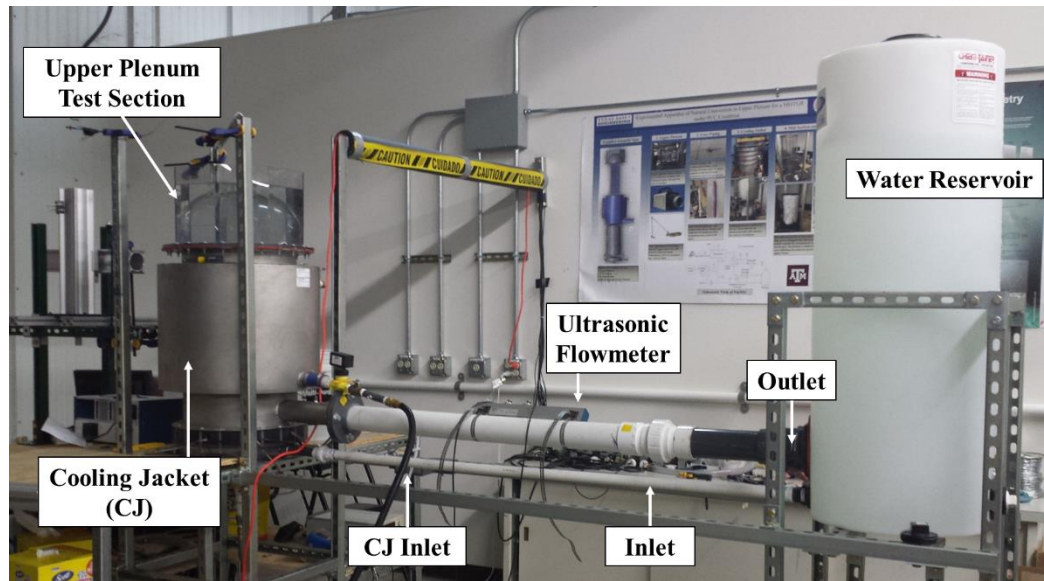


**Figure 2.11.** Completed test facility

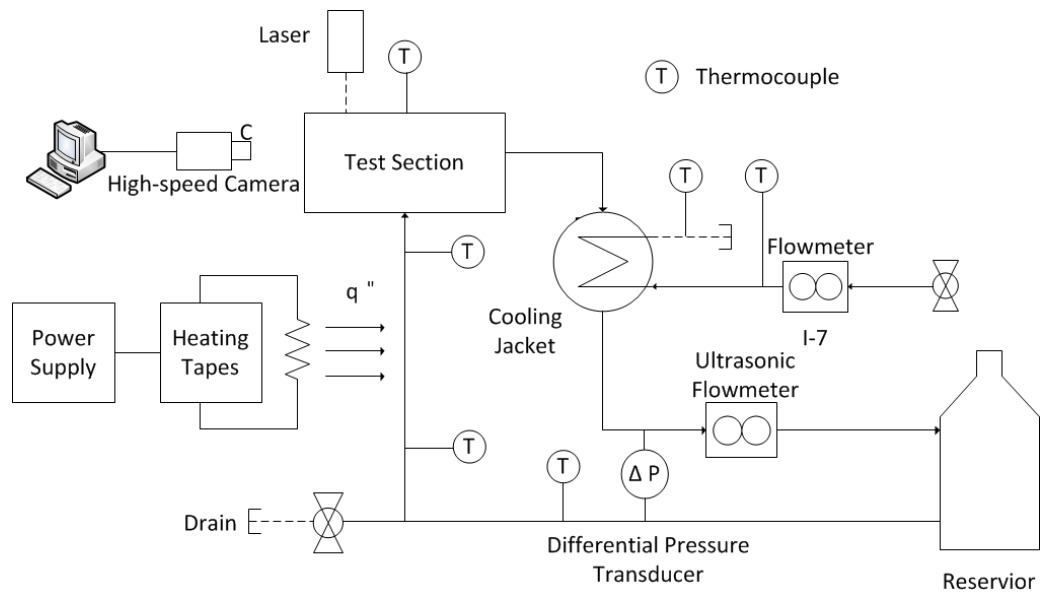


**Figure 2.12.** Schematic view of facility

### **3. PRELIMINARY TEST**

A set of three preliminary tests has been performed in order to obtain the validity of the PIV data analysis. At the time when the test was being conducted the heated pipes were not fully functioned and only five T-group pipes were operated for the tests. The work on this chapter was published on the journal paper [20] and the contents of the manuscript has been modified and rearranged.

#### **3.1 Experiment Method**

The system was run at partial core power to test the validity of the PIV process and capabilities of the test facility. Power was supplied only to the five pipes in T-group from Figure 2.4, and the other pipes were sealed off. A total of 1.44 kW power was evenly distributed between the five heating tapes for this preliminary test to run the maximum capability of the current test facility. The camera was positioned to capture a  $16 \times 13$  cm window above the outlets of three adjacent natural convection jets, shown in Figure 3.1 and 3.2. The laser sheet is aligned with marked locations on the test facility, and adjusted for the optimal power output. The laser used was a Vlite-200 from Beamtech Optronics Co. It has an average beam thickness of 1 mm, and can provide up to 200 mJ per pulse; we used 60 mJ. The test heaters were left on, and the cooling jacket was turned on to approximately 41.5 L/min, the maximum flowrate of the local water supply. The test



vessel and reservoir were filled with room-temperature water, and then the heaters and cooling jacket were activated. Steady state was determined when the outlet temperature rise across the core was 25–45 °C, and the temperature rise of the test vessel remained near 25 °C and constant for five minutes. Next the particles were injected into the test vessel inlet pipe, and allowed to circulate into the upper plenum. At steady state the coolant outlet temperature of the vessel after passing through the cooling jacket was within 0.5 °C of the reservoir temperature ensuring there would be no significant temperature rise in reservoir that would impede the system reaching steady state. Additionally the low flow rates and large piping resulted in a very low pressure drop to and from the reservoir so flow was not impeded. Once steady state was achieved the particles were injected at the inlet of the test facility, and particle images were collected. The test length was limited by the camera memory, which could hold up to 2,300 images. Because the fluid velocity was low, the camera and laser were synchronized to record images at 10 Hz, which means that time interval of successive images ( $\Delta t$ ) was 0.1 s; the test was run for approximately 4 minutes. The temperature of the system was constant within  $\pm 0.5$  °C once the system achieved steady state, and recorded with thermocouples at 1 Hz.



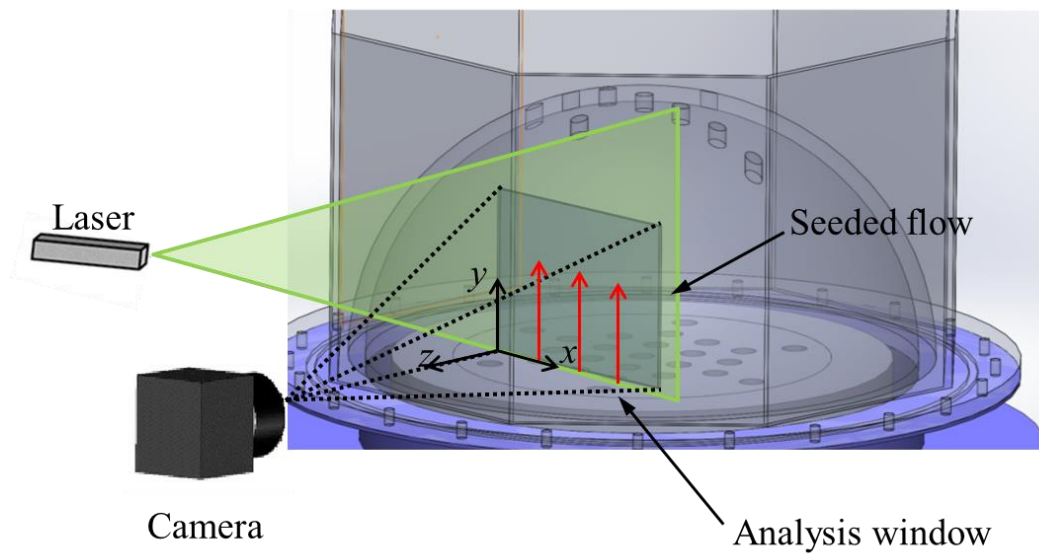


**Figure 3.1.** PIV schematic.

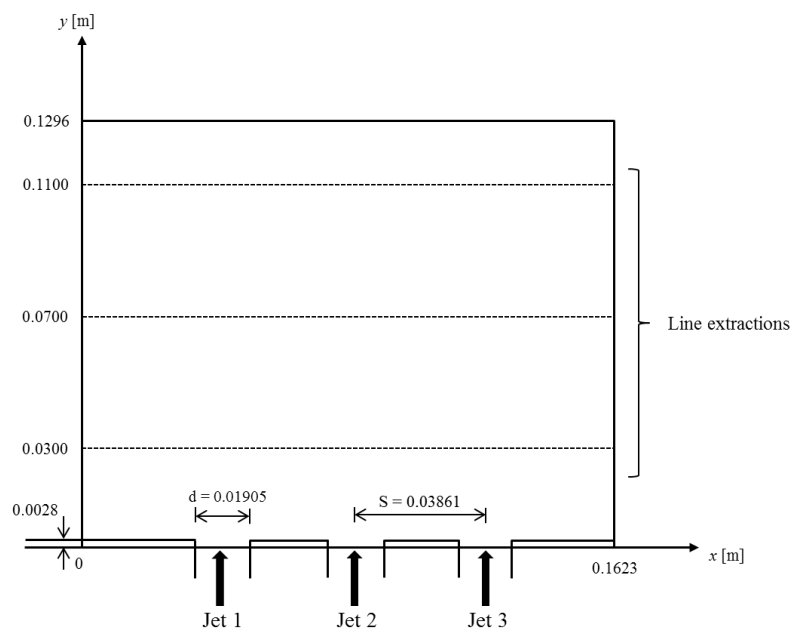


**Figure 3.2.** Analysis window geometry.

While the test was running the Krohne Optisonic 6400 ultrasonic flowmeter was measuring the total flow rate of the main coolant loop. The flowmeter had a 1% reading value accuracy for larger flow rates, but had no in-situ calibrations at the low operating flow rate of the system. A Krohne Optiflux 1000 electromagnetic flowmeter was installed on a nearby system and validated with an accuracy of  $\pm 3\%$  reading value at the operating low flow rate. An electromagnetic flowmeter is more accurate than an ultrasonic flowmeter due to the different measuring principle it employs. Because the flowmeter was in use, and could not operate on the 3" diameter pipe, the electromagnetic flowmeter was used to calibrate the ultrasonic flowmeter. The ultrasonic recorded flow for seven minutes and averaged the values, the average was then compared to the flow rate of the Optiflux reading. This was performed at six different low flow rates. The calibration formed a linear trendline shown in Figure 3.3, and the trendline equation was used to correct all test measurements.

The images were processed using PIVlab (version 1.32). PIVlab is an open source MATLAB-based package developed by Thielicke and Stamhuis [21] and has been verified by several investigators [22-26]. The 2,300 images were imported in a first-second, third-fourth image pair manner so approximately 1,150 image pairs or frames were available.

The analysis window was  $16 \times 13$  cm with a  $1280 \times 1024$  high resolution, and a  $0.125 \times 0.127$  mm/pixel size. Including the time between images, 1 px/frame corresponds to 1.26 mm/s. When the particles are illuminated by the laser they occupy  $4 \times 4$  pixels. When running PIV three interrogation windows were evaluated:  $64 \times 64$ ,  $32 \times 32$ , and  $16 \times 16$ , and a step width of 32, 16, and 8 pixels respectively. The average particle shifted 65

pixels in one image pair. The calculated Stokes number of the seeding particles was calculated to be 0.0014 at the worst, confirming the seeding particles followed the fluid flow accurately [27]. After calculating the velocity vectors for each image pair, PIVlab runs an algorithm with that located erroneous vectors with a user input standard deviation threshold value (7) and replaced them with the mean value of the neighboring vectors, the details may be found in the cited document [21].

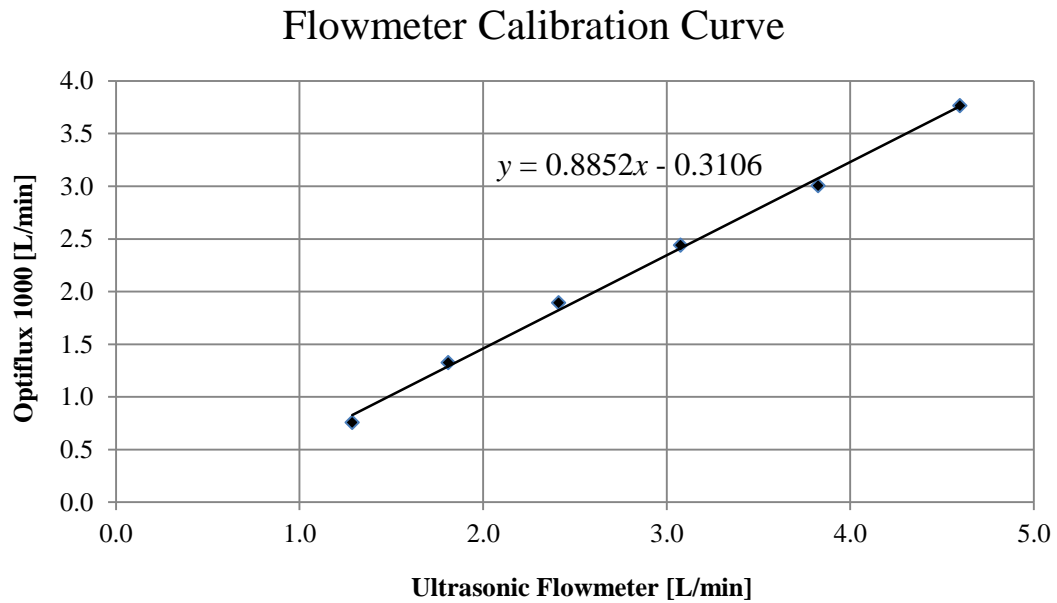


**Figure 3.3.** Flowmeter calibration line.

### 3.2 Sensitivity Analysis

The turbulent velocity field fluctuates transiently, but statistically steady state may be measured by averaging the velocity for a batch of frames. This is shown in Equation (3.1),

$$\mathbf{v}(r,t) = \overline{\mathbf{v}(r)} + \mathbf{v}'(r,t) \quad (3.1)$$

where the instantaneous velocity  $\mathbf{v}$  is represented as the averaged velocity  $\overline{\mathbf{v}}$  and the velocity fluctuation  $\mathbf{v}'$ . In order to validate the results multiple tests need to be run. A total of three tests were run for statistically steady state (Test 1, Test 2, and Test 3). One thousand frames were averaged to achieve the representative averaged velocity field over a duration of 200 seconds. The averaged velocity magnitude contour and streamlines are shown in Figure 3.4 and 3.5. There is a distortion 7 centimeters from the pipe outlets, this is due to the glued section between the curved dome and the cylinder in the upper plenum which slightly blurs the image and makes the particles harder to track. At 1 cm from the pipe outlet the contour is representative of the experimental flow. There is slight recirculation between the jets very close to the pipe outlet. The jets begin to merge approximately 3 cm from the pipe outlet, but diverge as the flow approaches the top of the test geometry which is exhibited by the streamlines. The x and y-velocity contours are shown in Figure 3.6 and 3.7 respectfully. Figure 3.6 shows that far from the pipe outlet the flow begins moving horizontally towards the downcomer. Figure 3.7 shows that the flow is predominantly vertical as the y-velocity contour nearly matches the velocity

magnitude contour. Figure 3.8 shows the averaged vorticity contour, calculated from Equation (3.2).

$$\omega = \frac{\partial v}{\partial x} - \frac{\partial u}{\partial y} \quad (3.2)$$

A single frame produces an instantaneous flow with eddies, but once averaged the results show good anti-symmetry. Directly between the jets the vorticity fluctuates such that the averaged value is approximately zero.

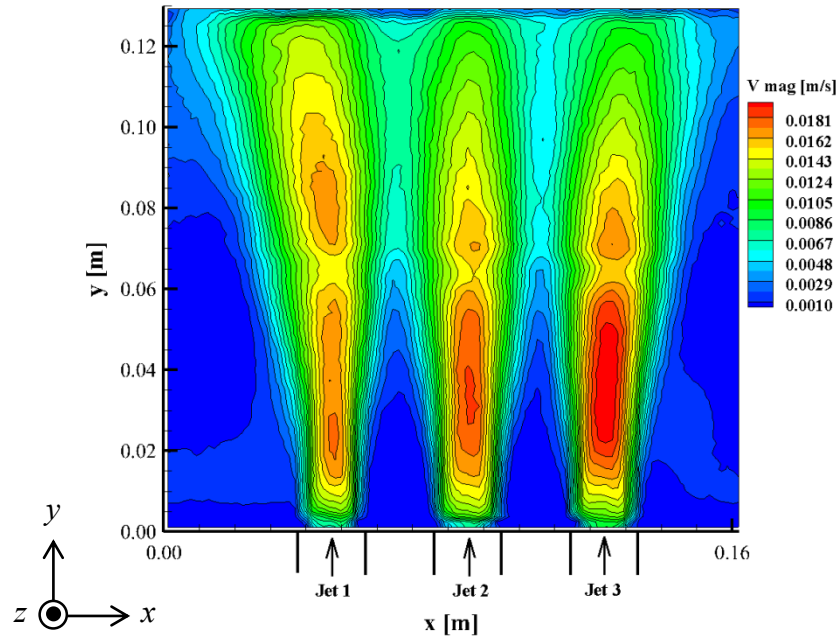


**Figure 3.4.** Velocity magnitude contour of 1,000 frames.

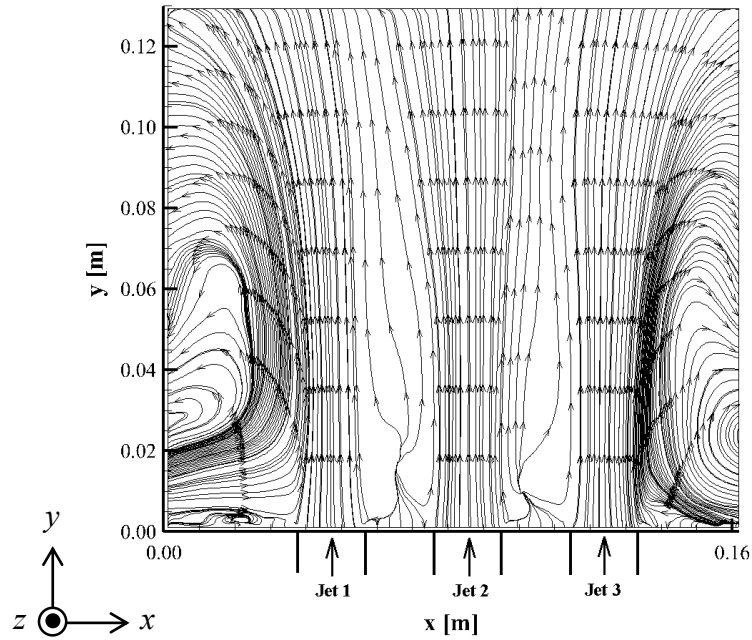


**Figure 3.5.** Streamline of 1,000 frames.

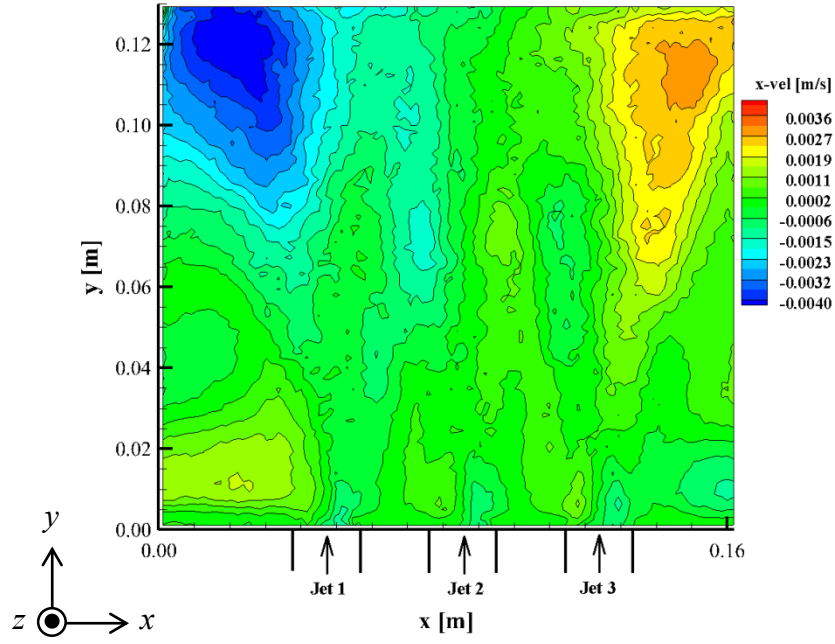


**Figure 3.6.** x-velocity contour of 1,000 frames.

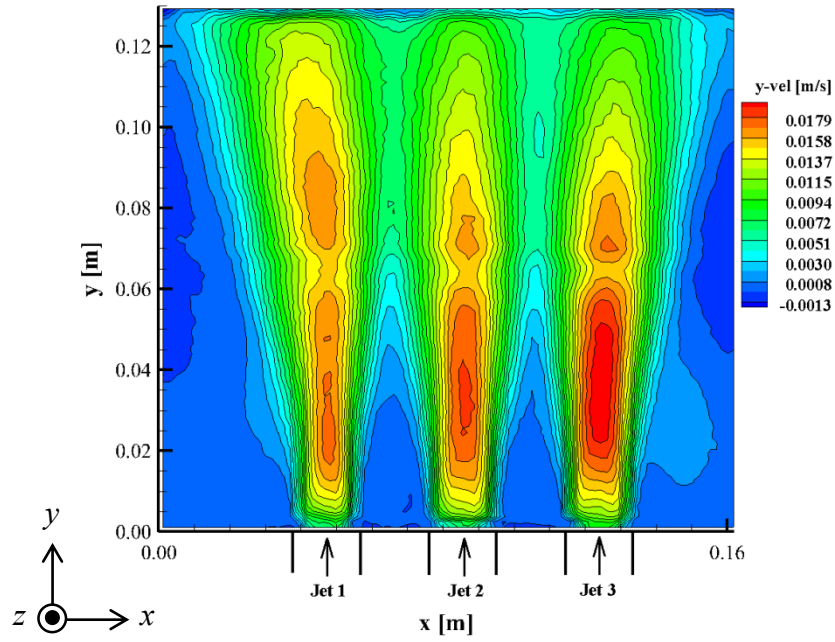


**Figure 3.7.** y-velocity contour of 1,000 frames.

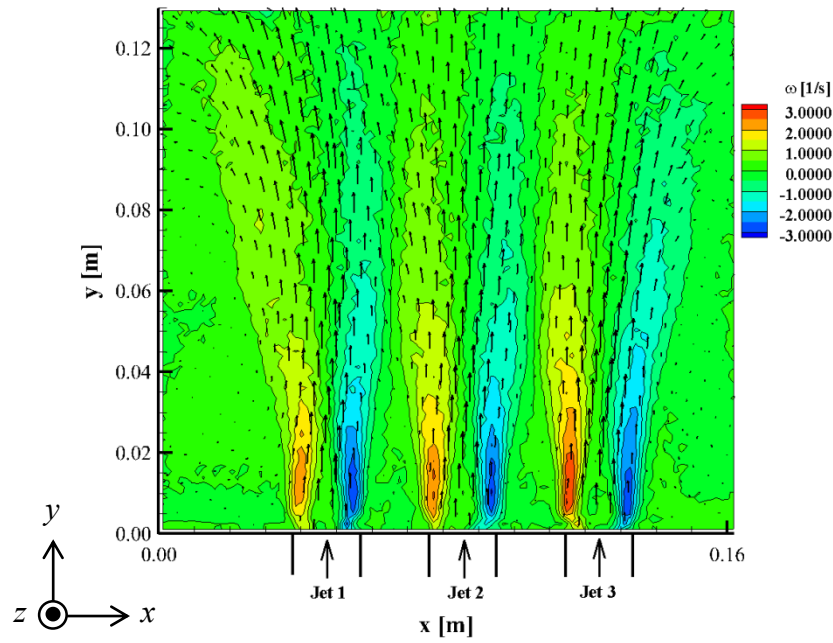


**Figure 3.8.** Vorticity contour and average velocity vector of 1,000 frames.

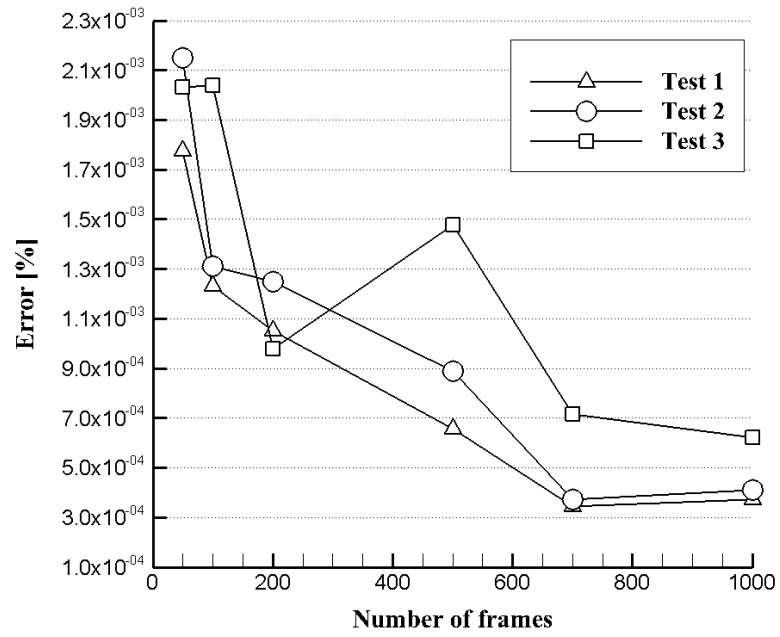


**Figure 3.9.** Percent error of y-velocity for different batch sizes of frames.



First a sensitivity analysis must be performed to confirm a sufficient number of frames were used to correctly model statistically steady state; a similar analysis was performed by Amini and Hassan [28]. To do this, different batch sizes of frames were used to calculate the averaged velocity field and this was compared to the previous averaged velocity field; as the batch sizes increase the flow profiles should began to match. The root-mean-square (RMS) deviation was calculated using Equation (3.3),

$$Error = \sqrt{\frac{\sum_{i,j=1}^n (v_{i,j}^k - v_{i,j}^{k-1})^2}{N}} \quad (3.3)$$

where  $v_{i,j}^k$  represents the averaged y-velocity field  $(i, j)$  at current frame count  $(k)$ ,  $v_{i,j}^{k-1}$  represents the averaged y-velocity field  $(i, j)$  at previous frame count  $(k-1)$ , and  $N$  is the current number of frames  $(k)$ . This was run for all  $159 \times 127$  vectors from PIVlab using the Fast Fourier Transform (FFT) option, the results are shown in Figure 3.9. As the batch sizes increase errors continue to decrease constantly and reach less than  $5.0 \times 10^{-4}$  after the 700 frames average, confirming that 1,000 frames are sufficient to measure statistically steady state. Tests 1 and 2 converge as expected, but Test 3 converges abnormally implying that the results may be misrepresentative of the flow and will not be shown in this study. It is hypothesized that this occurred because insufficient time was allowed to let the particles circulate through the system for Test 3. Figure 2.8 shows the particle density difference between the tests.

Additionally the y-velocity was extracted at 3, 7 and 11 cm from the pipe outlet for different batch sizes. Note that each symbols represents following numbers of frames: 50 frames ( $\circ$ ), 200 frames ( $\blacktriangledown$ ), 500 frames ( $\bullet$ ) and 700 frames ( $\nabla$ ). The solid line is the velocity for 1000 frames and is used as reference. At 3 cm Figure 3.10 and 3.11 show the majority of the batch sizes match the reference. At 7 cm Figure 3.12 and 3.13 show that the 50 and 200 batch sizes begin to differ significantly from the reference. Additionally the jets began merging. At 11 cm Figure 3.14 and 3.15, 500 and 700 frames begin to differ slightly, primarily in Test 1. This suggests when modeling significantly far from the pipe outlet to correctly represent the flow field more images need to be processed. Also the jets continue to merge, but stays within the merging region. The analysis window for this study is too small for the jets to fully merge and reach the combined point.

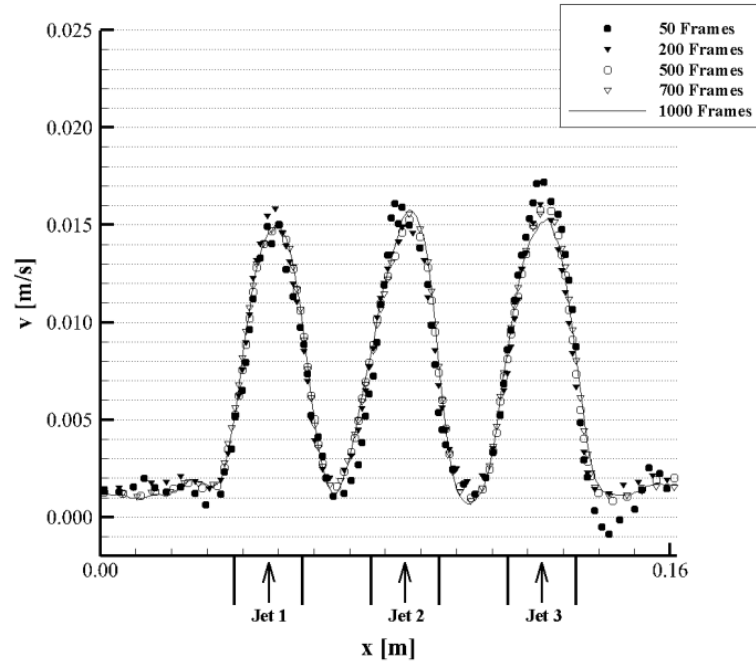


**Figure 3.10.** Test 1 sensitivity analysis at 3 cm from pipe outlet.

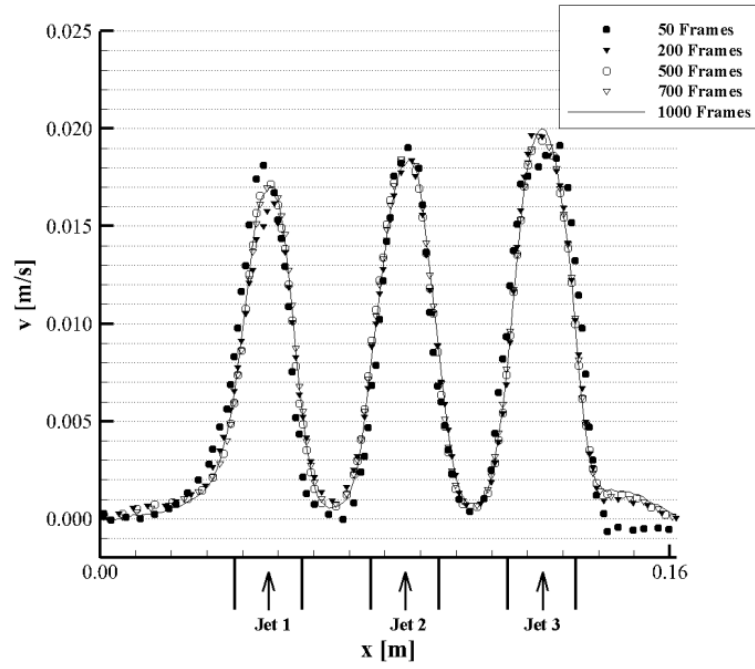


**Figure 3.11.** Test 2 sensitivity analysis at 3 cm from pipe outlet.

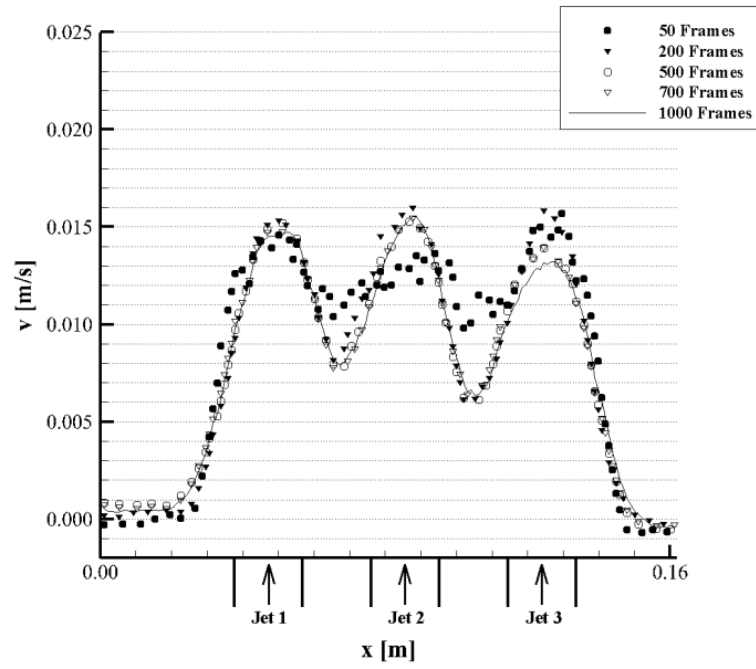


**Figure 3.12.** Test 1 sensitivity analysis at 7 cm from pipe outlet.

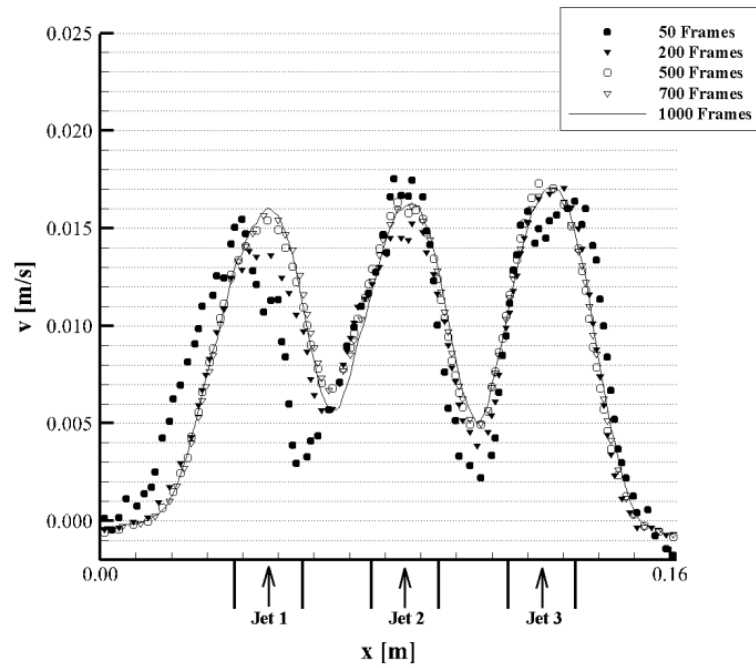


**Figure 3.13.** Test 2 sensitivity analysis at 7 cm from pipe outlet.

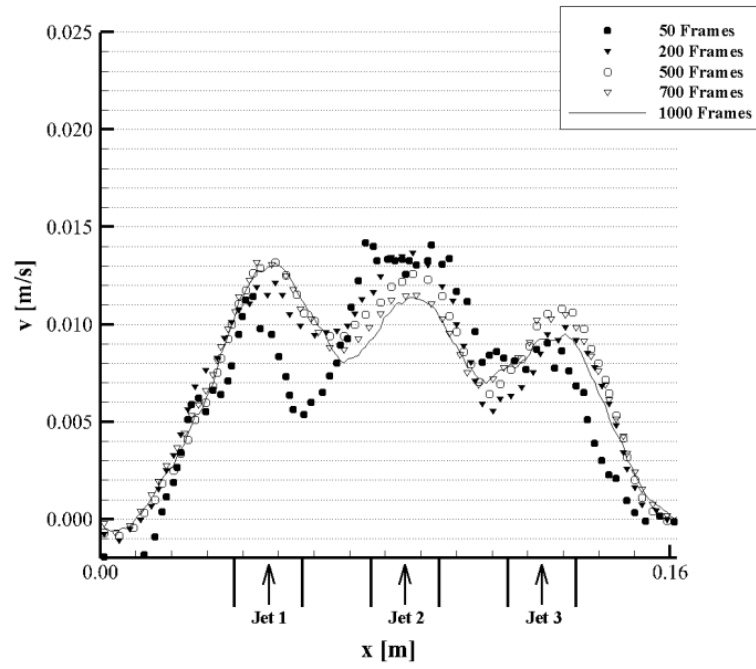


**Figure 3.14.** Test 1 sensitivity analysis at 11 cm from pipe outlet.

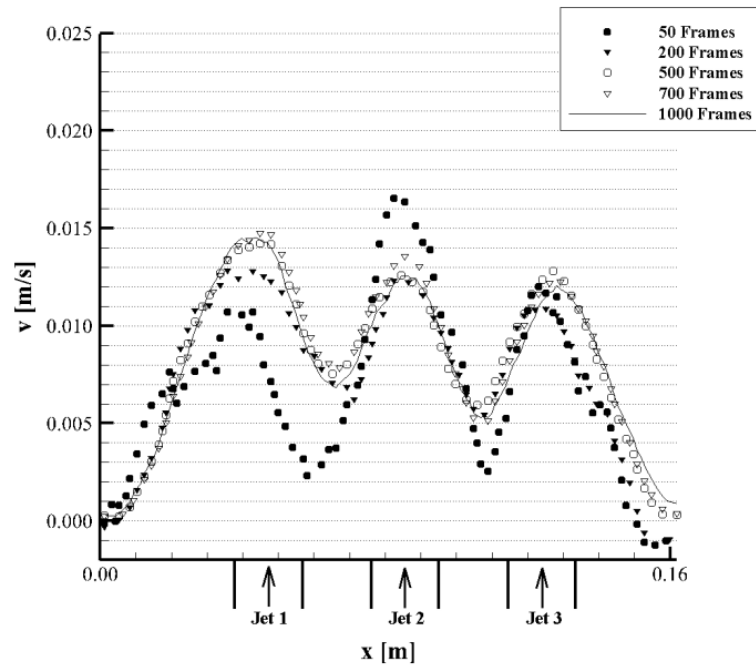


**Figure 3.15.** Test 2 sensitivity analysis at 11 cm from pipe outlet.

### 3.3 Experiment Result

Equation (3.4) was used to average the velocity profile for the 1,000 frames ( $N$ ) for each test, and average the velocity profile between the tests ( $M = 2$ ). The uncertainty was generated by standard deviation between the tests. Figure 3.16 shows that there is uncertainty between the tests; to more accurately assess the repeatability, more tests need to be run.

$$v_{ave} = \frac{1}{M} \sum_{m=1}^M \left( \frac{1}{N} \sum_{k=1}^N v_m^k \right) \quad (3.4)$$

Once the jets enter the upper plenum mixing occurs which causes the flow to become turbulent. The turbulence strength can be calculated by taking the root mean square (rms) of the velocity over a period of time, shown in Equation (3.5).

$$v_{rms} = \frac{1}{M} \sum_{m=1}^M \sqrt{\frac{\sum_{k=1}^N (v_m^k - \bar{v}_m^N)^2}{N}} \quad (3.5)$$

The turbulent intensity (TI) can be calculated by dividing the averaged velocity ( $v_{ave}$ ) from the turbulence strength ( $v_{rms}$ ). Figure 3.17 shows the turbulence strength averaged between Test 1 and 2. The turbulence strength is largest inside the jets where the mixing occurs, and the resulting TI is approximately 41% of the peak velocity, meaning  $TI = 0.4$  in the jets. This shows that the flow goes turbulent in the upper plenum where the mixing occurs, but less so between the jets. TI increases to 45% at the jet velocity peak 11 cm from the pipe outlet.

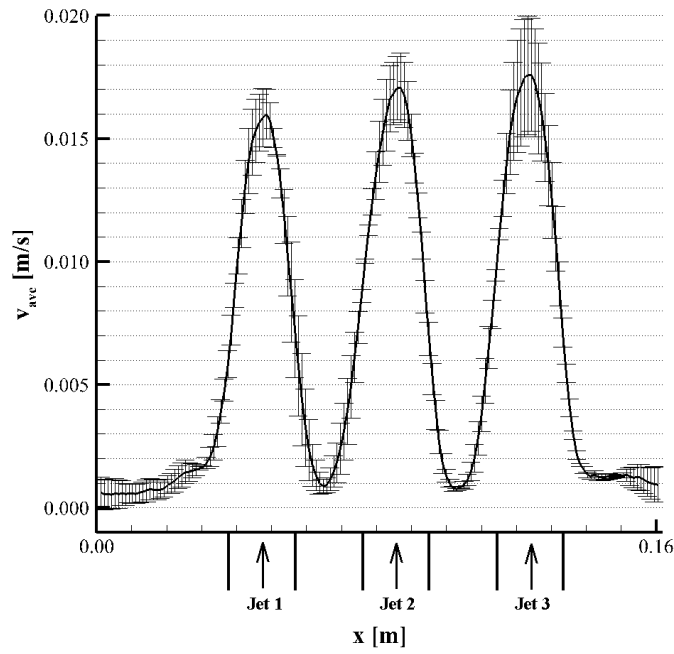


**Figure 3.16.** Average y-velocity at 3 cm from the pipe outlet with standard deviation between the tests.

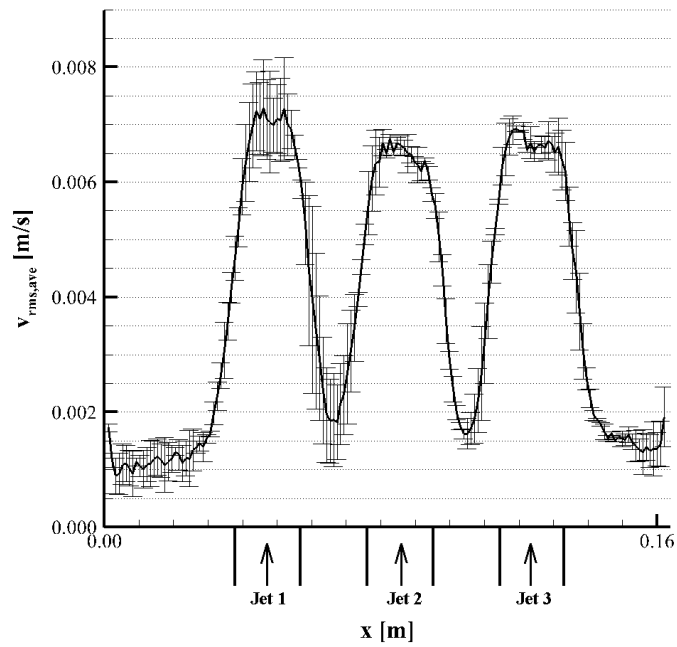


**Figure 3.17.** Averaged turbulence strength at 3 cm from the pipe outlet with standard deviation between the tests.

Next to validate the PIV results, the averaged flow rate for a single pipe is measured using the statistically steady state velocity vector field, and compared to an analytic flow rate and the ultrasonic flowmeter data. The flow rate of a single pipe may be calculated analytically using the heat balance equation as shown in Equation (3.6),

$$\dot{m} = \frac{Q}{c_p \Delta T} \quad (3.6)$$

where  $Q$  is the heat input (W) from the heating tape,  $\dot{m}$  is the mass flow rate (kg/s),  $c_p$  is the specific heat capacity for water (J/kg·K), and  $\Delta T$  is the temperature rise in the core piping (K).  $Q$  is controlled with the variable voltage transformer and the pre-measured resistance of the heating tape, and the temperature rise in the core is measured with thermocouples. At the steady state temperatures (approximately 25°C and 45°C) the specific heat matches, and there is minimal heat loss due to the insulating tubing. While the tests are running the ultrasonic flowmeter records the total flow rate of the system. The flow rates for all three methods are plotted in Figure 3.18. The analytic flow rate uncertainty is due to the error of the T-type thermocouples. From Equation (3.6), the error propagates to Equation (3.7). It was determined that the uncertainty from using centerline temperature rise over mean temperature rise is negligible compared to the RMS deviation of the thermocouples.

$$\begin{aligned} \xi_{\dot{m}} &= \sqrt{\left(\frac{d\dot{m}}{dT_i}\right)^2 \sigma_{T_i}^2 + \left(\frac{d\dot{m}}{dT_o}\right)^2 \sigma_{T_o}^2} \\ &= \sqrt{\left(\frac{Q}{c_p} \frac{1}{(T_o - T_i)^2}\right)^2 0.58^2 + \left(\frac{Q}{c_p} \frac{1}{(T_o - T_i)^2}\right)^2 0.58^2} \end{aligned} \quad (3.7)$$



The ultrasonic flowmeter uncertainty was set to 3%, the error of the Optiflux electromagnetic flowmeter it was calibrated with. The three jets evaluated in the preliminary test have identical geometry and heating, meaning the flow rate for each jet should be equal. When the test facility is under full operation, the jet flow rates vary depending on the location of the pipe due to mixing and other phenomena, however under partial operation there is insufficient mixing to inhibit flow. To evaluate the accuracy of the jets having matching flow rates, the velocity vectors at a jet outlet generated by PIV analysis were averaged and then multiplied with area and density to calculate flow rate; this was performed for all three jets. The uncertainty for the flow rates calculated from the PIV data is the standard deviation of these three jet flow rates. This assumes axisymmetric behavior for the jet; the accuracy of this assumption is a limitation for the present study. The uncertainty of the PIV system will be calculated with a different method. All uncertainties are shown in Table 3.1. The flow rates for all three methods (Analytic flow rate using Equation (3.6), Ultrasonic flowmeter, and PIV) match closely for Tests 1 and 2. The uncertainties for Test 3 do not overlap, which was shown to be irregular from the sensitivity test and thus cannot be validated to be representative of the flow.

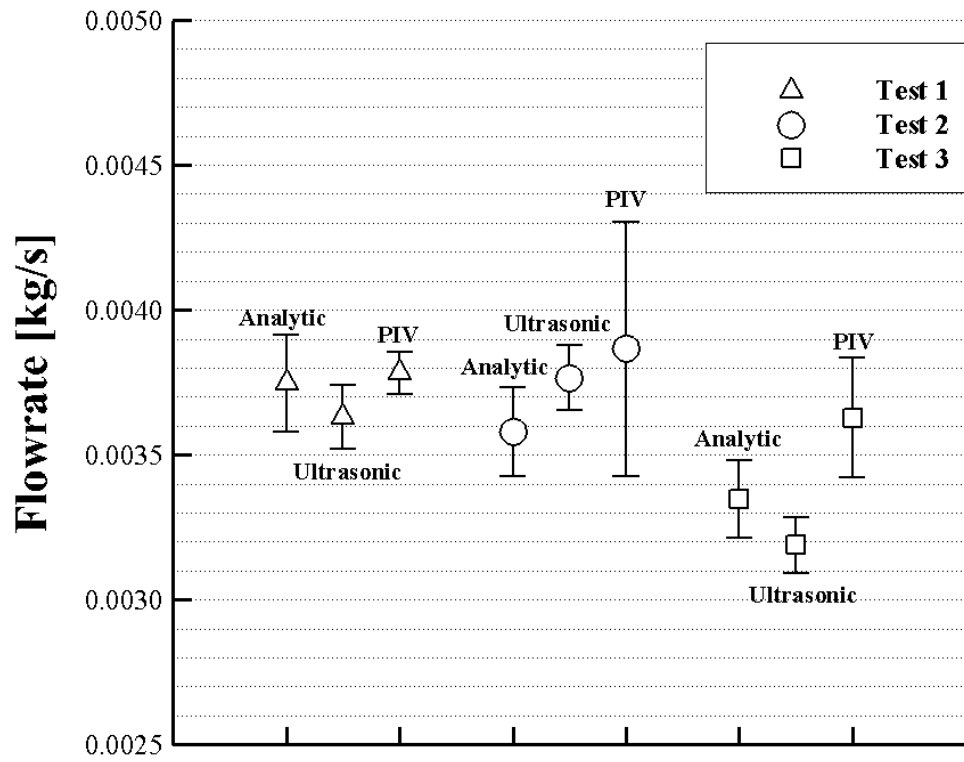


**Figure 3.18.** Flow rate for a single pipe with different methods.

**Table 3.1.** Flow rate uncertainties.

	Analytic	Ultrasonic	PIV
Test 1	1.679E-04	1.089E-04	7.166E-05
Test 2	1.534E-04	1.130E-04	4.383E-04
Test 3	1.340E-04	9.565E-05	2.060E-04

The Visualization Society of Japan (VSJ) proposed a guideline for performing an uncertainty analysis for a PIV system. The present uncertainty analysis was developed based on the VSJ recommendation [24]. Similar approach was performed in the works of Domiguez-Ontiveros and Hassan [25]. Four sources of uncertainty parameters were considered; the magnification factor ( $\alpha$ ), the displacement of particle image ( $\Delta X$ ), the time interval of successive images ( $\Delta t$ ), and the experiment uncertainty factor ( $\delta u$ ). The summary of PIV uncertainties are shown in Table 3.2, and the combined uncertainty was calculated using the Root-sum-square of the product of standard uncertainty and sensitivity coefficient. The largest uncertainty source in the present study is the mismatching error between pair particle images and this can be significantly reduced by the improvement of PIV data processing.

**Table 3.2.** Summary of PIV system uncertainties from VSJ method.

Category	Error sources	Standard uncertainty	Sensitivity coefficient	Combined uncertainty
Calibration $\alpha$ (mm/px)	Reference image	7.00E-01 px	1.87E-04 mm/px <sup>2</sup>	6.92E-04 mm/px
	Physical distance	2.00E-02 mm	1.44E-03 1/px	
	Image distortion by lens	3.48E+00 px	1.87E-04 mm/px <sup>2</sup>	
	Image distortion by CCD	5.60E-03 px	1.44E-03 mm/px <sup>2</sup>	
	Reference position	5.00E-01 mm	2.28E-04 1/px	
	Parallel board	3.50E-02 rad	4.55E-03 mm/px	
Acquisition $\Delta X$ (px)	Laser power fluctuation	7.10E-03 mm	7.69E+00 px/mm	2.10E-01 px
	Image distortion by CCD	5.60E-03 px	1.00E+00	
	Normal view angle	3.50E-02 rad	4.55E-03 mm/px	
Reduction $\Delta X$ (px)	Mis-matching error	2.00E-01 px	1.00E+00	
	Sub-pixel analysis	3.00E-02 px	1.00E+00	
Acquisition $\Delta t$ (s)	Delay generator	1.00E-08 s	1.00E+00	1.41E-08 s
	Pulse time	1.00E-08 s	1.00E+00	
Experiment $\delta u$ (mm/s)	Particle trajectory	5.00E-02 mm/s	1.00E+00	5.44E-02 mm/s
	3-D effects	2.15E-02 mm/s	1.00E+00	

### 3.4 CFD Validation

For CFD validation, Star-CCM+ 9.02 version was used to compare the PIV experiment results. Two different Reynolds-averaged Navier-Stokes (RANS) equation turbulent models were used as follows: k- $\epsilon$  model and Reynolds stress model. Segregated and coupled solvers were tested for the purpose of convergence efficiency. Tetrahedral and polyhedral meshes were used for mesh generation. Physics properties applied to the model were steady state condition, three dimensional, gravity, two-layer all  $y^+$  wall treatment, and constant density. Initial and boundary conditions such as temperature and velocity properties were imposed based on PIV experiment results. Water properties were referenced by NIST Chemistry WebBook. Two cases are compared with the PIV results. The first and second case are k- $\epsilon$  model and Reynolds stress model. Two cases are set to identify the necessity of more complex turbulent models for this particular physical problem.

Results from Figure 3.19 show that at 3 cm from the pipe outlet, the most plausible turbulent model is Reynolds Stress model. The result indicates that the k- $\epsilon$  model is not suitable for the significant mean streamline curvature, flows with strong swirl or secondary flows [29]. Therefore the Reynolds Stress model would be successful in calculating this type of flows. However, neither of those result show superior outcomes, unsteady calculations or Large-eddy simulation would be needed to fully validate the experiment result.

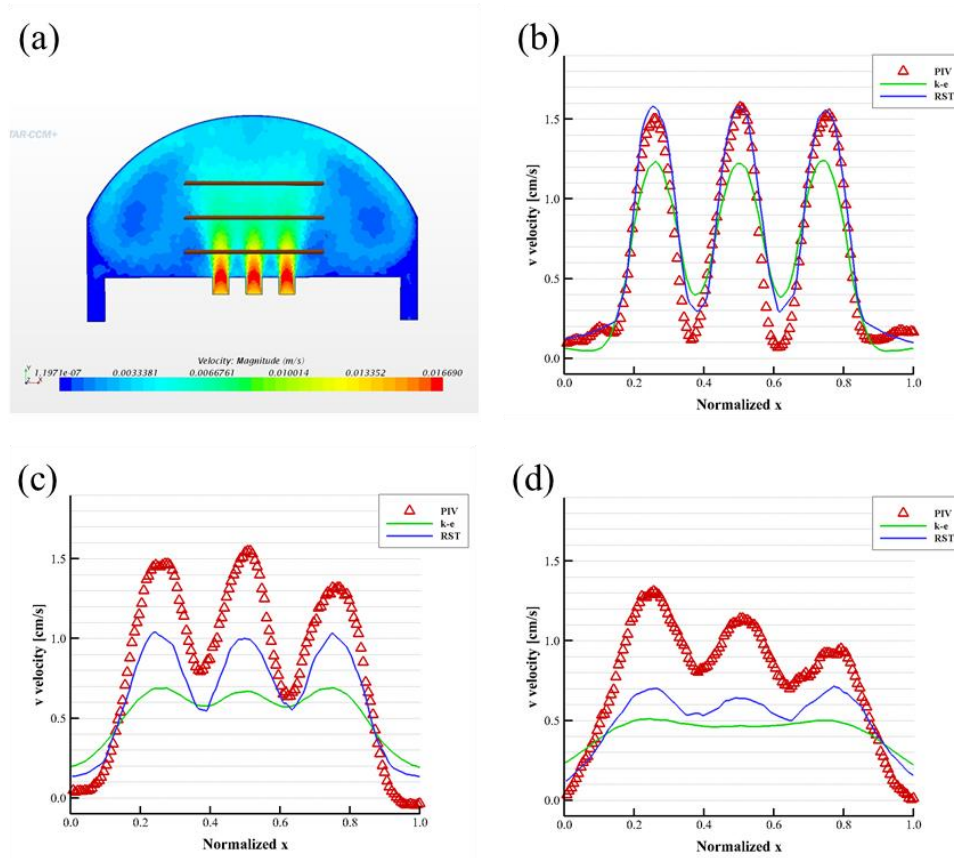


**Figure 3.19.** PIV and CFD comparison at different vertical location (a) each vertical location for the line extraction from the pipe outlet at, (b) 3 cm, (c) 7 cm, and (d) 11 cm for four cases.

### 3.5 Summary

A 1/16<sup>th</sup> scaled VHTR experimental model was constructed and the preliminary test was performed in this study. To produce benchmark data for CFD validation, the facility was first run at partial operation with five pipes being heated. PIV was performed to extract the vector velocity field for three adjacent naturally convective jets at statistically steady state. A small recirculation zone was found between the pipes, and the jets entered the merging zone at 3 cm from the pipe outlet but diverged as the flow approached the top of the test geometry. Turbulence analysis shows the turbulence intensity peaked at 41–45% as the jets mixed. A sensitivity analysis confirmed that 1,000 frames were sufficient to measure statistically steady state. The results were then validated by extracting the flow rate from the PIV jet velocity profile, and comparing it with an analytic flow rate and ultrasonic flowmeter; all flow rates lie within the uncertainty of the other two methods for Tests 1 and 2. This test facility can be used for further analysis of naturally convective mixing, and eventually produce benchmark data for CFD validation for the VHTR during a PCC or DCC accident scenario.

In the next chapter, additional experimental and computational works will be performed. First, experiments from a single plume to multiple plumes will be performed to better understand the turbulent mixing and thermal stresses in the upper plenum. Temperature measurement technique is also accompanied by a simultaneous measurement of the instantaneous velocity profile. Concurrently, different turbulent models with multiple initial conditions will be considered to obtain better results of turbulent

calculations. For example, turbulent viscosity is not obtained from the PIV experiment so a better prediction of these properties should lead to a significant improvement in the CFD results. Comparing the PIV, PLIF, and CFD results will provide a substantial understanding of the natural circulation during PCC and DCC events and will be used for benchmark data for assessment and improvement of codes proposed for NGNP design and safety studies [30].



#### **4. EXPERIMENT MODIFICATION**

After the preliminary tests, the experiment facility was shut down and disassembled to fix the water leak and enhance the performance of the PIV experiment. There were several problems encountered during the preliminary tests as follows:

1. Internal water leakage caused the malfunction of other groups of heating tapes.
2. The individual control towers were needed to manipulate the each heated pipes.
3. Light coming from the outside of the test section induced complications and need to be removed completely.
4. The fluorescent orange particles for PIV experiments are expensive and the amount of particles increased as we subsequently incorporated more numbers of heated pipes.

The first issue was solved by installing the waterproof shrink tubing between the connection of the heating tapes and extension wires. Figure 4.1 shows the previous wire burned out and the current connection wires. The orange-colored shrink tubing has a high temperature sustainability. For the second issue, two additional variable transformers and seven of six-outlet on/off surge protectors were installed as shown in Figure 4.2. Therefore, the contemporary test facility is capable of controlling each individual heating pipe line for the purpose of plume/jet experiment tests.

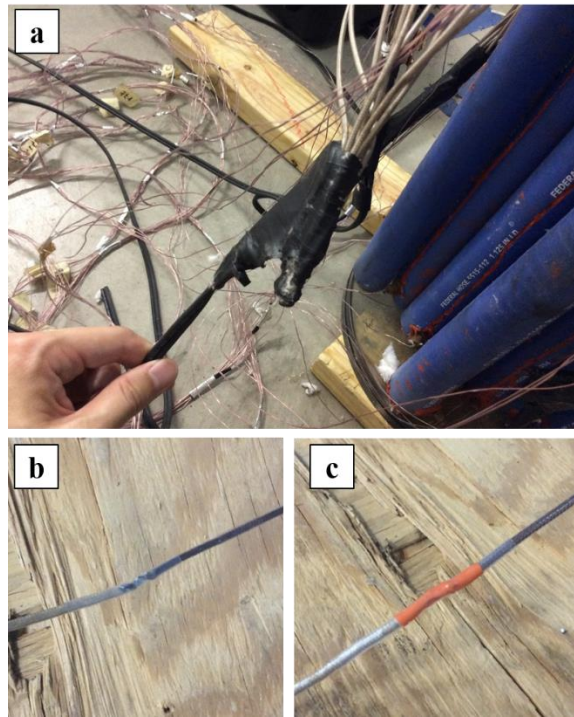


**Figure 4.1.** The procedure of the repair process of the heating tapes and extension wires. (a) Damaged wires were burned due to a short circuit. This caused the heating tapes disconnected. (b) A transparent shrink tubing was installed to protect each individual wires. (c) An orange high temperature shrink tubing was installed to enhance the thermal barrier to the wire connections.

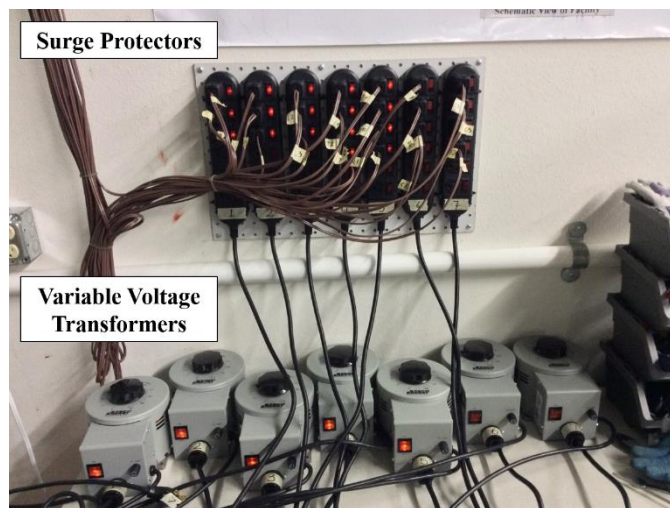


**Figure 4.2.** Surge protectors and variable voltage transformers.

Furthermore, the Unistrut curtain frames were constructed to effectively remove any lighting source coming from the outside as shown in Figure 4.3. The particle recycle system was constructed and installed next to the test facility. This system connects the facility drain pipeline, the sieve, and the water tank. The stainless steel sieve has an opening size of  $44\text{ }\mu\text{m}$  ( $= 325\text{ Mesh}$ ), which is sufficiently small compared to the particle size ( $53 - 63\text{ }\mu\text{m}$ ) used for the PIV experiments. Figure 4.4 shows collected particles on top of the sieve after recycling. It is estimated about 70% of particles can be recycled with this system.

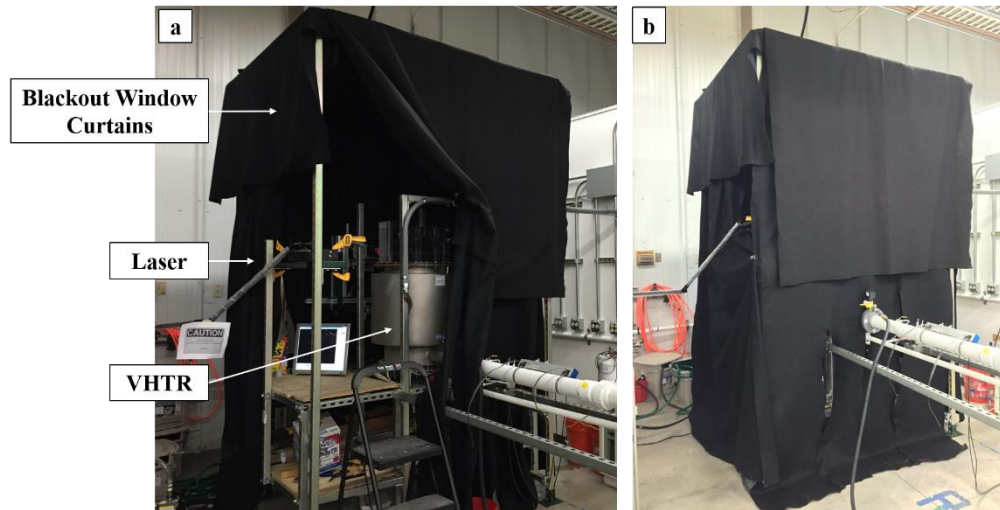


**Figure 4.3.** The blackout window curtains with the double pulse laser, high speed camera, and modeled VHTR inside. (a) When curtains are opened (b) closed.

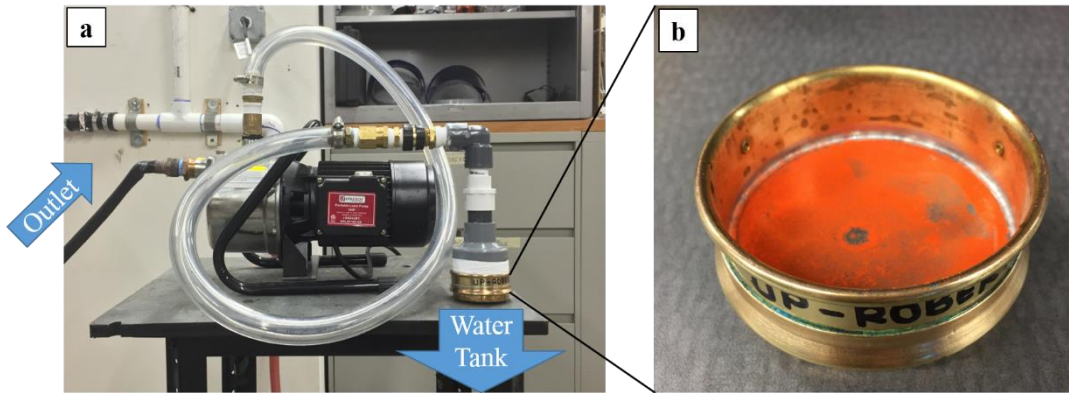


**Figure 4.4.** Fluorescent orange particle recycle system. (a) A pump connected with an exit hose from the test facility and stainless steel frame sieve. (b) A zoom in view of the sieve after collecting particles.

In addition to the issues reported above, the new type of laser system, Nd:YAG laser system made by New Wave Research, including the cooling device, laser power supply, laser head, arm and pulse generator, was utilized and is shown in Figure 4.5. It has dual laser-head system and provides a highly stable green light source for PIV application. The output energy has 15-200 mJ at 532 nm and the frequency varies from 1 to 15 Hz or continuous depending on the test purpose. A quantum Composer 9618+ delay pulse generator was used to control the delay period between the camera shutter speed and laser pulse.

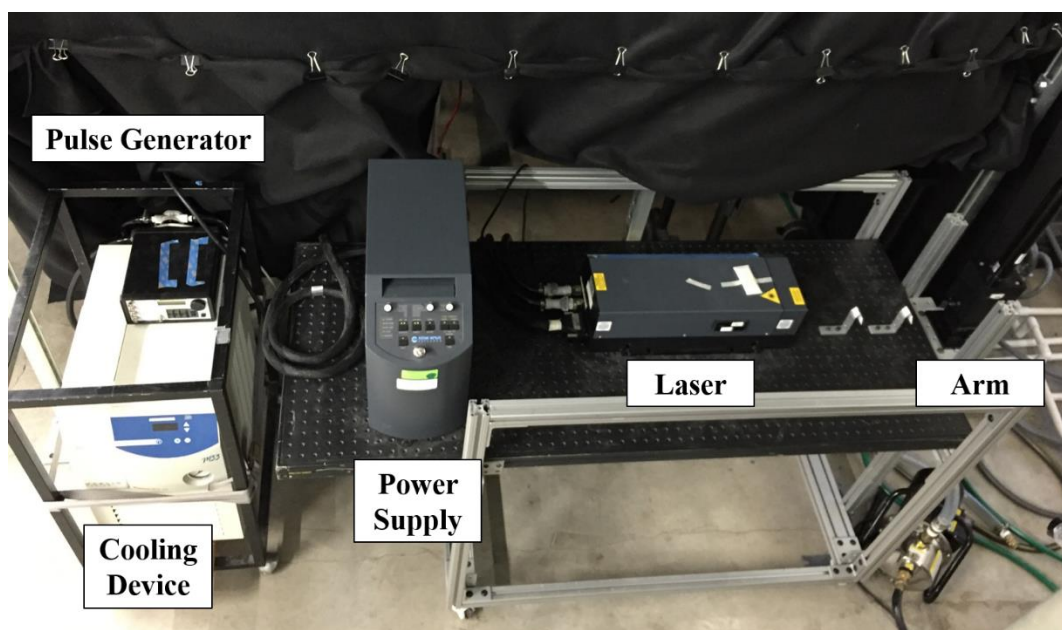


**Figure 4.5.** Overview of PIV laser system.

## 5. A SINGLE BUOYANT JET STUDY

In this chapter, the study focuses on the very simple basic geometry, boundary and initial condition: i.e., a single buoyant jet experiment. As a starting point of the multiple plume/jet experiments, the importance of a single buoyant jet experiment are superior and fundamental to the further experiments. Also there are many experimental and numerical literatures studied and analyzed on a single buoyant jet, thus it is the best practice for validating the test condition and numerical setup. However, the significance of the study differs from the other studies due to the range of the test condition and the test geometry. In the present experiment, we used the same setup for the PIV preliminary test with one exception to the laser system mentioned in the previous chapter. The sensitivity analysis provided the valid information of the pre-processing work that should be confirmed before analyzing the statistics. In the experiment result section, the statistically steady state results provide the value of this experiment and the important analysis of the study.

The present test condition is to simulate the natural circulation phase of the DCC event during the LOFC accident scenario without air ingress. During the DCC event, a rapid depressurization of the primary coolant and scram are initiated with the passive RCCS operational and without air ingress [7]. The decay heat from the core creates the relative high temperature distribution inside the core. When the temperature difference is sufficient to generate buoyancy force, the natural circulation phase begins. During this phase the flow reverses, i.e. flows from the outlet plenum pipe to the core region, enters

the upper plenum region, traverses down the channels on the core barrel, and exit through the pipe [31].

## **5.1 Turbulent Vertical Buoyant Jet**

Turbulent jets and plumes are classified as free shear flows. Free shear flows are inhomogeneous flows and remote from the solid body. The appearance of both jets and plumes are similar and they share similar characteristics in terms of turbulent motion: mixing with the ambient fluid is efficient; kinetic energy is lost to turbulence; momentum is conserved; and velocity and width of the jet/plume is a function of distance from the source. However, their fundamental mechanism is different. A jet is a flow driven by momentum of the source whereas a plume is driven by buoyancy of the source. Also, in the jet, mixing is directly related to the inertia of the turbulent eddies where in the plume, the buoyancy force produced the inertia, which lead to mixing [32]. If the mechanism is a combination of both momentum and buoyancy, it is called a buoyant jet or forced plume.

The present test condition is classified in a round turbulent vertical buoyant jet. The center line pipe is heated by a uniform heat flux and produces vertical natural convection which lead to vertical flow motion inside the pipe. However, the study is limited to the downstream of the pipe outlet because the physical information inside the heated pipe such as the boundary layer development and velocity or temperature distribution are not accessible due to the limitation of the test material (stainless steel) and geometry.

Turbulent plumes and jets are studied in many field of studies. In civil engineering, the discharge of waste such as the disposal of wastewater via ocean outfalls is of common interest. Geological volcanic fissure eruption on Earth generally forms turbulent buoyant plumes and jets. In nuclear engineering, when the reactor is shut down and the natural circulation is the only driving force, the decay heat from the core vessel creates the turbulent plumes and jets in both pressurized and depressurized loss-of-forced circulation accidents.

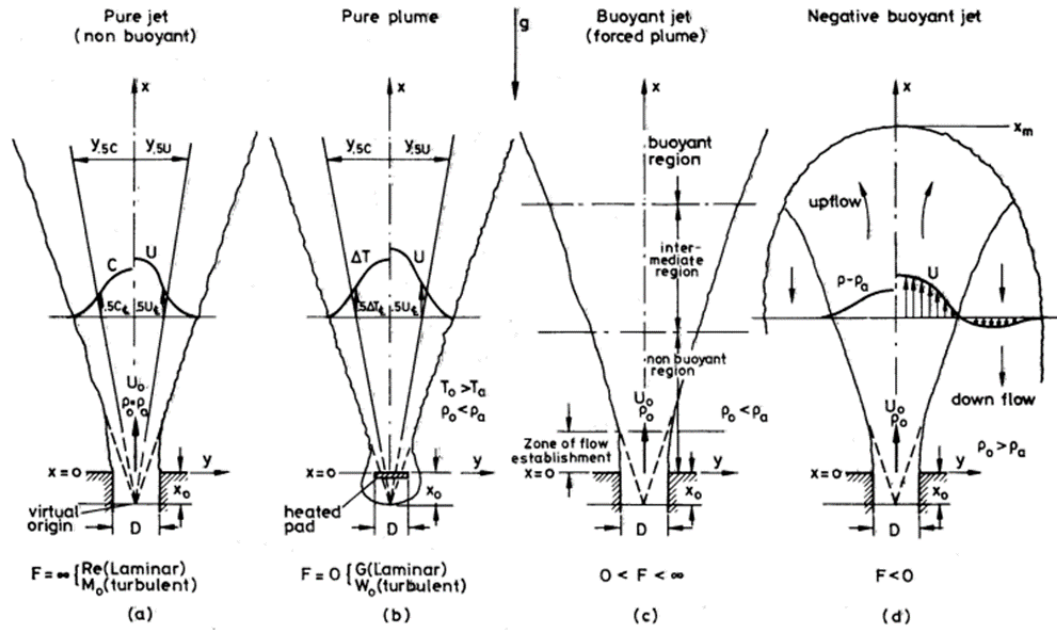


Figure 5.1. Buoyant jets in uniform surroundings [33].

Chen et al. [33], one of the pioneer of the turbulent buoyant jet study, classified four types of the buoyant jets in terms of source densimetric Froude number ( $Fr$ ) as shown



in Figure 5.1: pure jet, pure plume, buoyant jet (forced plume), and negative buoyant jet. Here the densimetric Froude number, which represents the ratio of inertial forces to buoyancy forces, is defined as

$$\text{Fr} = \frac{w_0}{\sqrt{\left(\frac{\Delta\rho_0}{\rho_a}\right)gD}} \quad (5.1)$$

where  $w_0$  is the velocity at the source,  $\Delta\rho_0 = |\rho_0 - \rho_a|$  is the density difference between the source fluid and the ambient fluid,  $\rho_a$  is the ambient density, and  $D$  is the size of the source (note: in his paper  $\text{Fr}^2 = F$ ). When the density of the discharge is the same as the environment so the buoyancy forces are absent, it is pure jet (a). When no initial momentum is generated and a heat source creates the buoyancy force to drive the flow, it is a pure plume (b). In a buoyant jet (forced plume), relatively lower density of fluid is discharged with the initial momentum (c). When the density of discharging fluid is higher than the environment, it is a negative buoyant jet (d). In our test condition, the higher temperature fluid which is heated inside the pipe, i.e. lower density fluid, is discharged through a nozzle therefore it is classified as buoyant jets or forced plumes. The buoyant jets have four different regions: Zone of flow establishment, non-buoyant region, intermediate region, and buoyant region.

The cylindrical coordinate system is chosen for the round buoyant jet as shown in Figure 5.2. The axial direction and velocity with the origin at the center of the round nozzle exit are represented by  $z$  and  $w$  respectively while the radial directions are denoted by  $r$  and  $u$ , respectively. The ambient temperature is denoted by  $T_a$ . The fluctuating velocities

are denoted by the apostrophe ('); for example, the fluctuating axial velocity is denoted by  $w'$ . The averaged velocities are denoted by the angled bracket  $\langle \rangle$  and determined by time averaging. Therefore, the instantaneous velocities ( $\sim$ ) are composed of mean and fluctuating components by using Reynolds decomposition.

$$\tilde{v}_i = v_i + v'_i \quad (5.2)$$

where  $v$  is the tensor notation ( $i = 1, 2, 3$ ). Therefore each of the cylindrical component can be written as follows:

$$\begin{array}{ll} \text{Radial Component}(r) & : \tilde{u} = u + u' \\ \text{Axial Component}(z) & : \tilde{w} = w + w' \\ \text{Azimuthal Component}(\theta) & : \tilde{v}_\theta = v_\theta + v'_\theta \\ \text{Temperature} & : \tilde{T} = T + T' \\ \text{Concentration} & : \tilde{c} = c + c' \\ \text{Reduced gravity} & : \tilde{g}' = g' + g'' \end{array} \quad (5.3)$$

where the reduced gravity, the buoyancy force per unit mass of the jet/plume fluid  $g'(r, z) = g(\rho_0 - \rho_a) / \rho_a$ , have the same profile as the concentration of any tracer [33].

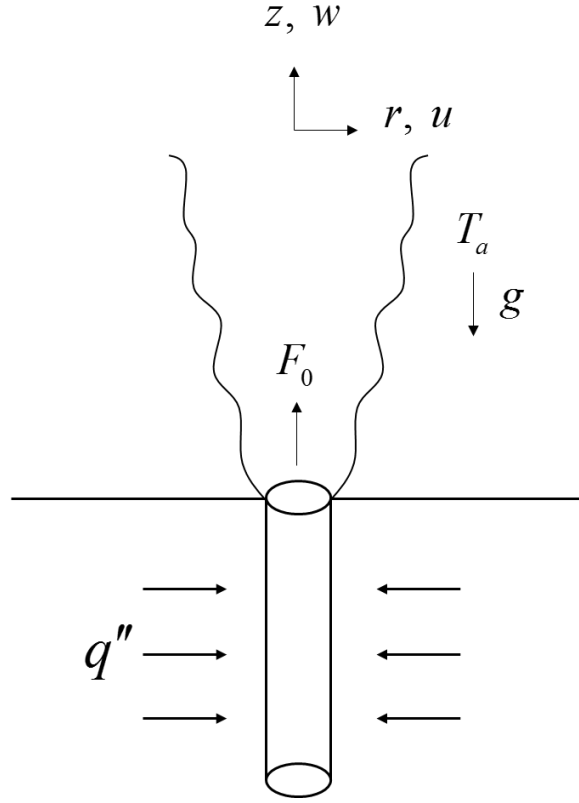


**Figure 5.2.** A cylindrical coordinate system and nomenclature.

The governing equations for mass, momentum, and buoyancy with the Boussinesq approximation and negligible viscous effects are given by

$$\frac{1}{r} \frac{\partial(ru)}{\partial r} + \frac{\partial w}{\partial z} = 0 \quad (5.4)$$

$$u \frac{\partial w}{\partial r} + w \frac{\partial w}{\partial z} = -\frac{1}{r} \frac{\partial}{\partial r} (r \langle u'w' \rangle) - \frac{\partial}{\partial z} (\langle w'^2 \rangle - \langle u'^2 \rangle) + g \beta \Delta T \quad (5.5)$$

$$u \frac{\partial g'}{\partial r} + w \frac{\partial g'}{\partial z} = -\frac{1}{r} \frac{\partial}{\partial r} (r \langle u'g' \rangle) - \frac{\partial}{\partial z} (\langle w'g' \rangle) \quad (5.6)$$

where  $\beta$  is the thermal expansion coefficient,  $\Delta T$  is the temperature difference between ambient temperature  $\Delta T = T - T_a$  and  $g$  is the gravitational acceleration. The concentration

$c$  can be replaced by the reduced gravity  $g'$  in Equation (5.6) that yields the advection-diffusion equation. Note that assumptions are made according to the analysis done by Hussein et al. [34] where the term  $\partial \langle u'^2 \rangle / \partial z$  in Equation (5.5) is obtained from the axial pressure gradient  $(-1/\rho)(\partial P / \partial z)$  by integrating the radial momentum equation.

Studies on the vertical axisymmetric jet/plume show that the profiles of axial velocity and reduced gravity can be well described by Gaussian functions at distances  $z/D > 5$  where  $D$  is the nozzle diameter [35].

$$w(r, z) = w_c(z) \exp \left\{ \frac{-r^2}{b^2(z)} \right\} \quad (5.7)$$

$$g'(r, z) = g'_c(z) \exp \left\{ \frac{-r^2}{\lambda^2 b^2(z)} \right\} \quad (5.8)$$

where the subscript  $c$  represents the mean vertical centerline location so that  $w_c(r, z) = w(0, z)$ ,  $b$  is the jet width where the velocity is equal to  $1/e$  of the centerline value and  $\lambda$  is the ratio between the diffusion of mass and momentum. Note that the jet width  $b$  is a function of  $z$ -direction.

One pioneering analysis for turbulent buoyant plumes and jets was reported by Morton et al. [36] where they introduced mean fluxes of volume  $Q$ , specific momentum  $M$  and specific buoyancy  $B$  defined as

$$\begin{aligned} Q(z) &= 2\pi \int_0^\infty w(r, z) r dr \\ M(z) &= 2\pi \int_0^\infty w^2(r, z) r dr \\ B(z) &= 2\pi \int_0^\infty w(r, z) g'(r, z) r dr \end{aligned} \quad (5.9)$$

A Morton length scale is defined as Equation (5.10).

$$l_s = \frac{(M_0)^{\frac{3}{4}}}{(B_0)^{\frac{1}{2}}} \quad (5.10)$$

The Morton length scale provides the criteria of the contribution of jets and plumes. The research done by Papanicolaou and List [37] showed that when  $z/l_s < 1$  the buoyant jet behaves like a jet due to the initial momentum while when  $z/l_s > 5$  it behaves like a plume.

## 5.2 Scaling of Mixing of Jet Flows entering the Upper Plenum

The objective of our study is to understand the flow behavior of the upper plenum during DCC event. The flow into the upper plenum is more complicated than a single buoyant jet and involves multiple intersecting jets and the interactions of the jets with surrounding components. According to Peterson [38], the divergence angle of a single buoyant jet is  $20^\circ$  and is independent of Reynolds number. Therefore, scaling of jet intersection and jet co-mixing is solely dependent on geometry. Through the geometric scaling analysis performed in Chapter 2, the pitch to diameter ratio ( $P/D_{\text{Hole}}$ ) for both full-scale and model was estimated 2.03 of the geometry, i.e. the turbulent jet mixing phenomena, for full-scale jets and model jets are well scaled (Figure 5.3). The one significant trade-off of this approach is that the ratio of jet diameter ( $D_{\text{Hole}}$ ) divided by upper plenum radius ( $D_{\text{CID}}/2$ ) is larger than prototypical, which will reduce the amount of mixing in the fluid that reaches the upper plenum boundary.

Jet Reynolds number should be sufficiently large that a turbulent buoyant jet is insured. According to Tritton [39], the critical Reynolds number based on the jet diameter ( $Re_D$ ) should be larger than a few  $10^3$ 's. In general, jets that are laminar within the confined channel, in our case heated pipes, are turbulent when they become free. The Coanda effect, the tendency of a fluid jet to stay attached to a convex surface, will increase the divergence angle between closely spaced jets and draw jets to nearby walls. The Coanda effect is caused by fluid entrainment into the jet, lowering the local pressure in the volume from

which the fluid is entrained. If jet entrainment is well scaled, then jet divergence angles should also be well scaled.

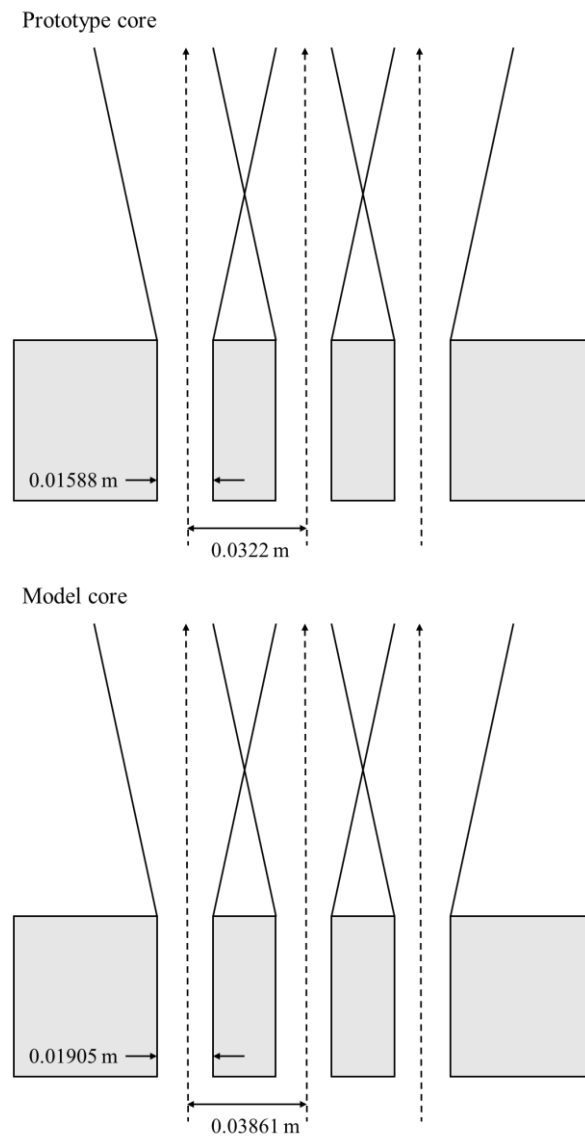


**Figure 5.3.** Turbulent buoyant jet mixing.

### 5.3 Experiment Method

A  $1/16^{\text{th}}$  scaled VHTR test facility was developed for the turbulent buoyant jet experiment. The test facility with measuring instruments are shown in Figure 5.4 to 5.6. Two thermocouples were located at 1 inch below/above the heating pipe's inlet/outlet, which was named in c1t (center group-1-top) and c1b (center group-1-bottom) respectively. Also four thermocouples were located at the system inlet/outlet, i.e. the inflow/outflow pipe line from the water reservoir, and cooling jacket inlet/outlet to monitor the steady state temperature for the system and estimate the rate of heat transfer on the heat sink.

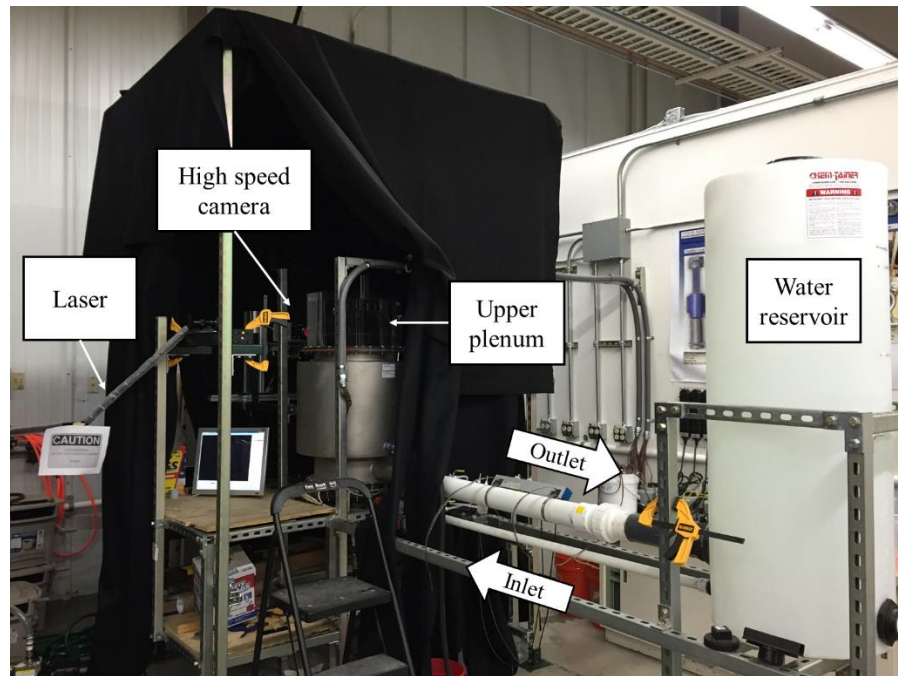


**Figure 5.4.** Experiment test facility:  $1/16^{\text{th}}$  scaled VHTR with the upper plenum. The PIV laser system with the high speed camera. The system inlet/outlet pipe lines. The water reservoir.



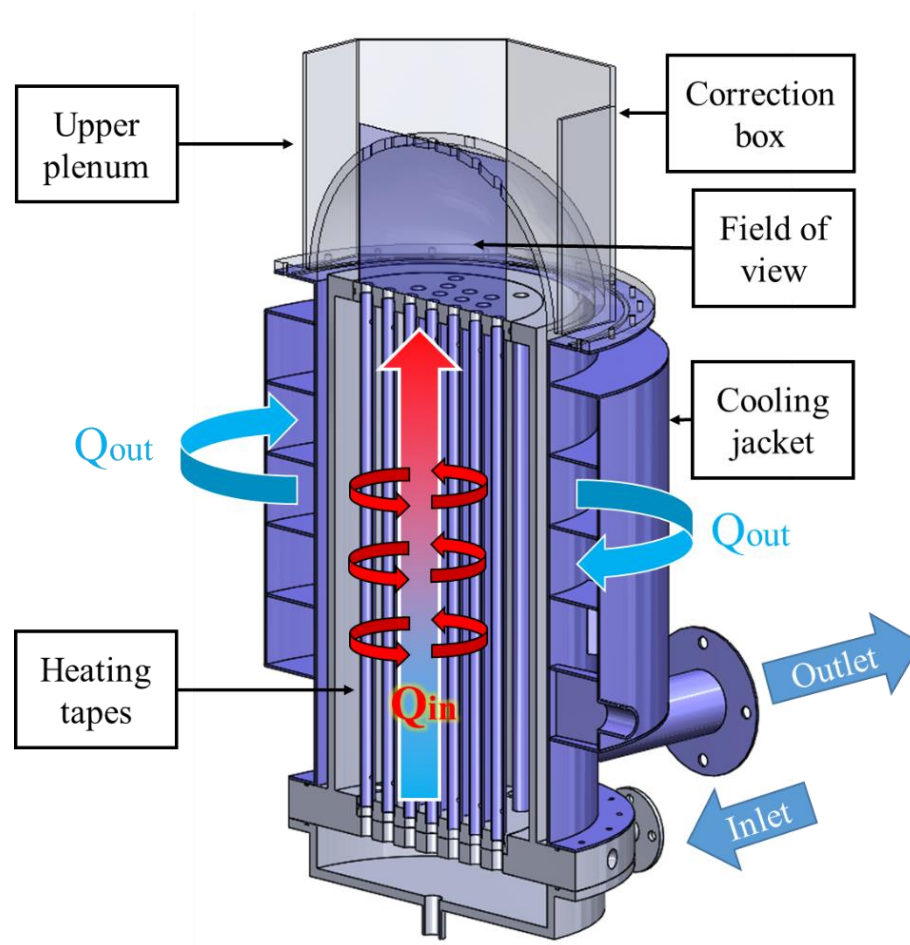


**Figure 5.5.** VHTR test cross section view.

Two optical filters, a polarizer and orange bandpass filter, were used in the PIV laser/camera system as shown in Figure 5.6. A polarizer was placed in the plane perpendicular to the camera and the field of view (FOV) to remove reflections, i.e. undefined or mixed polarization into a beam. An orange bandpass filter was used to remove the background image from the FOV to ease post-processing as shown in Figure 5.8.

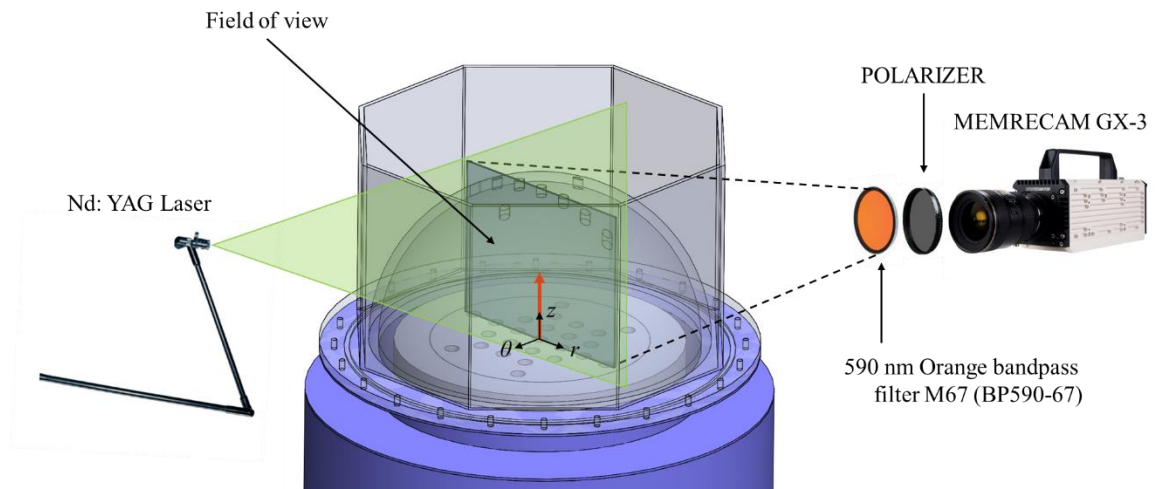


**Figure 5.6.** Schematic of PIV laser and camera system. The origin of a cylindrical coordinate system is located at the center of the pipe outlet.

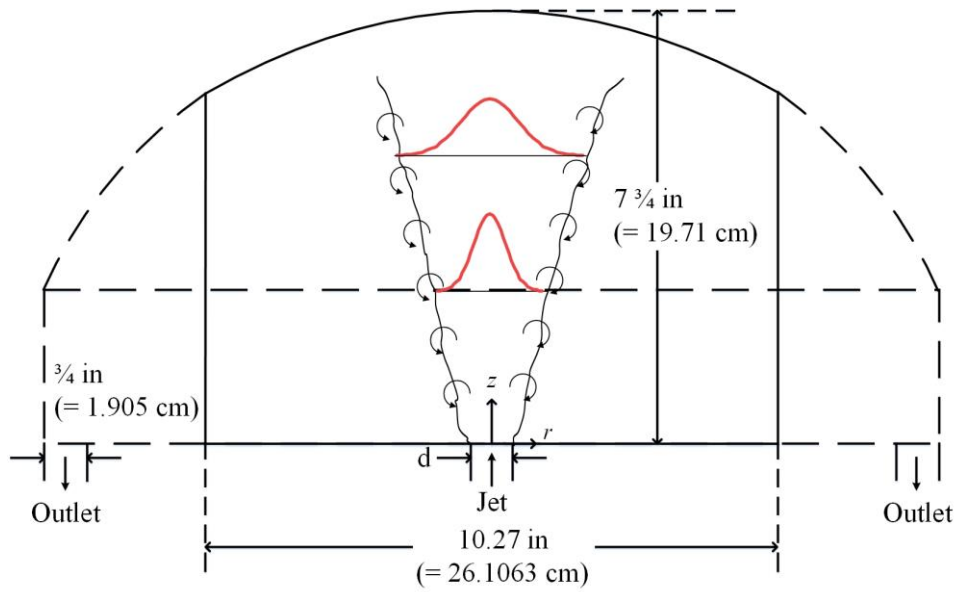


**Figure 5.7.** Schematics of the test section (solid and dotted line) and region of interest (solid line).

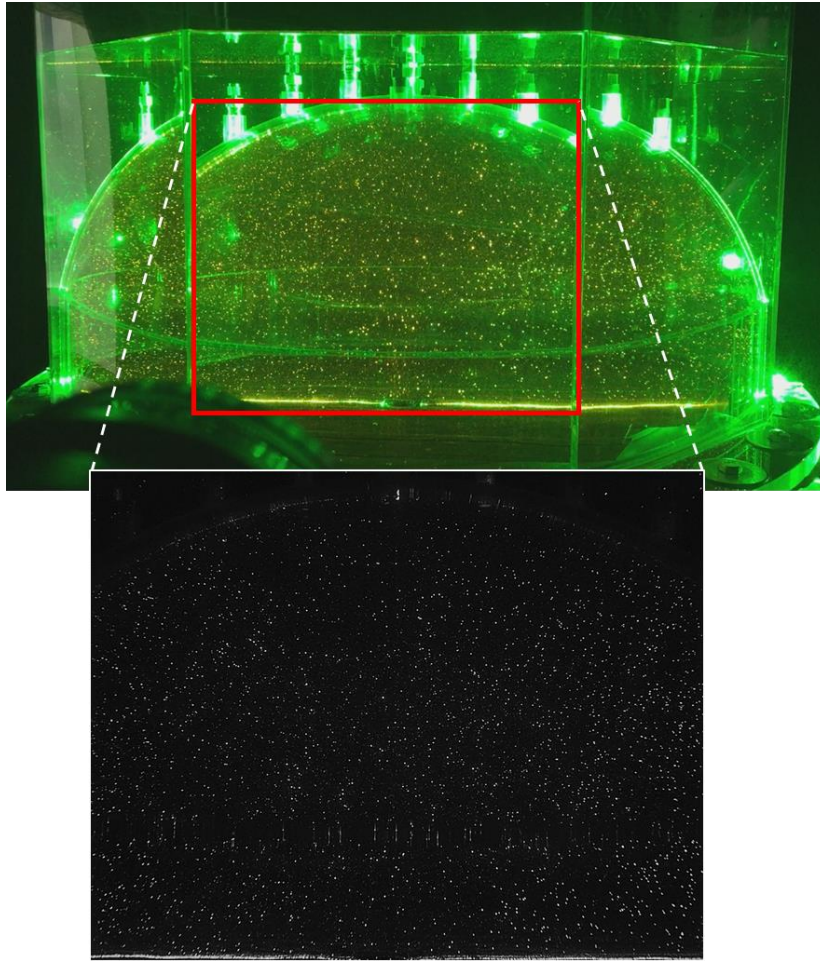


**Figure 5.8.** Real time experiment image (top) with the green laser sheet and orange fluorescent particles and filtered image (bottom) after the polarizer and orange bandpass filter in the field of view (red box). The color of orange fluorescent particles is orange (top) and white (bottom).

A size of the region of interest (ROI) was close to FOV since the only difference was the dome shape on the top edge of the FOV, which was removed during post-processing. The FOV, shown in Figure 5.9 red line, was chosen to capture up to 5 pipe outlet flow behavior for further study. The restriction was made due to the curvature of the correction box, which did not allow for an extended view to the maximum number of jets.

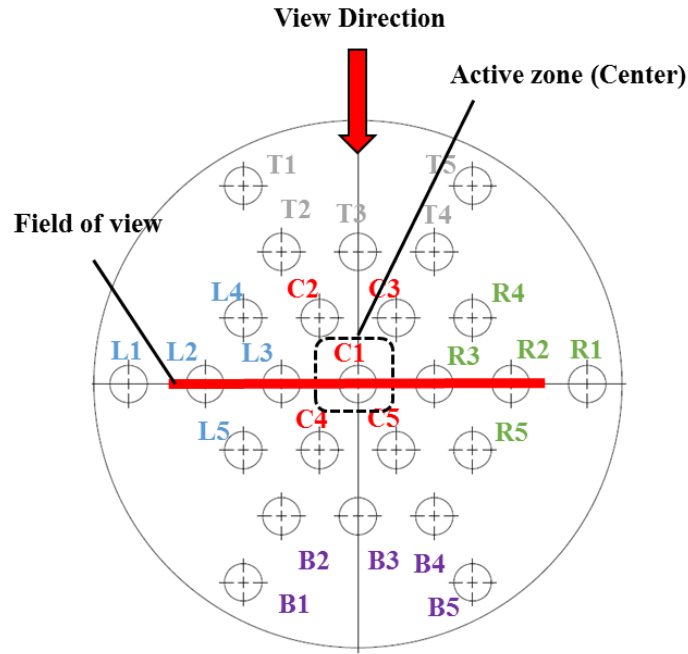


**Figure 5.9.** Pipe layout, test section and a center pipe (C1) plan view.

A flow visualization method for the experiment is the same as the preliminary experiment: the PIV method. The only difference is the laser system; a Nd:YAG laser system made by New Wave Research. Table 5.1 shows the list of the experiment setup used for the single buoyant jet study and Table 5.2 shows its PIV settings for the analysis. Similar to the preliminary test, PIVlab, the MATLAB software, version 1.41 was used for PIV analysis.

**Table 5.1.** PIV camera and laser test conditions.

Application	Turbulent buoyant jet
Flow geometry	Parallel to light sheet
Field of view	261.1 x 197.1 mm <sup>2</sup>
Observation Distance	$y_0 = 0.645$ m
Recording method	Single frame / double exposure ( $\Delta t = 100$ ms)
Recording lens	$f = 50$ mm, $f_{\#} = 2$
Recording medium	Carl Zeiss Makro-Planar T* 2/50 ZF.2
Ambiguity removal	Polarizer / 590 nm orange bandpass filter M67 (BP590-67)
Illumination	Nd:YAG laser 15 mJ/pulse
Pulse delay	Continuous
Seeding material	Polyethylene microsphere ( $d_p = 53 - 63$ $\mu\text{m}$ )
Seeding type	Fluorescent orange
Camera resolution	1280 x 1024 pixel

**Table 5.2.** PIV computation settings.

Evaluation method	Fully digital evolution, cross correlation
Peak finding	2x3 point Gaussian fit
Size of interrogation area	64 x 64, 32 x 32, 16 x 16 pixel
Size of FFT	64 x 64, 32 x 32, 16 x 16 pixel
Grid distance	32 x 32, 16 x 16, 8 x 8 pixel
Overlap of interrogation area	50%

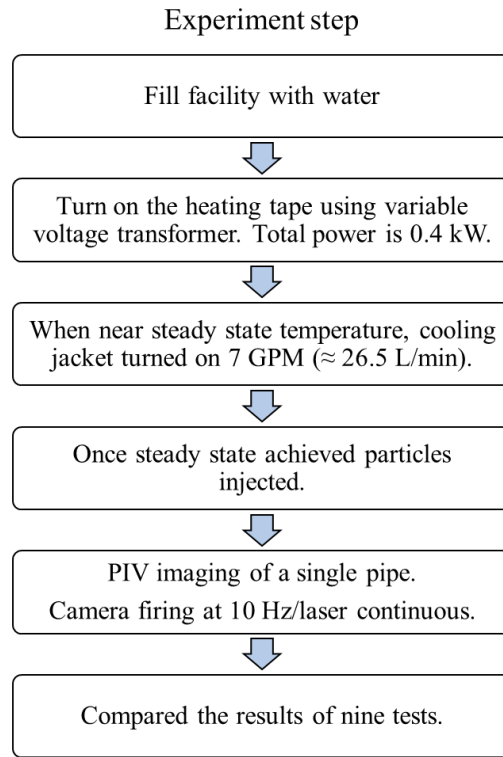


**Figure 5.10.** Experiment test procedure for PIV.

Nine tests were performed and compared for a single buoyant jet study; they followed the same experiment steps as shown in Figure 5.10. The maximum power of 0.4 kW was applied for the variable voltage transformer. The power is sufficient for flow to become turbulent when it exits from the pipe outlet. The cooling jacket was turned on to 7 GPM when the system was close to the steady state temperature to cool down the reactor vessel. The steady state temperature was achieved when the difference of the system inlet/outlet temperature reached  $\pm 0.5$  °C, which is the accuracy of the thermocouple.

A number of dimensionless numbers have been used to comprehend the physical interpretation of the present test condition which is shown in Table 5.3. The definition of each dimensionless number is in Equation (5.11) to (5.14),

$$\text{Re} = \frac{w_0 D}{\nu_0} \quad (5.11)$$

$$\text{Gr} = \frac{g \beta (T_0 - T_\infty) D^3}{\nu_0^2} \quad (5.12)$$

$$\text{Ri} = \frac{g \beta (T_0 - T_\infty) D}{w_0^2} = \frac{\text{Gr}}{\text{Re}^2} \quad (5.13)$$

$$\text{Ra} = \frac{g \beta (T_0 - T_\infty) D^3}{\nu_0 \alpha} = \text{Gr} \cdot \text{Pr} \quad (5.14)$$

where  $w_0$  is the nozzle top-hat velocity (i.e. assuming constant velocity distribution across the jet),  $D$  is the nozzle diameter,  $\nu_0$  is the viscosity at the nozzle,  $T_0$  is the temperature at the nozzle,  $T_\infty$  is the ambient temperature,  $\beta$  is the thermal expansion coefficient at the nozzle temperature,  $\alpha$  is the thermal diffusivity at the nozzle.

The  $\text{Re}$  is sufficiently large to generate turbulent jets. The Grashof number ( $\text{Gr}$ ) measures the ratio of the buoyancy to viscous forcing acting on a fluid. The  $\text{Gr}$  is not enough to induce the transition to turbulent flow for natural convection from the coolant pipe. However, when the flow exits from the nozzle, high entrainment of the fluid from the ambient flow enhances the flow becomes turbulent. The Richardson number ( $\text{Ri}$ ) measures the ratio of buoyant to inertial forces. The  $\text{Ri}$  is the criteria to determine whether the flow is governed by either natural or forced convection. Typically when  $\text{Ri} < 0.1$  the natural convection is negligible and when  $\text{Ri} > 10$  forced convection is negligible. However, like the present test condition where  $0.1 < \text{Ri} < 10$ , neither of them is negligible. Both mechanisms are important in the present study and corresponds to the range of  $\text{Fr}$ . The Rayleigh number ( $\text{Ra}$ ) is just the product of  $\text{Gr}$  and  $\text{Pr}$ . The  $\text{Ra}$  measures the heat

transfer mechanism, either conduction or convection, associated with buoyancy driven flow. When the Ra is less than  $10^8$  the flow is laminar and when the Ra is high than  $10^{10}$ , the flow is fully turbulent. Again the Ra is not sufficient for the beginning of turbulence in natural convection in the vertical channel flow; consequently, the Re insures the jet becomes turbulent.

**Table 5.3.** Dimensionless numbers of the present test condition

Dimensionless number	Acronym	Value (Average)
Reynolds number	Re	227 - 450 (351)
Grashof number	Gr	$1.3 - 2.73 (2.04) \times 10^5$
Richardson number	Ri	$1.35 - 2.52 (1.66)$
Rayleigh number	Ra	$0.79 - 1.55 (1.19) \times 10^6$
Densimetric Froude number	Fr	0.57-1.01 (0.81)



## 5.4 Experiment Result

Time-averaged profiles were achieved by averaging 3,000 PIV frames with 1-2, 2-3, 3-4 ... image sequencing style. Since images were recorded by 10 Hz (= 100 ms), the total time for the steady state profiles were determined by Reynolds-averaging for 300 seconds (= 5 minutes). After obtaining time-averaged profiles, ensemble-averaged profiles were evaluated by averaging nine experiment test results. Figure 5.11 to 5.13 show ensemble-averaged profiles of Reynolds-averaged first-order statistics, second-order statistics, turbulent kinetic energy ( $k$ ) and turbulent intensity ( $TI$ ).

The radial velocity  $u$  shows that the maximum (-0.68 cm/s) and minimum (0.69 cm/s) values were obtained close to the dome surface at  $r = -6.06$  cm and 6.10 cm, respectively and in time it was right after impinging to the highest point. Close to the jet inlet a symmetrical right-hand and left-hand side radial velocity were formed due to the Rayleigh-Taylor (RT) instability which occurs when relatively lighter fluid pushes the heavier fluid. At the beginning, the lighter fluid accumulates adjacent fluids until it reaches a sufficiently large volume to burst out of the fluid upward creating RT instability [40-43]. This instability of two different density fluids creates vorticity along the interface and entrains the heavier fluid toward the lighter fluid. This vorticity form a large toroidal vortex with a diameter approximately equal to the jet inlet narrowing the jet fluid and accelerates the flow below. The accumulation of these fluid and acceleration can be observed from the temperature measured at the location 1 inch below the jet inlet as shown in Figure 5.14. The steep gradients of the  $u$  velocity indicates the existence of the jet

boundary and entrainment of the ambient fluid. The entrainment of the fluid gradually weakens as the jet flows upward; however due to the vortex created by the dome shape additional counter directional fields were formed below the impingement region where  $z = 13$  cm.

The axial velocity  $v$  shows almost symmetrical distribution across the ROI where the maximum velocity (1.57 cm/s) was obtained at  $z_m = 12.51$  cm as shown in Figure 5.15. The axial velocity is 2.28 times higher than the radial velocity. The mean velocity magnitude was estimated by the square-root of the axial and radial velocity. The standard deviation of the radial and axial velocity were maximized near the jet inlet because the high volume of fluid were entrained and the toroidal vortex increased the velocity magnitude. Turbulent kinetic energy, turbulent viscosity and turbulent intensities were defined as follows:

$$k = \frac{1}{2} \left( \langle u'^2 \rangle + \langle v'^2 \rangle \right) \quad (5.15)$$

$$\nu_t = \frac{\langle u'w' \rangle}{-\frac{\partial \langle w \rangle}{\partial r}} \quad (5.16)$$

$$TI_u = \frac{u_{std}}{u}, TI_w = \frac{w_{std}}{w} \quad (5.17)$$

where  $u_{std}$  and  $w_{std}$  are the root-mean-square (RMS) or standard deviation of the turbulent velocity fluctuations ( $u'$  and  $w'$ ).  $TI$  goes extremely high values toward the jet boundaries although the Reynolds stresses decay along the vertical direction. The turbulent viscosity is positive since  $\partial \langle w \rangle / \partial r$  is negative where the Reynolds stress  $\langle u'w' \rangle$  is positive and vice versa.

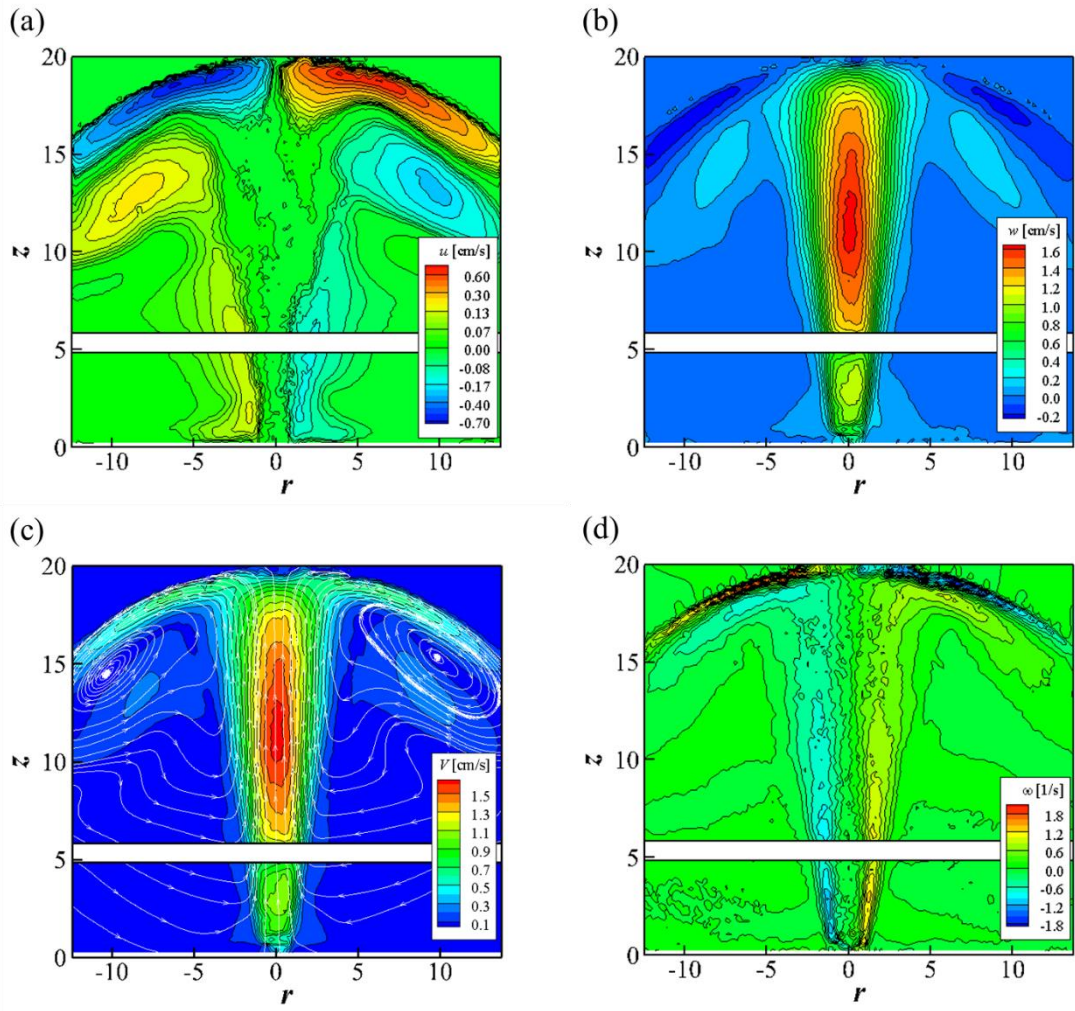


**Figure 5.11.** Contours of averaged single buoyant jet; (a) mean radial velocity; (b) mean axial velocity; (c) mean velocity magnitude with streamlines; (d) vorticity ( $\omega$ ).

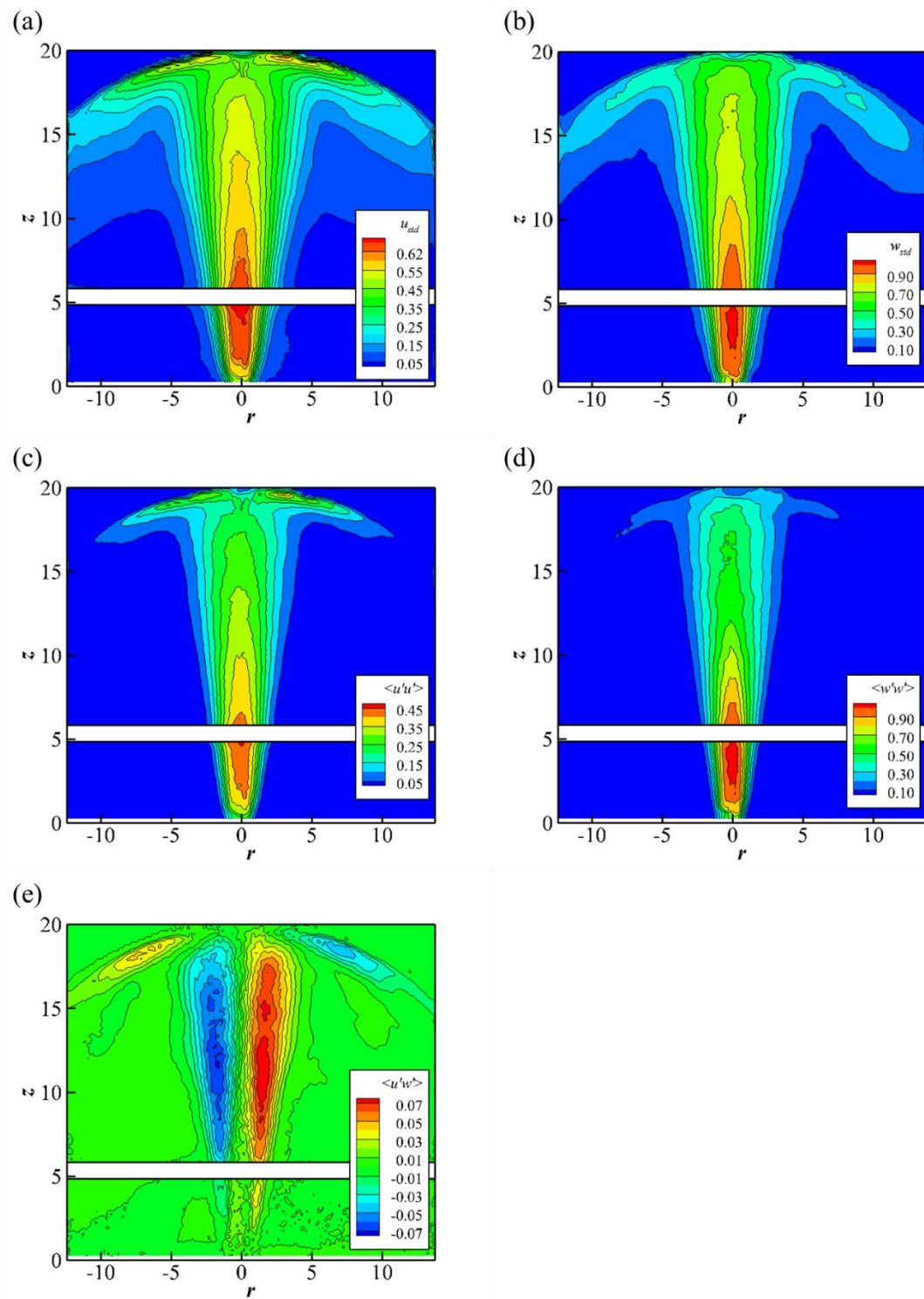


**Figure 5.12.** Contours of averaged single buoyant jet; (a) standard deviation of radial velocity; (b) standard deviation of axial velocity; (c) Reynolds stress  $\langle u'u' \rangle$ ; (d) Reynolds stress  $\langle w'w' \rangle$ ; (e) Reynolds stress  $\langle u'w' \rangle$ .

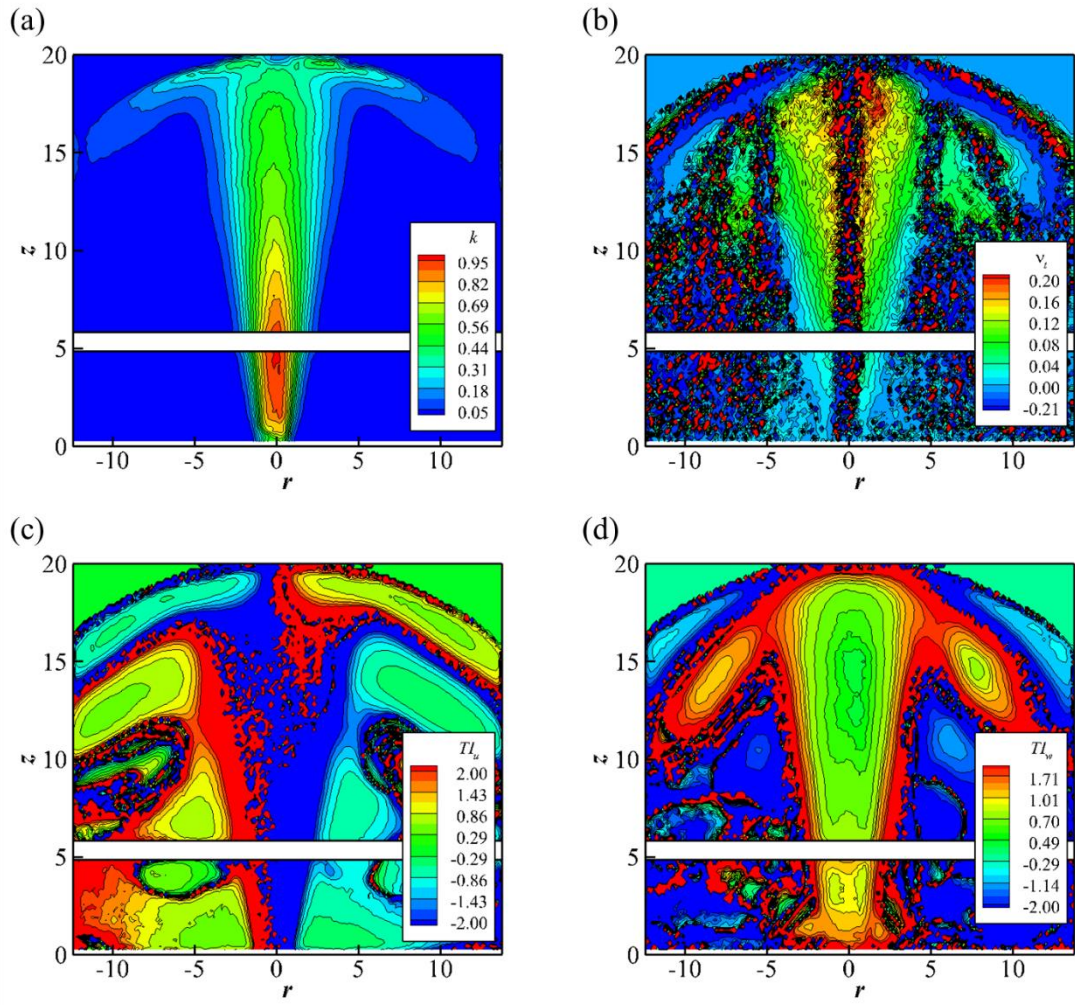


**Figure 5.13.** Contours of averaged single buoyant jet; (a) Turbulent kinetic energy ( $k$ ); (b) turbulent viscosity ( $\nu_t$ ); (c) turbulent intensity in radial direction; (d) turbulent intensity in axial direction.

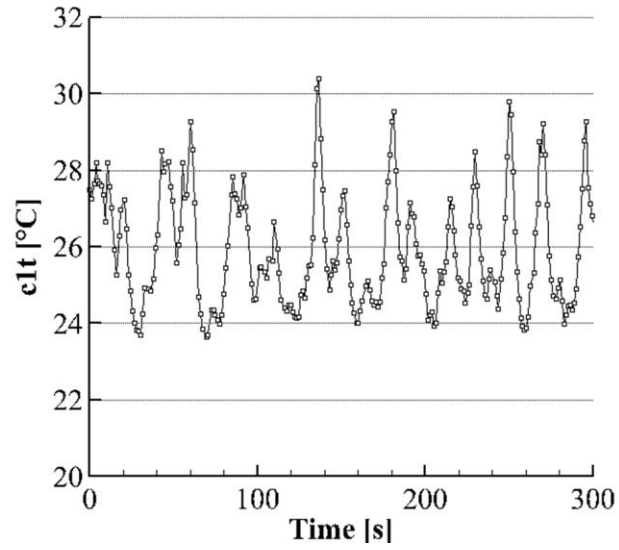


**Figure 5.14.** Time series of temperature at location  $r = 0$  cm,  $z = - 2.54$  cm in Test 8. The passage of 7 puff cycles is observed.

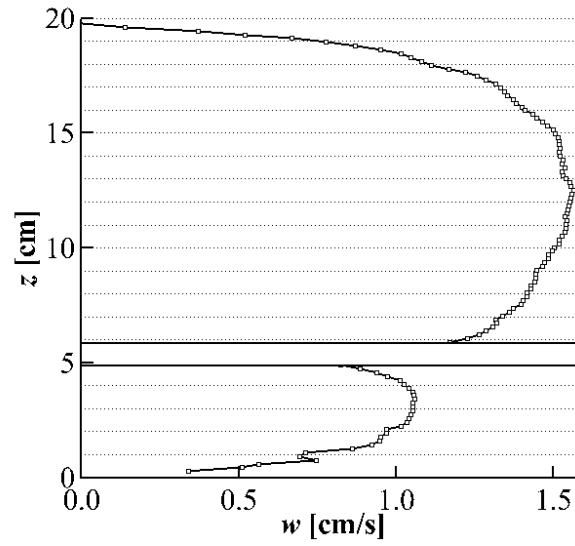


**Figure 5.15.** The axial velocity distribution along the  $z$ -direction at  $r = 0$  cm. The maximum velocity is obtained at  $z = 12.51$  cm.

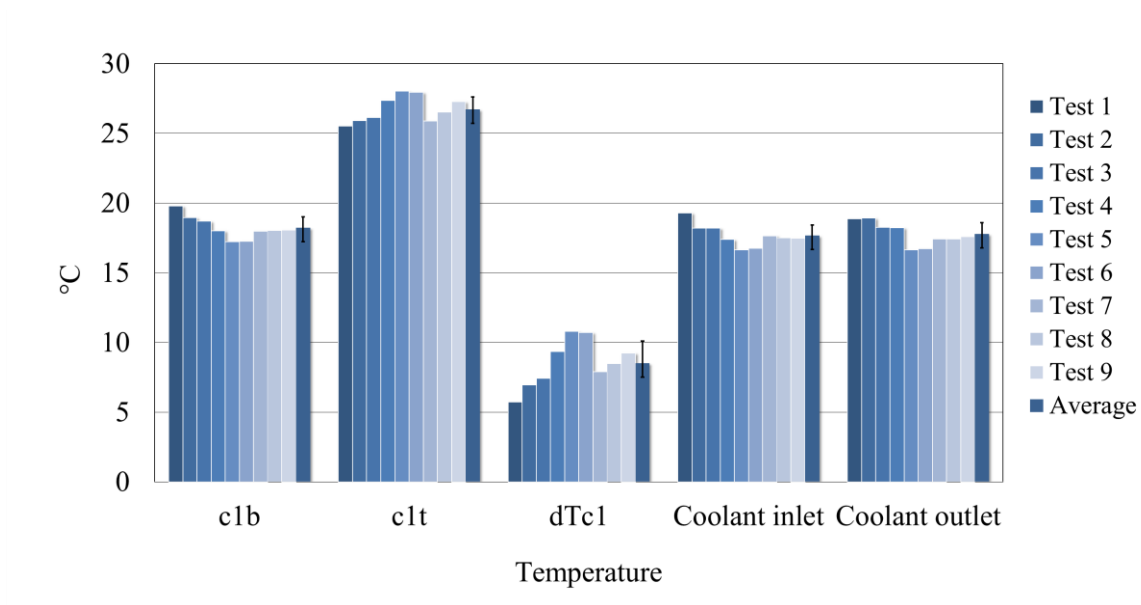


**Figure 5.16.** Temperature data at each location for nine test results and averaged temperature data.

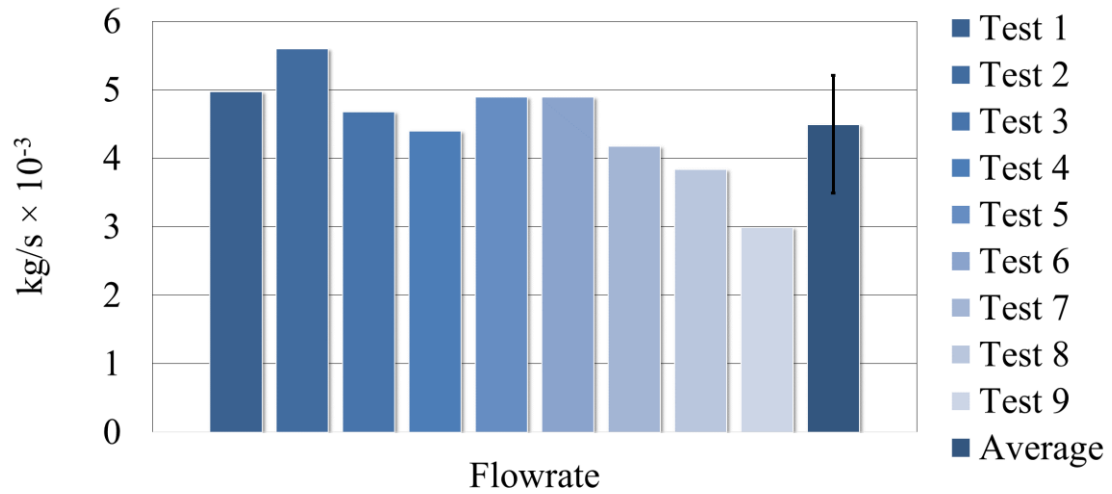


**Figure 5.17.** Flowrate data at each location for nine test results and averaged flowrate data.



A jet boundary is defined as a jet width  $b$  as shown in Figure 5.18. The entrainment coefficient  $\alpha_e$  and spreading rate  $\alpha_s$  are defined as follows.

$$\alpha_e(z) = \frac{u_e(z)}{w_c(z)} \quad (5.18)$$

$$\alpha_s(z) = \frac{b(z)}{z} \quad (5.19)$$

where  $u_e(z) = |u|_{r=\pm\infty}$  = entrainment velocity. The entrainment velocity  $u_e$  is proportional to the jet centerline velocity  $w_c$ .

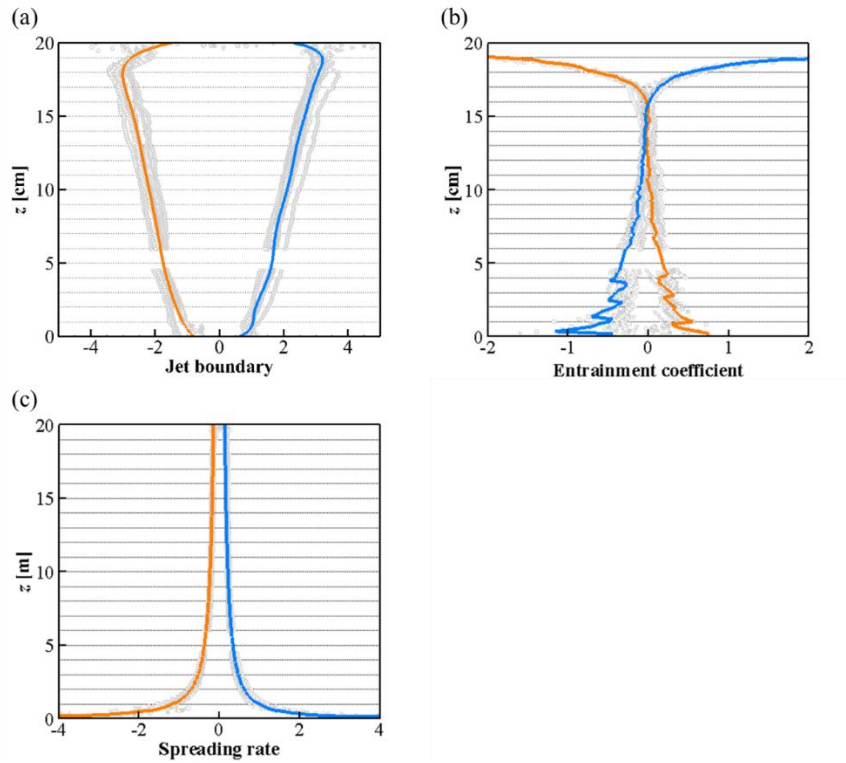


**Figure 5.18.** The characteristics of a single buoyant jet. (a) jet boundary, (b) entrainment coefficient, and (c) spreading rate. The orange line indicates the left-hand side value while the blue line represents the right-hand side value.



Self-similarity is an important concept in a jet and plume study because it provides the general behavior of buoyant jets. After the flow is developed from the jet inlet time-averaged profiles show a Gaussian distribution. When these profiles collapse into a single Gaussian profile, the turbulent structure reaches self-preserving. Many authors from different studies define the transition of this self-similarity with slightly different parameters. Two very common parameters are  $(z - z_0)/D$  or  $z/D$  and  $(z - z_0)/l_s$  where  $z_0$  is a virtual origin where two jet boundaries are met,  $D$  is a diameter of the jet inlet and  $l_s$  is a Morton length scale defined in Equation (5.10). However, the studies were limited to free jets where jets develop without bound [37, 44, 45]. The present results show when and where these self-similarity patterns were observed in the dome shaped geometry. The velocity and radial distribution profiles were non-dimensionalized by the centerline axial velocity  $w_c$  and  $(z - z_0)$ , respectively.

Self-similarity profiles were well observed in the axial velocity and velocity magnitude profile regardless of  $z/D$  where the radial velocity did not show any similarity pattern. This is due to the big counter rotating vortices located near the dome surface. The normal components of Reynolds stresses have self-similarity within the range of  $z/D > 5.78$  where  $\langle u'w' \rangle$  reaches within the range of  $1.61 < z/D < 8.91$ .

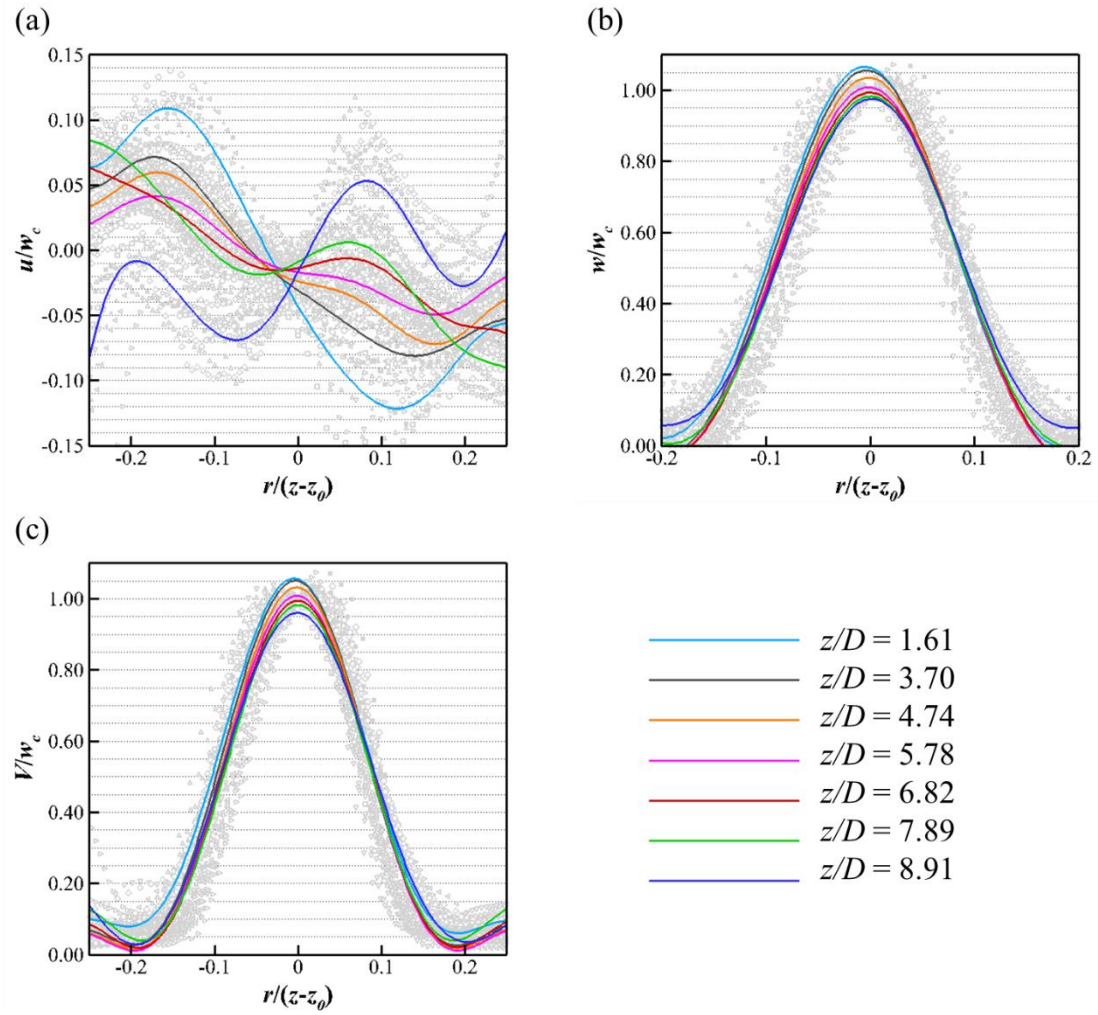


**Figure 5.19.** Radial profiles of non-dimensional (a) radial velocity, (b) axial velocity, (c) velocity magnitude within a single buoyant jet.

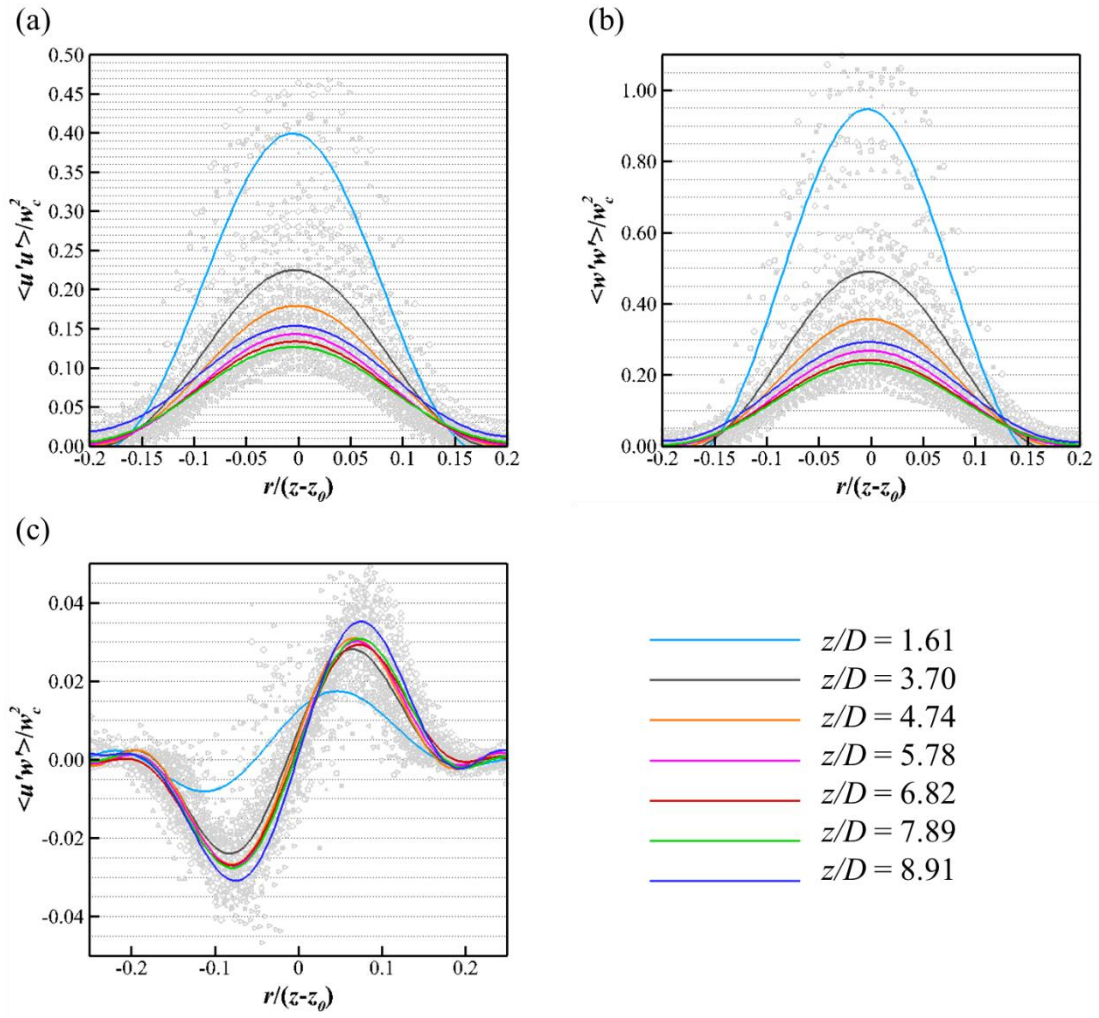


**Figure 5.20.** Radial profiles of non-dimensional Reynolds stresses ((a) - (c)) within a single buoyant jet.

## 6. CONCLUTION AND FUTURE WORK

A turbulent single buoyant jet study was performed for the case of LOFC in the upper plenum of scaled VHTR. Time-averaged profiles show that 3,000 frames of images were sufficient for the study up to second-order statistics. Self-similarity is an important feature of jets since the behavior of jets is independent of Reynolds number and a sole function of geometry. Self-similarity profiles were well observed in the axial velocity and velocity magnitude profile regardless of  $z/D$  where the radial velocity did not show any similarity pattern. The normal components of Reynolds stresses have self-similarity within the range of  $z/D > 5.78$  where  $\langle u'w' \rangle$  reaches within the range of  $1.61 < z/D < 8.91$ . The study shows that large vortices were observed close to the dome wall, indicating that the geometry of the VHTR has a significant impact on its safety and performance. Near the dome surface, large vortices were shown to inhibit the flows, resulting in reduced axial jet velocity. The vortices that develop subsequently reduce the Reynolds stresses that develop and the impact on the integrity of the VHTR upper plenum surface.

## REFERENCES

1. *BP statistical review of world energy* June 2015, BP.
2. *Technology roadmap: nuclear energy*. 2015, International Energy Agency (IEA).
3. *Technology roadmap update for generation IV nuclear energy systems*. December 2002, Gen IV International Forum (GIF).
4. Doug Chapin, S.K., Jim Nestell, *The very high temperature reactor: a technical summary*. 2004: MPR Associates Inc.
5. (INL), I.N.L., *Very high temperature reactor [VHTR]*, very-high-temperature-reactor.pdf, Editor.
6. Schultz, R.R., et al., *Studies related to the oregon state university high temperature test facility: scaling, the validation matrix, and similarities to the modular high temperature gas-cooled reactor*. 2010, Idaho National Laboratory (United States). Funding organisation: DOE-NE (United States).
7. PIRT, *Next generation nuclear plant phenomena identification and ranking tables (PIRTs)*. 2008.
8. Haque, H., W. Feltes, and G. Brinkmann, *Thermal response of a modular high temperature reactor during passive cooldown under pressurized and depressurized conditions*. Nuclear Engineering and Design, 2006. **236**(5–6): p. 475-484.
9. McIlroy, H., et al., *PIV experiments to measure flow phenomena in a scaled model of a VHTR lower plenum*. Idaho National Laboratory Report INL/INT-06-11740, 2006.
10. Gauthier, J.-C., et al., *ANTARES: The HTR/VHTR project at framatome ANP*. Nuclear Engineering and Design, 2006. **236**(5–6): p. 526-533.
11. Chang, J., et al., *A study of a nuclear hydrogen production demonstration plant*. Nuclear Engineering and Technology, 2007. **39**(2): p. 111.
12. Condie, K., et al., *Development of an experiment for measuring flow phenomena occurring in a lower plenum for VHTR CFD assessment*. 2005: Idaho National Laboratory.
13. Elder, R. and R. Allen, *Nuclear heat for hydrogen production: coupling a very high/high temperature reactor to a hydrogen production plant*. Progress in Nuclear Energy, 2009. **51**(3): p. 500-525.
14. Khamis, I. *Nuclear power plants can produce hydrogen to fuel the “hydrogen economy”*. in *ACS Press Conference*. 2012. San Diego, California: American Chemical Society
15. Chang, H.O., C. Davis, and R. Moore, *Development of safety analysis codes and experimental validation for a very high temperature gas-cooled reactor*. 2004, Idaho National Laboratory (INL).
16. Reyes Jr, J., et al., *Scaling analysis for the high temperature gas reactor test section (GRTS)*. Nuclear Engineering and Design, 2010. **240**(2): p. 397-404.

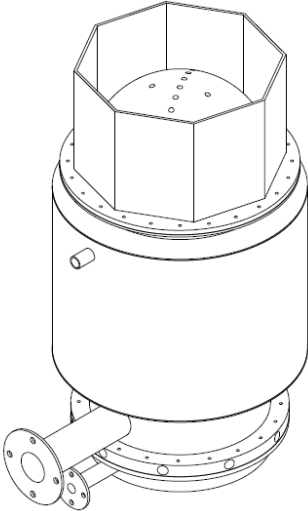
17. Gougar, H. and C. Davis, *Reactor pressure vessel temperature analysis for prismatic and pebble-bed VHTR designs*. Idaho National Laboratory, 2006.
18. Johnson, R.W., D.P. Guillen, and T. Gallaway, *Investigations of the application of CFD to flow expected in the lower plenum of the prismatic VHTR*. 2006: Idaho National Laboratory.
19. Tung, Y.-H. and R.W. Johnson. *CFD calculations of natural circulation in a high temperature gas reactor following pressurized circulator shutdown*. in *ASME 2011 International Mechanical Engineering Congress and Exposition*. 2011. American Society of Mechanical Engineers.
20. McVay, K.L., et al., *Preliminary tests of particle image velocimetry for the upper plenum of a scaled model of a very high temperature gas cooled reactor*. *Progress in Nuclear Energy*, 2015. **83**: p. 305-317.
21. Thielicke, W. and E.J. Stamhuis, *PIVlab—Towards user-friendly, affordable and accurate digital particle image velocimetry in MATLAB*. *Journal of Open Research Software*, 2014. **2**(1): p. e30.
22. Sanchez, T., et al., *Spontaneous motion in hierarchically assembled active matter*. *Nature*, 2012. **491**(7424): p. 431-434.
23. Booth-Gauthier, E.A., et al., *Force-induced changes in subnuclear movement and rheology*. *Biophysical journal*, 2012. **103**(12): p. 2423-2431.
24. Leong, T., et al., *The role of surfactant headgroup, chain length, and cavitation microstreaming on the growth of bubbles by rectified diffusion*. *The Journal of Physical Chemistry C*, 2011. **115**(49): p. 24310-24316.
25. Mirsepassi, A. and D. Rankin, *Particle image velocimetry in viscoelastic fluids and particle interaction effects*. *Experiments in Fluids*, 2013. **55**(1): p. 1-7.
26. Piro, V., N. Piro, and O. Piro, *Characterization of intraventricular blood flow using a microbubble-contrast tracking echo-PIV technique*. *Journal of the American College of Cardiology*, 2012. **59**(13s1): p. E1139-E1139.
27. Xu, H. and E. Bodenschatz, *Motion of Inertial Particles with Size Larger than Kolmogorov Scale in Turbulent Flows*. *Physica D: Nonlinear Phenomena*, 2008. **237**(14): p. 2095-2100.
28. Amini, N. and Y.A. Hassan, *Measurements of jet flows impinging into a channel containing a rod bundle using dynamic PIV*. *International Journal of Heat and Mass Transfer*, 2009. **52**(23–24): p. 5479-5495.
29. Pope, S.B., *Turbulent flows*. 2000: Cambridge university press.
30. McCreery, G.E., K.G. Condie, and R.R. Schultz, *Scaled experimental modeling of VHTR plenum flows*, in *Proceedings of the 15th International Conference on Nuclear Engineering (ICONE 15)*, Nagoya, Japan. 2007.
31. Aldridge, R.J., *Scaling Study of the Depressurized Conduction Cooldown Event in the High Temperature Test Facility Using REAL5-3D/ATHENA*, in *Nuclear Engineering*. 2013, Oregon State University.
32. Lee, J.H.W. and V.H. Chu, *Turbulent Jets and Plume: A Lagrangian Approach*. 2003: Springer Science+Business Media, LLC.
33. Chen, C.J. and W. Rodi, *Vertical turbulent buoyant jets: a review of experimental data*. NASA STI/Recon Technical Report A, 1980. **80**.

34. Hussein, H.J., S.P. Capp, and W.K. George, *Velocity measurements in a high-Reynolds-number, momentum-conserving, axisymmetric, turbulent jet*. Journal of Fluid Mechanics, 1994. **258**: p. 31-75.
35. Paillat, S. and E. Kaminski, *Entrainment in plane turbulent pure plumes*. Journal of Fluid Mechanics, 2014. **755**: p. R2.
36. Morton, B., G. Taylor, and J. Turner. *Turbulent gravitational convection from maintained and instantaneous sources*. in *Proceedings of the Royal Society of London A: Mathematical, Physical and Engineering Sciences*. 1956. The Royal Society.
37. Papanicolaou, P.N. and E.J. List, *Investigations of round vertical turbulent buoyant jets*. Journal of Fluid Mechanics, 1988. **195**: p. 341-391.
38. Peterson, P., *Scaling and analysis of mixing in large stratified volumes*. International Journal of Heat and Mass Transfer, 1994. **37**: p. 97-106.
39. Tritton, D.J., *Physical Fluid Dynamics*. 1977, New York: Van Nostrand Reinhold.
40. O'hern, T., et al., *Experimental study of a turbulent buoyant helium plume*. Journal of Fluid Mechanics, 2005. **544**: p. 143-171.
41. Soteriou, M.C., Y. Dong, and B.M. Cetegen, *Lagrangian simulation of the unsteady near field dynamics of planar buoyant plumes*. Physics of Fluids, 2002. **14**(9): p. 3118-3140.
42. Cetegen, B.M. and T.A. Ahmed, *Experiments on the periodic instability of buoyant plumes and pool fires*. Combustion and Flame, 1993. **93**(1-2): p. 157-184.
43. Cetegen, B.M. and K.D. Kasper, *Experiments on the oscillatory behavior of buoyant plumes of helium and helium-air mixtures*. Physics of Fluids, 1996. **8**(11): p. 2974-2984.
44. Papanicolaou, P.N. and E.J. List, *Statistical and spectral properties of tracer concentration in round buoyant jets*. International journal of heat and mass transfer, 1987. **30**(10): p. 2059-2071.
45. Shabbir, A. and W.K. George, *Experiments on a round turbulent buoyant plume*. Journal of Fluid Mechanics, 1994. **275**: p. 1-32.

## **APPENDICES**



APPENDIX A FACILITY DRAWINGS



ITEM NO.	PART NUMBER	DESCRIPTION	QTY.
1	Mid Section Steel	Stainless Steel	1
2	Lower Plenum	Polycarbonate	1
3	Bottom Plate	Polycarbonate	1
4	Top Plate	Polycarbonate	1
5	Hemishpere	Polycarbonate	1
6	Steel Pipe	Stainless Steel	25
7	Cooling Jacket	Stainless Steel	1

PROPRIETARY AND CONFIDENTIAL

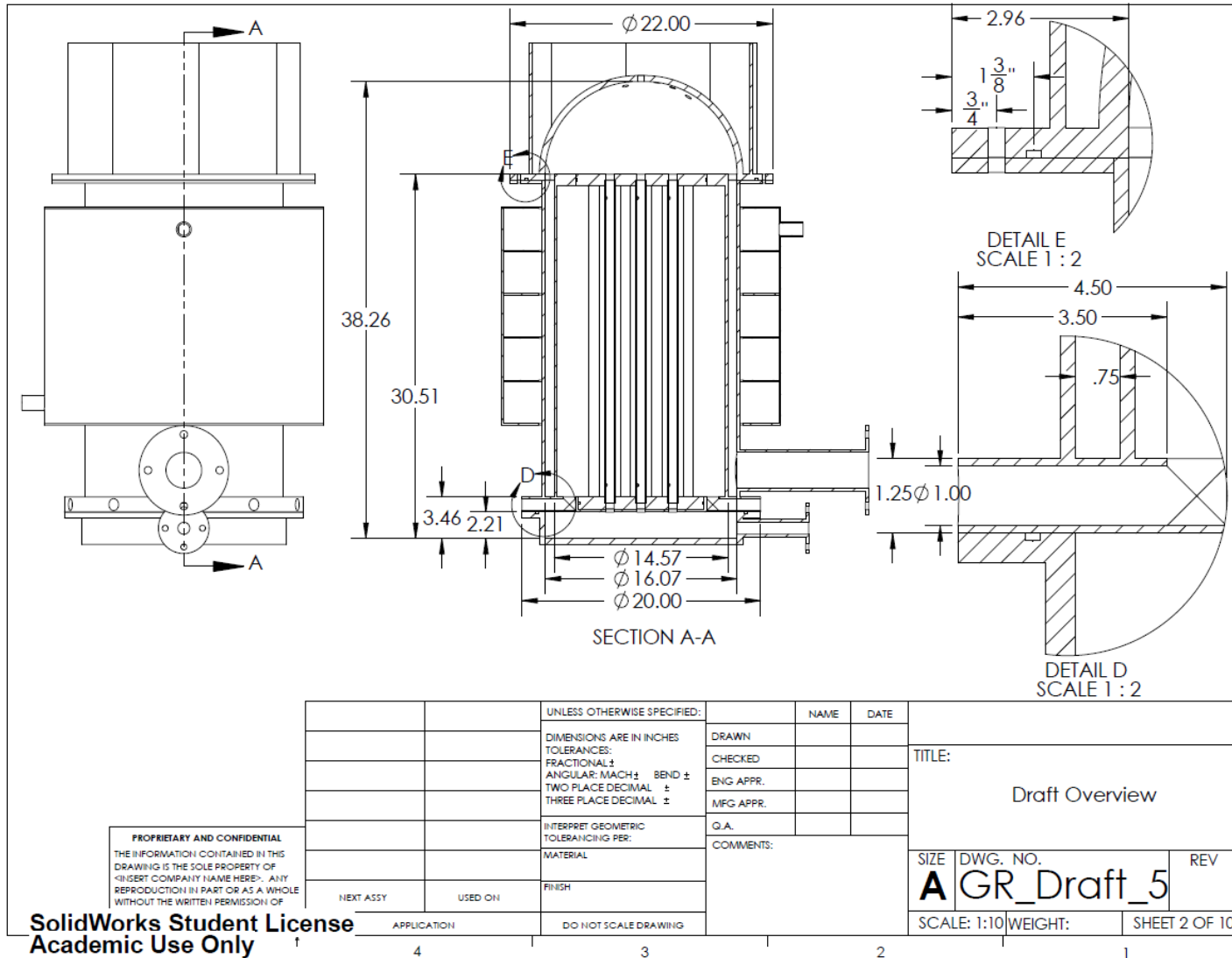
THE INFORMATION CONTAINED IN THIS DRAWING IS THE SOLE PROPERTY OF HUBERT COMPANY NAME HERE. ANY REPRODUCTION IN PART OR AS A WHOLE WITHOUT THE WRITTEN PERMISSION OF

SolidWorks Student License  
Academic Use Only

UNLESS OTHERWISE SPECIFIED:		NAME	DATE
DRAWN			
CHECKED			
ENG APPR.			
MFG APPR.			
Q.A.			
COMMENTS:			
MATERIAL			
FINISH			
DO NOT SCALE DRAWING			

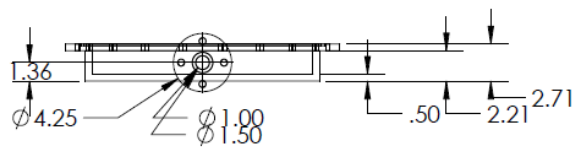
SIZE	DWG. NO.	REV
A	GR_Draft_5	

SCALE: 1:10	WEIGHT:	SHEET 1 OF 10

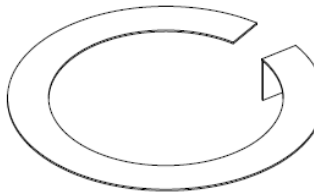
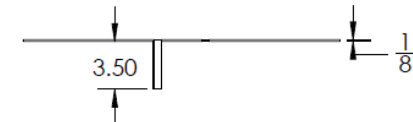
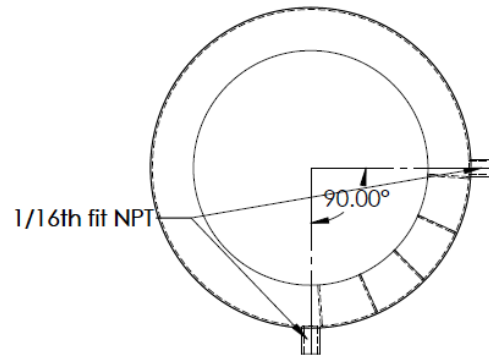
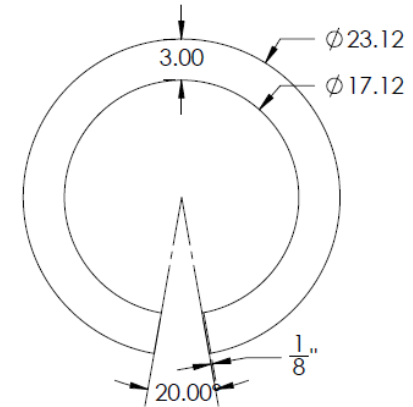
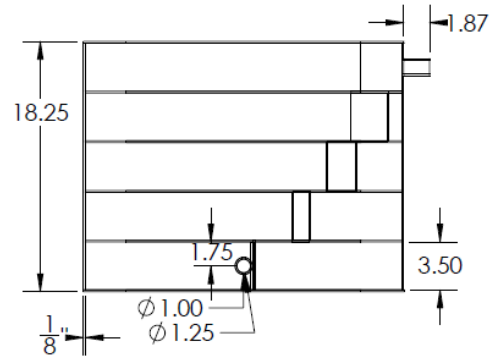
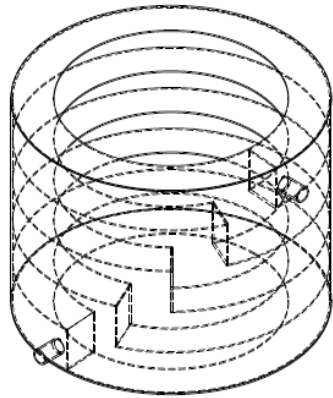


**SolidWorks Student License**  
**Academic Use Only**







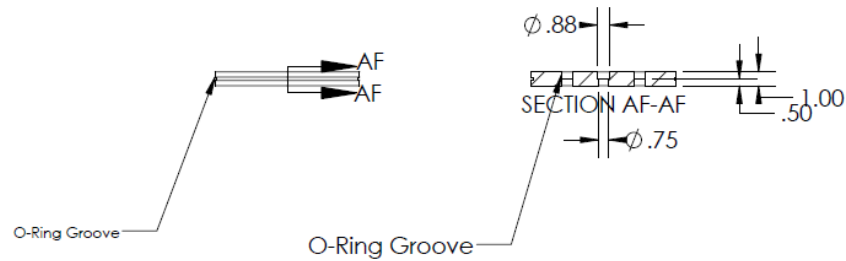
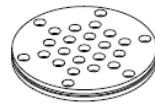
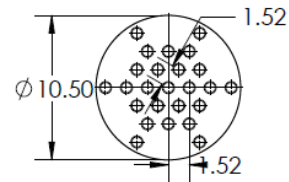


PROPRIETARY AND CONFIDENTIAL  
THE INFORMATION CONTAINED IN THIS  
DRAWING IS THE SOLE PROPERTY OF  
"INSERT COMPANY NAME HERE". ANY  
REPRODUCTION IN PART OR AS A WHOLE  
WITHOUT THE WRITTEN PERMISSION OF

**SolidWorks Student License**  
**Academic Use Only**

		UNLESS OTHERWISE SPECIFIED:		NAME	DATE		
		DIMENSIONS ARE IN INCHES		DRAWN			
		TOLERANCES:		CHECKED		TITLE:	
		FRACTIONAL: ±		ENG APPR.		Cooling Jacket	
		ANGULAR: MACH ± BEND ±		MFG APPR.			
		TWO PLACE DECIMAL ±		Q.A.			
		THREE PLACE DECIMAL ±		COMMENTS:			
		INTERPRET GEOMETRIC TOLERANCING PER:				SIZE DWG. NO. REV	
		MATERIAL				<b>A GR_Draft_5</b>	
NEXT ASSY		USED ON				SCALE: 1:10 WEIGHT: SHEET 6 OF 10	
APPLICATION		DO NOT SCALE DRAWING					

1 4 1 3 1 2 1

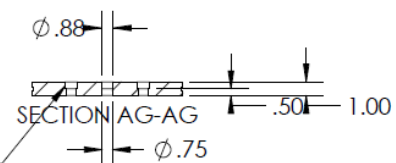
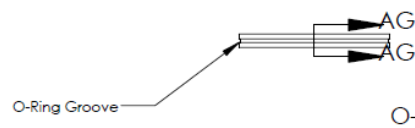
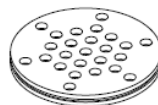
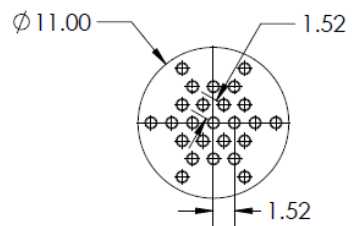


PROPRIETARY AND CONFIDENTIAL  
THE INFORMATION CONTAINED IN THIS  
DRAWING IS THE SOLE PROPERTY OF  
<INSERT COMPANY NAME HERE>. ANY  
REPRODUCTION IN PART OR AS A WHOLE  
WITHOUT THE WRITTEN PERMISSION OF

		UNLESS OTHERWISE SPECIFIED:		NAME	DATE	TITLE:  Bottom Plate	
		DIMENSIONS ARE IN INCHES	DRAWN				
		TOLERANCES:	CHECKED				
		FRACTIONAL ±	ENG APPR.				
		ANGULAR: MACH ± BEND ±	MFG APPR.				
		TWO PLACE DECIMAL ±	Q.A.			SIZE	DWG. NO.
		THREE PLACE DECIMAL ±	COMMENTS:			A GR_Draft_5	
		INTERPRET GEOMETRIC				REV	
		TOLERANCING PER:					
		MATERIAL				SCALE: 1:10	WEIGHT:
		FINISH				SHEET 7 OF 10	
NEXT ASSY	USED ON	APPLICATION					
		DO NOT SCALE DRAWING					

SolidWorks Student License  
Academic Use Only

4 3 2 1



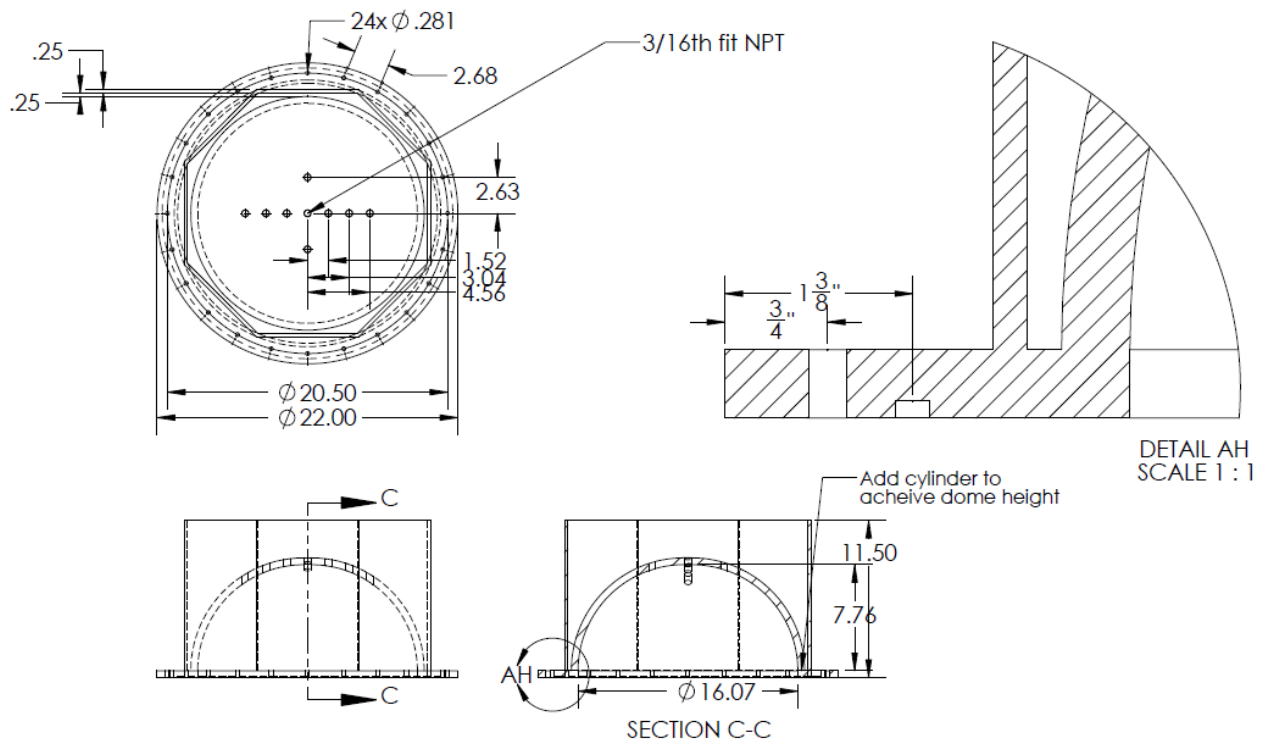
PROPRIETARY AND CONFIDENTIAL  
THE INFORMATION CONTAINED IN THIS  
DRAWING IS THE SOLE PROPERTY OF  
<INSERT COMPANY NAME HERE>. ANY  
REPRODUCTION IN PART OR AS A WHOLE  
WITHOUT THE WRITTEN PERMISSION OF

**SolidWorks Student License**  
**Academic Use Only**

		UNLESS OTHERWISE SPECIFIED:	NAME	DATE		
		DIMENSIONS ARE IN INCHES	DRAWN			
		TOLERANCES:	CHECKED		TITLE:  Top Plate	
		FRACTIONAL: ±	ENG APPR.			
		ANGULAR: MACH ± BEND ±	MFG APPR.			
		TWO PLACE DECIMAL ±	Q.A.			
		THREE PLACE DECIMAL ±	COMMENTS:			
		INTERPRET GEOMETRIC TOLERANCING PER:				
		MATERIAL				
		FINISH				
NEXT ASSY	USED ON					
APPLICATION		DO NOT SCALE DRAWING				
			SCALE: 1:10		WEIGHT:	SHEET 8 OF 10

SIZE DWG. NO. REV  
**A** GR\_Draft\_5

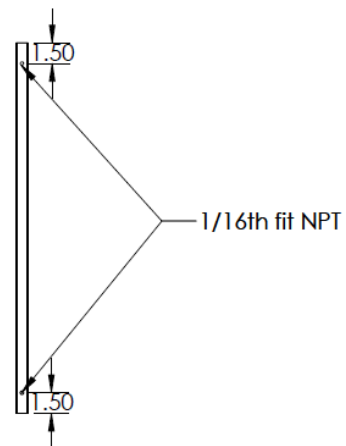
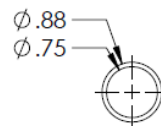




PROPRIETARY AND CONFIDENTIAL  
THE INFORMATION CONTAINED IN THIS  
DRAWING IS THE SOLE PROPERTY OF  
<INSERT COMPANY NAME HERE>. ANY  
REPRODUCTION IN PART OR AS A WHOLE  
WITHOUT THE WRITTEN PERMISSION OF

**SolidWorks Student License**  
**Academic Use Only**

		UNLESS OTHERWISE SPECIFIED:		NAME	DATE	TITLE:  Hemisphere		
		DIMENSIONS ARE IN INCHES	DRAWN					
		TOLERANCES:	CHECKED					
		FRACTIONAL: $\pm$	ENG APPR.					
		ANGULAR: MACH: $\pm$ BEND $\pm$	MFG APPR.					
		TWO PLACE DECIMAL $\pm$	Q.A.			SIZE DWG. NO. REV		
		THREE PLACE DECIMAL $\pm$						
		INTERPRET GEOMETRIC TOLERANCING PER:				SCALE: 1:10 WEIGHT: SHEET 9 OF 10		
		MATERIAL						
		FINISH				SCALE: 1:10 WEIGHT: SHEET 9 OF 10		
		DO NOT SCALE DRAWING						
		APPLICATION				SCALE: 1:10 WEIGHT: SHEET 9 OF 10		
		DO NOT SCALE DRAWING						
		DO NOT SCALE DRAWING				SCALE: 1:10 WEIGHT: SHEET 9 OF 10		
		DO NOT SCALE DRAWING						
		DO NOT SCALE DRAWING				SCALE: 1:10 WEIGHT: SHEET 9 OF 10		
		DO NOT SCALE DRAWING						
		DO NOT SCALE DRAWING				SCALE: 1:10 WEIGHT: SHEET 9 OF 10		
		DO NOT SCALE DRAWING						
		DO NOT SCALE DRAWING				SCALE: 1:10 WEIGHT: SHEET 9 OF 10		
		DO NOT SCALE DRAWING						
		DO NOT SCALE DRAWING				SCALE: 1:10 WEIGHT: SHEET 9 OF 10		
		DO NOT SCALE DRAWING						
		DO NOT SCALE DRAWING				SCALE: 1:10 WEIGHT: SHEET 9 OF 10		
		DO NOT SCALE DRAWING						
		DO NOT SCALE DRAWING				SCALE: 1:10 WEIGHT: SHEET 9 OF 10		
		DO NOT SCALE DRAWING						
		DO NOT SCALE DRAWING				SCALE: 1:10 WEIGHT: SHEET 9 OF 10		
		DO NOT SCALE DRAWING						
		DO NOT SCALE DRAWING				SCALE: 1:10 WEIGHT: SHEET 9 OF 10		
		DO NOT SCALE DRAWING						
		DO NOT SCALE DRAWING				SCALE: 1:10 WEIGHT: SHEET 9 OF 10		
		DO NOT SCALE DRAWING						
		DO NOT SCALE DRAWING				SCALE: 1:10 WEIGHT: SHEET 9 OF 10		
		DO NOT SCALE DRAWING						
		DO NOT SCALE DRAWING				SCALE: 1:10 WEIGHT: SHEET 9 OF 10		
		DO NOT SCALE DRAWING						
		DO NOT SCALE DRAWING				SCALE: 1:10 WEIGHT: SHEET 9 OF 10		
		DO NOT SCALE DRAWING						
		DO NOT SCALE DRAWING				SCALE: 1:10 WEIGHT: SHEET 9 OF 10		
		DO NOT SCALE DRAWING						
		DO NOT SCALE DRAWING				SCALE: 1:10 WEIGHT: SHEET 9 OF 10		
		DO NOT SCALE DRAWING						
		DO NOT SCALE DRAWING				SCALE: 1:10 WEIGHT: SHEET 9 OF 10		
		DO NOT SCALE DRAWING						
		DO NOT SCALE DRAWING				SCALE: 1:10 WEIGHT: SHEET 9 OF 10		
		DO NOT SCALE DRAWING						
		DO NOT SCALE DRAWING				SCALE: 1:10 WEIGHT: SHEET 9 OF 10		
		DO NOT SCALE DRAWING						
		DO NOT SCALE DRAWING				SCALE: 1:10 WEIGHT: SHEET 9 OF 10		
		DO NOT SCALE DRAWING						
		DO NOT SCALE DRAWING				SCALE: 1:10 WEIGHT: SHEET 9 OF 10		
		DO NOT SCALE DRAWING						
		DO NOT SCALE DRAWING				SCALE: 1:10 WEIGHT: SHEET 9 OF 10		
		DO NOT SCALE DRAWING						
		DO NOT SCALE DRAWING				SCALE: 1:10 WEIGHT: SHEET 9 OF 10		
		DO NOT SCALE DRAWING						
		DO NOT SCALE DRAWING				SCALE: 1:10 WEIGHT: SHEET 9 OF 10		
		DO NOT SCALE DRAWING						
		DO NOT SCALE DRAWING				SCALE: 1:10 WEIGHT: SHEET 9 OF 10		
		DO NOT SCALE DRAWING						
		DO NOT SCALE DRAWING				SCALE: 1:10 WEIGHT: SHEET 9 OF 10		
		DO NOT SCALE DRAWING						
		DO NOT SCALE DRAWING				SCALE: 1:10 WEIGHT: SHEET 9 OF 10		
		DO NOT SCALE DRAWING						
		DO NOT SCALE DRAWING				SCALE: 1:10 WEIGHT: SHEET 9 OF 10		
		DO NOT SCALE DRAWING						
		DO NOT SCALE DRAWING				SCALE: 1:10 WEIGHT: SHEET 9 OF 10		
		DO NOT SCALE DRAWING						
		DO NOT SCALE DRAWING				SCALE: 1:10 WEIGHT: SHEET 9 OF 10		
		DO NOT SCALE DRAWING						
		DO NOT SCALE DRAWING				SCALE: 1:10 WEIGHT: SHEET 9 OF 10		
		DO NOT SCALE DRAWING						
		DO NOT SCALE DRAWING				SCALE: 1:10 WEIGHT: SHEET 9 OF 10		
		DO NOT SCALE DRAWING						
		DO NOT SCALE DRAWING				SCALE: 1:10 WEIGHT: SHEET 9 OF 10		
		DO NOT SCALE DRAWING						
		DO NOT SCALE DRAWING				SCALE: 1:10 WEIGHT: SHEET 9 OF 10		
		DO NOT SCALE DRAWING						
		DO NOT SCALE DRAWING				SCALE: 1:10 WEIGHT: SHEET 9 OF 10		
		DO NOT SCALE DRAWING						
		DO NOT SCALE DRAWING				SCALE: 1:10 WEIGHT: SHEET 9 OF 10		
		DO NOT SCALE DRAWING						
		DO NOT SCALE DRAWING				SCALE: 1:10 WEIGHT: SHEET 9 OF 10		
		DO NOT SCALE DRAWING						
		DO NOT SCALE DRAWING				SCALE: 1:10 WEIGHT: SHEET 9 OF 10		
		DO NOT SCALE DRAWING						
		DO NOT SCALE DRAWING				SCALE: 1:10 WEIGHT: SHEET 9 OF 10		
		DO NOT SCALE DRAWING						
		DO NOT SCALE DRAWING				SCALE: 1:10 WEIGHT: SHEET 9 OF 10		
		DO NOT SCALE DRAWING						
		DO NOT SCALE DRAWING				SCALE: 1:10 WEIGHT: SHEET 9 OF 10		
		DO NOT SCALE DRAWING						
		DO NOT SCALE DRAWING				SCALE: 1:10 WEIGHT: SHEET 9 OF 10		
		DO NOT SCALE DRAWING						
		DO NOT SCALE DRAWING				SCALE: 1:10 WEIGHT: SHEET 9 OF 10		
		DO NOT SCALE DRAWING						
		DO NOT SCALE DRAWING				SCALE: 1:10 WEIGHT: SHEET 9 OF 10		
		DO NOT SCALE DRAWING						
		DO NOT SCALE DRAWING				SCALE: 1:10 WEIGHT: SHEET 9 OF 10		
		DO NOT SCALE DRAWING						
		DO NOT SCALE DRAWING				SCALE: 1:10 WEIGHT: SHEET 9 OF 10		
		DO NOT SCALE DRAWING						
		DO NOT SCALE DRAWING				SCALE: 1:10 WEIGHT: SHEET 9 OF 10		
		DO NOT SCALE DRAWING						
		DO NOT SCALE DRAWING				SCALE: 1:10 WEIGHT: SHEET 9 OF 10		
		DO NOT SCALE DRAWING						
		DO NOT SCALE DRAWING				SCALE: 1:10 WEIGHT: SHEET 9 OF 10		
		DO NOT SCALE DRAWING						
		DO NOT SCALE DRAWING				SCALE: 1:10 WEIGHT: SHEET 9 OF 10		
		DO NOT SCALE DRAWING						
		DO NOT SCALE DRAWING				SCALE: 1:10 WEIGHT: SHEET 9 OF 10		
		DO NOT SCALE DRAWING						
		DO NOT SCALE DRAWING				SCALE: 1:10 WEIGHT: SHEET 9 OF 10		
		DO NOT SCALE DRAWING						
		DO NOT SCALE DRAWING				SCALE: 1:10 WEIGHT: SHEET 9 OF 10		
		DO NOT SCALE DRAWING						
		DO NOT SCALE DRAWING				SCALE: 1:10 WEIGHT: SHEET 9 OF 10		
		DO NOT SCALE DRAWING						



PROPRIETARY AND CONFIDENTIAL  
THE INFORMATION CONTAINED IN THIS  
DRAWING IS THE SOLE PROPERTY OF  
<INSERT COMPANY NAME HERE>. ANY  
REPRODUCTION IN PART OR AS A WHOLE  
WITHOUT THE WRITTEN PERMISSION OF

**SolidWorks Student License**  
**Academic Use Only**

		UNLESS OTHERWISE SPECIFIED:		NAME	DATE			
		DIMENSIONS ARE IN INCHES	DRAWN			TITLE:  Steel Piping		
		TOLERANCES:	CHECKED					
		FRACTIONAL: ±	ENG APPR.					
		ANGULAR: MACH: ± BEND ±	MFG APPR.					
		TWO PLACE DECIMAL ±	Q.A.			SIZE	DWG. NO.	
		THREE PLACE DECIMAL ±	COMMENTS:			<b>A</b>	GR_Draft_5	
		INTERPRET GEOMETRIC TOLERANCING PER:				SCALE: 1:10	WEIGHT:	REV
		MATERIAL				SHEET 10 OF 10		
NEXT ASSY	USED ON	FINISH						
APPLICATION		DO NOT SCALE DRAWING						

# **ATTACHMENT 1**

## **EXPERIMENTAL DESIGN AND FLOW VISUALIZATION FOR THE UPPER PLENUM OF A VERY HIGH TEMPERATURE GAS COOLED FOR COMPUTER FLUID DYNAMICS VALIDATION**

A Thesis

by

KYLE L. MCVAY

Submitted to the Office of Graduate and Professional Studies of  
Texas A&M University

in partial fulfillment of the requirements for the degree of

**MASTER OF SCIENCE**

Chair of Committee, Hassan, Yassin

Co- Chair, Anand, Nagamangala

Committee Members, Chen, Hamn Lau, Sai

Head of Department, Polycarpou, Andreas

August 2014

Major Subject: Mechanical Engineering

Copyright 2014 Texas A&M

## **ABSTRACT**

The Very High Temperature Reactor (VHTR) is a Generation IV nuclear reactor that is currently under design. It modifies the current high temperature gas reactor (HTGR) design to have a 1000 °C coolant outlet. This increases fuel efficiency and allows for other industrial applications. During the design process several studies are performed to develop safety codes for the reactor. One major accident of interest is the Pressurized Conduction Cooldown (PCC) scenario. The PCC scenario involves loss of forced coolant to the core but the loop stays pressurized. This results in a large buoyancy force that through natural convection reverses the flow of the core coolant loop to circulate into the upper plenum of the VHTR. Computer codes may be developed to simulate the phenomenon that occurs in a PCC scenario, but benchmark data is needed to validate the simulations. There are currently no experimental models to provide benchmark data for the PCC scenario. This study will cover the design, construction, and testing of a 1/16<sup>th</sup> scaled model of a VHTR that uses Particle Image Velocimetry (PIV) for flow visualization in the upper plenum. Three tests were run for a partially heated core at statistically steady state, and PIV was used to generate the velocity field of three naturally convective adjacent jets. After performing a sensitivity analysis the flow rate of a single pipe was extracted from the PIV flow field, and compared with an ultrasonic flowmeter and calculated flow rate. All the values lied within the calculated error ranges, validating the test results.

## **Acknowledgements**

First I would like to thank the Department of Energy for funding this project. I am honored for the opportunity to work on such exciting and stimulating research. I'd also like to thank Dr. Richard Schultz and everyone else at Idaho National Laboratories for their research and work in organizing this project.

I would like to thank Dr. Yassin Hassan and Dr. N.K. Anand who were great advisors despite their busy schedules. Researching under such experienced and respected advisors has been a gift, and I am grateful for the guidance as well as the freedom given while performing my research.

My sincere thanks go to my colleague Saya Lee. His experience and knowledge was crucial for this study. He had an answer to my every question and problem, and was usually correct. I'd also like to thank Robert Park my research partner and friend, who acted as my counterbalance and was enjoyable to work with. Likewise I'd like to thank my labmate Pratanu Roy, who I could always count on for sensible professional advice.

Finally I would like to thank my parents who raised me with the morals to become who I am today, and who have supported me throughout my academic career. I wouldn't be an engineer today without you.

## Table of Contents

ABSTRACT .....	II
ACKNOWLEDGEMENTS .....	III
TABLE OF CONTENTS .....	IV
TABLE OF FIGURES .....	V
1 INTRODUCTION .....	1
1.1 Project Background .....	2
1.2 Research Objectives .....	5
1.3 Outline .....	6
2 LITERATURE REVIEW .....	7
2.1 Previous Studies - Simulations.....	7
2.2 Previous Studies – Scaling and Modeling.....	12
2.3 Previous Studies – Particle Image Velocimetry .....	16
3 PROJECT DESIGN .....	23
3.1 Solidworks Design Phase .....	23
3.2 Project Assembly.....	29
3.3 Data Acquisition.....	38
4 TESTS AND RESULTS .....	44
4.1 Testing .....	44
4.2 Analyzing .....	46
4.3 Results .....	49
4.4 Computer Fluid Dynamics Modeling.....	64
5 CONCLUSION AND FUTURE WORK .....	70
5.1 Conclusion.....	70
5.2 Future Work .....	72
REFERENCES.....	74
Appendix A.....	vii

## Table of Figures

Figure 1-1: VHTR under normal operation.....	3
Figure 1-2: Air Ingress Causing DCC Scenario for a VHTR .....	5
Figure 2-1: VHTR velocity profile following a PCC accident scenario .....	8
Figure 2-2: VHTR Temperature profile following a PCC accident scenario .....	8
Figure 2-3: Velocity contour at top of the VHTR core 100 seconds after PCC scenario	10
Figure 2-4: Streamline plot of the upper plenum 100 seconds after the PCC scenario ...	10
Figure 2-5: Oregon State University's high temperature test facility .....	16
Figure 2-6: PIV Schematic .....	17
Figure 2-7: Cross Correlation field .....	18
Figure 3-1: Initial Design Geometry .....	24
Figure 3-2: Pipe Layout.....	25
Figure 3-3: Cooling Jacket Design.....	25
Figure 3-4: Exploded cross section .....	27
Figure 3-5: Cross section after assembly .....	27
Figure 3-6: Experimental scaffolding .....	30
Figure 3-7: Piping, heating tape, and thermocouples.....	31
Figure 3-8: Lower plenum and core containment .....	31
Figure 3-9: Reservoir tank.....	31
Figure 3-10: Insulated core .....	32
Figure 3-11: Core and containment.....	32
Figure 3-12: Top plate flush with containment.....	33
Figure 3-13: Outer containment being lowered .....	33

Figure 3-14: Assembled Facility .....	34
Figure 3-15: Top view of upper plenum .....	34
Figure 3-16: Sealing the heating tapes with silicon tubing and adhesive .....	36
Figure 3-17: Thermocouple with tubing, epoxy, and ferrules.....	37
Figure 3-18: Core top view after reassembly .....	38
Figure 3-19: Cross section for data acquisition.....	40
Figure 3-20: Calibration test for flowmeter .....	41
Figure 3-21: Calibration curve for flowmeter .....	41
Figure 3-22: Glass bead particles vs Fluorescent particles .....	42
Figure 4-1: Pipe layout with closed pipes .....	45
Figure 4-2: Analysis region.....	45
Figure 4-3: PIVlab vector field output .....	48
Figure 4-4: Velocity magnitude for set 2 .....	49
Figure 4-5: Y-velocity contour for set 2.....	50
Figure 4-6: Vorticity for single image pair .....	51
Figure 4-7: Vorticity contour for set 3 .....	52
Figure 4-8: Percent error of Y- velocity field for different numbers of image pairs .....	54
Figure 4-9: Line extraction locations for sensitivity analysis .....	55
Figure 4-10: Sensitivity analysis for set 2 - 0.1m line.....	56
Figure 4-11: Sensitivity analysis for set 2 - 0.06 m line .....	57
Figure 4-12: Sensitivity Analysis for set 2 - 0.02 m line .....	59
Figure 4-13: Repeatability.....	60
Figure 4-14: Standard deviation of turbulent velocity fluctuations for set 2 at Y=0.1m. 61	
Figure 4-15: Flow rates for single pipe with different methods.....	63



Figure 4-16: Test facility CFD model .....	65
Figure 4-17: Velocity field of gas reactor fluid region .....	66
Figure 4-18: Non-symmetric cross section of upper plem .....	67
Figure 4-19: Symmetric cross section of upper plenum .....	68
Figure A-1: Sensitivity Analysis for set 1 - 0.1m line extraction.....	1
Figure A-2: Sensitivity analysis for set 2 – 0.1 m line extraction .....	2
Figure A-3: Sensitivity analysis for set 3 – 0.1 m line extraction .....	3
Figure A-4: Sensitivity analysis for set 1 – 0.06 m line extraction .....	4
Figure A-5: Sensitivity analysis for set 2 – 0.06 m line extraction .....	5
Figure A-6: Sensitivity analysis for set 3 – 0.06 m line extraction .....	6
Figure A-7: Sensitivity analysis for set 1 – 0.02 m line extraction .....	7
Figure A-8: Sensitivity analysis for set 2 – 0.02 m line extraction .....	8
Figure A-9: Sensitivity analysis for set 3 – 0.02 m line extraction .....	9

## **1 INTRODUCTION**

The world is ever growing, and the energy demands grow with it. The United States energy consumption from just 2010 to 2013 has grown from 74.769 to 81.664 Quadrillion Btu, a 9% increase and 78% of the energy consumed in 2013 were fossil fuels[1]. As the fossil fuels grow scarcer and the demand for alternative energy rises the nuclear industry will continue to develop to meet this demand and with it the safety codes governing them. Intensive safety analysis has been performed for currently operating reactors, and several safety systems are employed to ensure safe operation and that the correct procedures are taken in case of emergency conditions to minimize further damage. Older reactor models safety systems rely on pumps, electricity, and human interaction all of which may fail resulting in serious damages to human health, the reputation of the nuclear industry, and monetary loss. In light of this the current Gen III reactors, such as the AP1000 developed by Westinghouse, employ passive safety systems. Instead of using active components, passive safety systems use natural forces such as gravity, pressure, and compressed gases to keep the core and containment from overheating and melting the fuel for an extended period of time[2]. As the industry advances into the next generation of reactors, the safety systems must evolve with it.

## 1.1 Project Background

The Very-high-temperature-reactor (VHTR) is a prominent Generation IV nuclear reactor design. The VHTR loosely includes any reactor design with a coolant outlet temperature about 1000 °C or above[3]. However it is typically used when discussing the evolutionary development of the high-temperature gas-cooled reactors (HTGR). The HTGR is largely defined by its fuel design. The fuel is comprised of small particles that are coated with porous graphite, layers of pyrolytic carbon, silicon, and carbide. These particles are then loaded into several spheres and are grouped in the core, or the fuel is loaded into thin rods and arranged in a hexagonal pattern following the prismatic design[4]. The fuel particles can withstand very high temperatures and will not fail below 1600 °C permitting the design of the HTGR. The current HTGRs in operation operate with an outlet of 850 °C, where employing the VHTR technology design would increase the outlet temperature to 1000 °C or greater.

Because of the high outlet temperature the VHTR enables it for other applications besides energy production. One application is the mass production of hydrogen. As efficient fuel cells are developed and the demand for hydrogen grows a new market based on hydrogen power is introduced. Currently 95% of the hydrogen being produced uses valuable natural gases, which makes it economically unusable for consumer use[5]. A more environmentally friendly and economically viable production of hydrogen would use a nuclear energy system to mass produce the hydrogen. The hot steam produced by nuclear reactors, particularly the VHTR, is optimal for electrolysis in hydrogen production. Said hydrogen could be used to replace fossil fuels in multiple applications

such as automobiles[6]. Another application of the VHTR is heat production to be used in industrial applications such as coal gasification or petrochemical operations. The VHTR is designed to have high fuel efficiency and maintain the safety characteristics of the modular high temperature gas-cooled reactors. Studies by Idaho National Engineering and Environmental Laboratory (INEEL) on a pebble bed and prismatic design for the HTGR shows that both of their designs meet the three basic requirements set for the Next Generation Nuclear Plant (NGNP): a coolant outlet of 1000 °C, passive safety systems, and a total power output that meets the expected output for commercial HTGR, making the VHTR design the leading candidate for the NGNP and a prominent focus for studies[5].

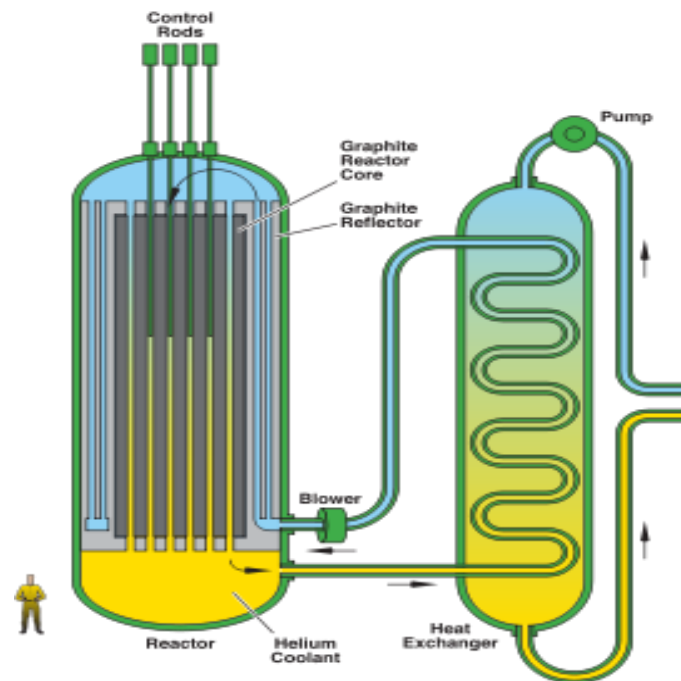


Figure 1-1:VHTR under normal operation

Since the VHTR is still in design phase, multiple studies are being performed that can be used in developing the safety codes. Multiple accident scenarios as well as normal operation are of interest. Two primary accident scenarios for the VHTR are the Pressurized Conduction Cooldown (PCC) and the Depressurized Conduction Cooldown (DCC). Under normal operation a blower is used to pump the coolant up between the reflector and the core, where it then impinges on the upper plenum and goes down through the core as seen in Figure 1-1, resulting in forced convection for core cooling[7]. A PCC scenario occurs most commonly during a loss of power scenario. The blower fails and the forced convection fails with it. Because the loop is still pressurized the gas density remains high which leads to a large buoyancy force. Over time this force reverses circulation through the core, causing the coolant, normally helium, to rise from the lower plenum up through the core, into the upper plenum, and down between the reflector and the core. The DCC scenario occurs when the main pressure loop has been breached. Hot air is vented out and cold air ingress floods the containment. Because the containment is depressurized the buoyancy force is insufficient to counteract the inertial forces. This causes the cold air to pool at the bottom of the containment where it eventually diffuses through the hot coolant, usually helium. This process can be seen in Figure 1-2[8]. This is much slower than the PCC scenario's buoyancy driven, making the DCC scenario more critical as the core will reach higher temperatures.

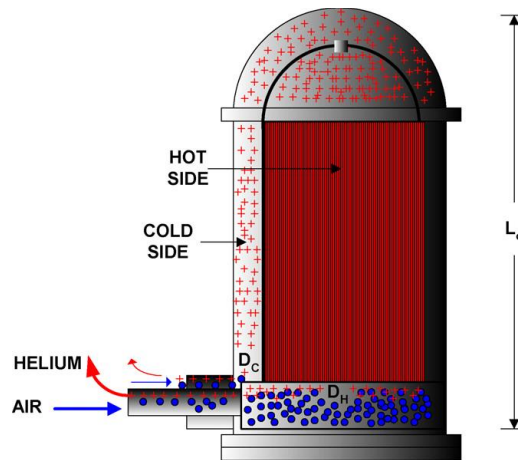


Figure 1-2: Air Ingress Causing DCC Scenario for a VHTR

## 1.2 Research Objectives

The primary focus of this study is the design, construction, and testing of a scaled ( $1/16^{\text{th}}$ ) experimental facility that models a VHTR. The model must be able to extract data relating to flow visualization and other thermal hydraulic phenomena in the upper plenum and be used to validate Computer Fluid Dynamics (CFD) codes.

The design of this facility accounted for several parameters which include: the scaled geometry from INL, fabrication process limitations, can supply sufficient heat to the modeled core for testing, a heat sink sufficient to remove the heat input, and a system that allows for sufficient data acquisition. Once this facility was designed and constructed, the testing may begin.

The experimental facility uses Particle Image Velocimetry (PIV) to measure the velocity field of a planar cross section in the upper plenum of the scaled model. This study obtains particle images that are processed using PIV techniques, and the results are validated. First a sensitivity analysis is performed to determine the sufficient

number of images to correctly represent the flow field. Then multiple tests are compared to each other for repeatability. Finally the PIV results are validated by comparing them with an ultrasonic flowmeter and calculated flowrates.

### **1.3 Outline**

This chapter describes the Background and Validation for this study. It largely focuses on the design and future applications of the VHTR, as well as the accident scenarios of interest. It also covers the objectives for this study.

Chapter 2 will provide information performed in previous studies performed related to the VHTR. Additionally it will go over the scaling and modeling performed in other studies that relate to the test facility.

Chapter 3 will explain the procedure in designing the experimental test facility. It will also cover the assembly process after the parts are finished machining and problems encountered, as well as the data acquisition layout and parts selection.

Chapter 4 will cover the testing procedure, data analysis, and the results. Additionally an example computer fluid dynamics simulation is discussed.

Chapter 5 has the conclusion which provides a summary and what has been gained from the study, as well as future possible work that can be accomplished with the test facility.

## **2 LITERATURE REVIEW**

### **2.1 Previous Studies - Simulations**

A transient numerical model was used by Haque to simulate the flow through the core after the accident occurs[9]. The temperature profile can be seen below in Figure 2-1 and the temperature profile in Figure 2-2. Their thermal hydraulic code THERMIX has been verified with experimental data[10]. Initially the hottest part of the core is in the lower half, but as the buoyancy forces overpower the inertial forces, the flow reverses and the temperature profile shifts towards the top of the core. This study also evaluated a DCC scenario. Without the natural circulation the core reached 1587 °C, near the failing point of the fuel. Because the DCC scenario is more severe there has been more research on the behavior of the system following depressurization.



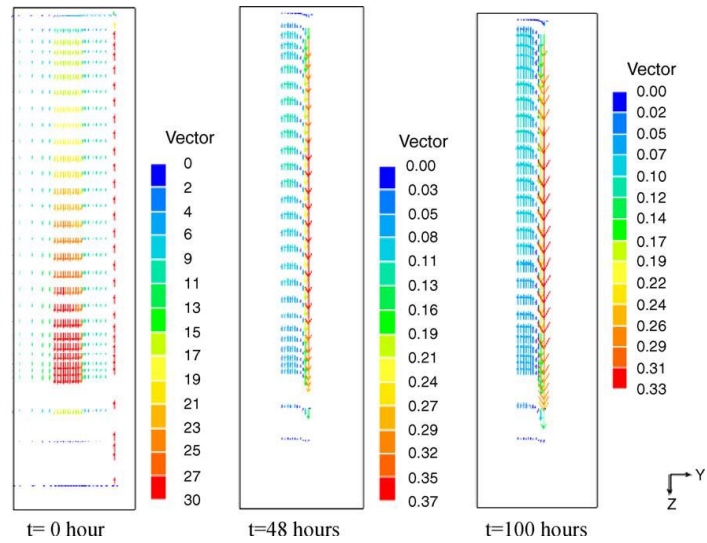


Figure 2-1: VHTR velocity profile following a PCC accident scenario

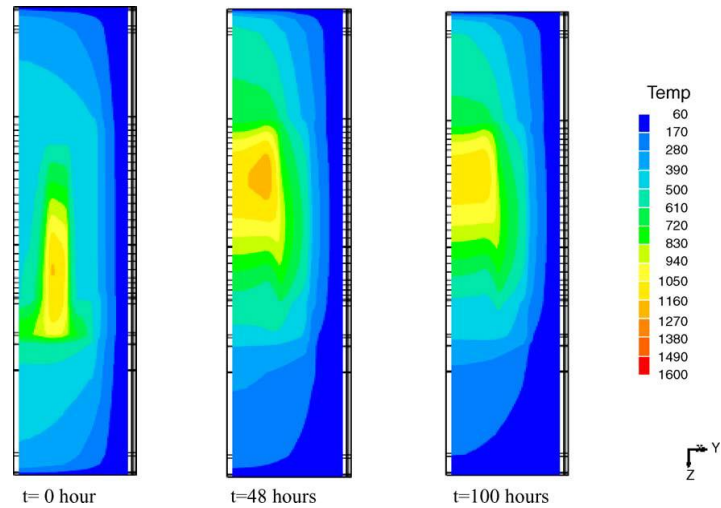
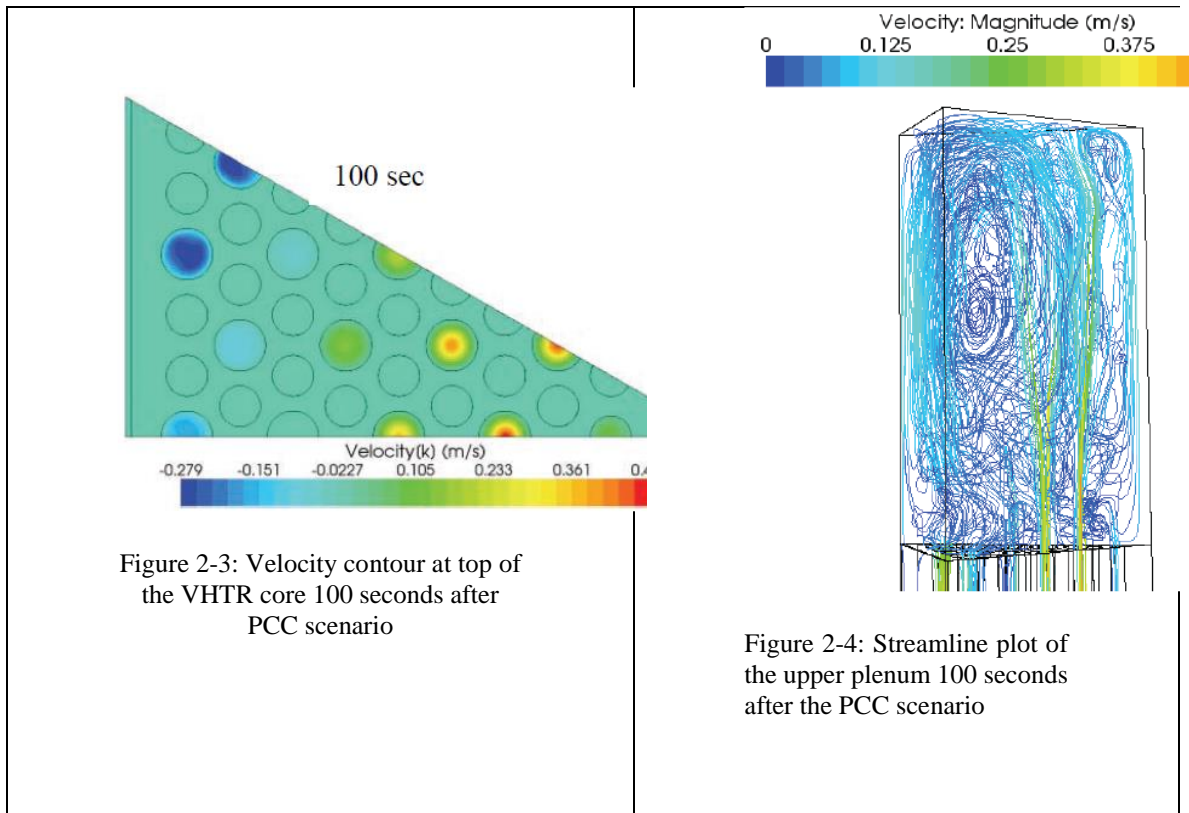


Figure 2-2: VHTR Temperature profile following a PCC accident scenario

Tung and Johnson working with INL published a study in 2011 of CFD analysis for a 1/12<sup>th</sup> sector of a heated column of prismatic blocks that covers the

heated portion of the core of a prismatic VHTR[11]. Using the steady state operating conditions as the initial conditions, Star-ccm+ was used for a transient analysis following a PCC scenario. Their mesh used 7.6 million cells for the core, and a total of 11.1 million cells with the upper and lower plenum. Figure 2-3 shows the velocity contour at the top of the core. Buoyancy forces drive the flow up through the center of the core as its hotter there, and then because there is no outlet for their model it goes down the coolant channels at the edge. They claim that though in reality there is an outlet, the flow resistance to go to the outlet and down to the lower plenum is higher than the nearby coolant channels, so the down-flow should occur in exterior coolant channels. Figure 2-4 shows the flow streamlines in the upper plenum. The flow impinges onto the top of the upper plenum, which is flat and doesn't represent the geometry of the actual VHTR.



The French CEA released a study in 2002 about the thermal fluctuations in the lower plenum of a HTGR[12]. There are internal structures below the reactor that are important in supporting the core. Part of this structure is subjected to 850<sup>0</sup>C helium near the outlet, but also subjected on its other side to 450<sup>0</sup>C helium coming from the cold duct resulting in a sharp temperature gradient. Because of this their study focused on estimating the thermal stresses induced by the temperature gradient in the different support structures, which requires thermal and flow analysis in the lower plenum. They used the CATHARE code to perform global simulations which gave accurate boundary conditions[13]. These

conditions were then used for transient CFD simulations for 4.5 seconds. Their results analyzed the oscillating characteristics and the mixing of flows that occurs.

Idaho National Laboratories (INL) has performed significant analysis for normal operations, DCC scenario, and partial loss of active coolant. INL has worked with the Korea Advanced Institute of Technology (KAIST), Seoul National University (SNU), and the University of Michigan (UM) to develop safety codes for the VHTR [14]. In March 2006 INL submitted a report to the Department of Energy (DOE) their study which focused on a loss-of-coolant accident (LOCA) resulting in a DCC scenario. LOCA accidents can lead to significant fuel damage of a VHTR. The tests modeled a new reactor core cooling system (RCCS) that used water instead of air as the coolant, and removed complex structures of other currently used water cooled RCCS models. Three scenarios were tested: normal operation, partial active cooling failure, and a loss of coolant (LOCA) scenario. To model this, an intensive CFD code was developed by KAIST to model the thermo-fluid phenomena that occurs in the multi-component mixture when an air and water ingress accident occurs in a VHTR. Two experiments were used to validate the code. A water pool reactor core cooling system (RCCS) was built at SNU, and an inverse U-tube experiment that predicted the thermo-fluid and chemical reaction behavior of a multi-component mixture. The codes were developed, refined, and validated with experimental measurements to be used in calculations for safety issues during a DCC accident in a VHTR, normal operations, and partial failure of active coolant.

## 2.2 Previous Studies – Scaling and Modeling

In September 2006 INL submitted a report to the Department Of Energy (DOE) for the experimental modeling of a VHTR during normal operation and a PCC scenario[15]. A lower plenum model would be used to model hot streaking and thermal striping phenomena that occurs during normal operation. Another model would be needed to model the upper plenum during a PCC scenario to monitor the flow phenomena in the upper plenum of the VHTR. INL covered mainly the conceptual design and scaling of possible models. The conceptual design included inducing channel flow with pumps or natural circulation, possible heat sink designs, the fluids to use, and modeling designs that allowed for light sheets to illuminate the upper plenum for particle imaging. The scaling analysis approach was to match the Richardson number, the ratio of the buoyancy force and inertial force, and the Reynolds number, the ratio of inertial to viscous forces, of the experimental model to the VHTR prototype for normal operation of a PCC scenario. The Boussinesq Approximation was used to determine the density change as a function of temperature. The Boussinesq approximates the density change as,

$$\rho = \rho_0 + \Delta\rho \quad (2.1)$$

Using this Navier-Stokes equation becomes [16],

$$\frac{D\bar{V}}{Dt} = -\frac{\nabla P}{\rho} + \nu \nabla^2 \bar{V} + \frac{\Delta\rho}{\rho} g \quad (2.2)$$

In this  $\bar{V}$  is the velocity vector,  $t$  is time,  $P$  is pressure,  $\nu$  is kinematic viscosity, and  $\bar{g}$  is the gravitational acceleration. Measuring the pressure difference and using it analytically is problematic. To fix this it can be represented as a function of the temperature difference,

$$\Delta\rho = -\alpha\rho_0\Delta T \quad (2.3)$$

Where  $\alpha$  is the thermal expansion coefficient. As discussed before the Richardson number is the focus of the scaling analysis. From the Navier-Stokes equation the inertial and buoyancy forces are used to represent the Richardson as a function of either the density or temperature gradient. The Richardson number and the ratio for the model (m) and the prototype (p) are shown below.

$$Ri = \frac{g(\Delta T / T)D}{V^2} \quad (2.4)$$

$$\frac{Ri_m}{Ri_p} = \frac{\left(\frac{\Delta\rho}{\rho}\right)_m V_p^2 D_m}{\left(\frac{\Delta\rho}{\rho}\right)_p V_m^2 D_p} \quad (2.5)$$

And if the Richardson number matched for both the model and the prototype, that is  $Ri_m/Ri_p = 1$ , then the Reynolds number ratio may be expressed as,

$$\frac{Re_m}{Re_p} = \frac{V_m D_m \nu_p}{V_p D_p \nu_m} = \left[ \frac{\left(\frac{\Delta\rho}{\rho}\right)_m}{\left(\frac{\Delta\rho}{\rho}\right)_p} \right]^{1/2} \left[ \frac{D_m}{D_p} \right]^{3/2} \frac{\nu_p}{\nu_m} \quad (2.6)$$

The pressure and temperature difference for the experimental model will be significantly less than that of the prototype as the model can only realistically operate at much lower temperatures and a pressure near one atmosphere, so the ratios would be off. However if water was used in the experimental model then this problem can be compensated for by the differences in density and viscosity between water and helium. Additionally the experimental model cannot model the Reynolds number in the core. This is due to the decrease in the number of channels from about 11,000 total channels to 67 channels for a 1/4<sup>th</sup> scaled model. Once the flow enters the upper plenum the model may be representative of the Reynolds number. After this other characteristics of the model such as the adiabatic heat transfer and relating the model jet flow and the prototype jet flow were considered for the scaling analysis of the model.

After the scaling analysis was done the INL began the experimental modeling design [17]. Different experimental modeling techniques were considered for modeling a VHTR under normal operations or PCC conditions. The designs covered an experimental apparatus that could model three dimensional laminar natural circulation in the upper and lower plenums. One topic was the method to model the heated coolant. One method was heating the fluid in the core channels to induce natural circulation, another by simulating the channel flows using pumps of pre-heated fluid. For the upper plenum one could use a complete, one-half, or one-quarter model of the geometry of the prototype. The instrumentation was also discussed. The main data acquisition would be performed

by PIV and Planar Laser Induced Fluorescence (PLIF) which can measure the temperature field of a planar cross section.

Oregon State University has been tasked with creating a High Temperature Test Facility (HTTF) to model a Very High Temperature Reactor (VHTR) during a DCC accident scenario [8]. The HTTF will provide benchmark data for existing safety analysis codes. For the modeling it was assumed that the Boussinesq approximation is valid and the fluid is incompressible. This facility would model the DCC conditions where there is a LOCA scenario and air ingress. It is expected that the air being colder would collect in the lower plenum, and transiently diffuse through the helium. As the core of the HTTF will be very hot a ceramic core was designed. The final scaled model was 1:4 length scale and 1:2 time scale. It operates at a temperature of 687 °C and 259 °C for the inlet and outlet respectively, but only at a low pressure of 0.8 MPa, so the modeling begins once the depressurization of the prototype is complete[18]. Figure 2-5 shows the geometry of the HTTF [19].



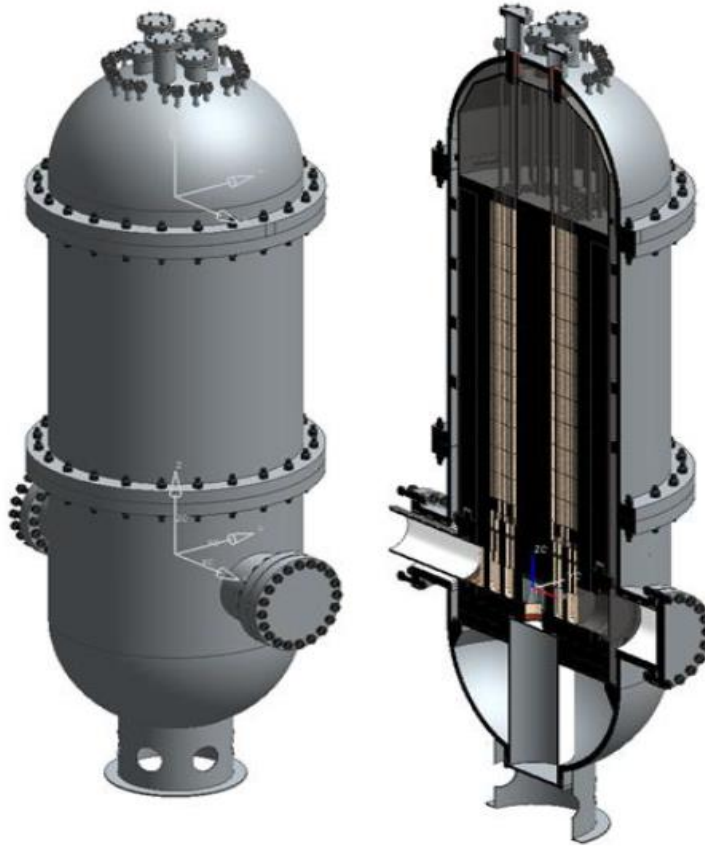


Figure 2-5: Oregon State University's high temperature test facility

### 2.3 Previous Studies – Particle Image Velocimetry

Particle Image Velocimetry can measure large or small flow fields instantaneously in a non-intrusive manner. This is very beneficial for flow analysis. Figure 2-6 shows a schematic on how PIV functions [20]. PIV is executed by injecting small particles into the working fluid. Two laser pulses are fired in quick succession that illuminates the particles. A high speed camera captures the 2-D laser sheets of illuminated particles. When a picture

is taken the high speed camera interprets the intensity of the light reflected by the particles as a value. It takes this value for each pixel and represents this value in a digital image as something similar to a signal.

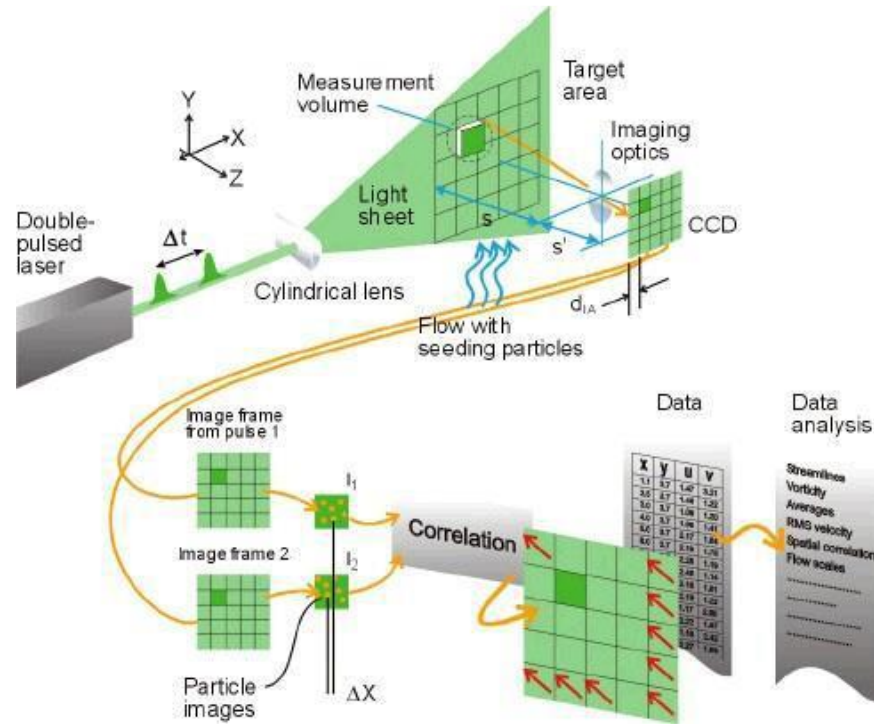


Figure 2-6: PIV Schematic

To compare the pictures the images are subdivided into several “interrogation windows”. Each interrogation window is comprised of multiple pixels. Next a cross correlation function is used to compare the two images or image pair. The below equations is used in direct cross correlation.

$$R_{AB}(s) = \iint A(X)B(X + s)d^2 X \quad (2.7)$$

A and B store the light intensity of each pixel which can be extracted similar to a matrix.  $X$  is the domain of an interrogation window,  $R_{AB}$  is a correlation value between an interrogation window of the first image compared with a nearby interrogation window in the second image which essentially represents how close the pattern of one window compares to the other. The variable  $s$  is the displacement vector between these two windows.

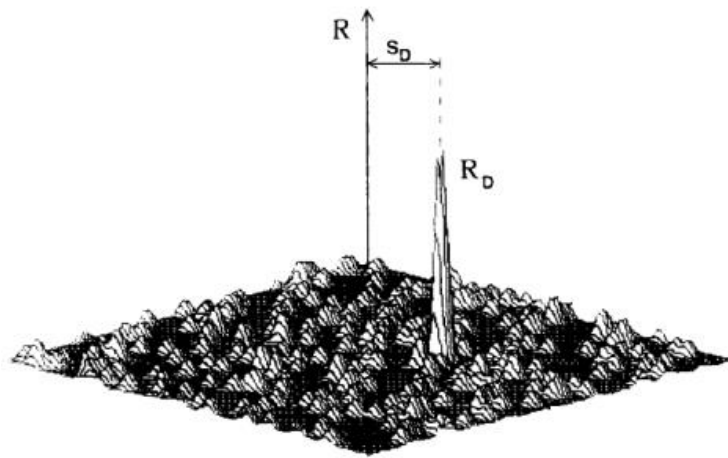


Figure 2-7: Cross Correlation field

Cross correlation integrates through the domain of  $X$  to give a total correlation value between the two windows. After all nearby windows have been scanned you would have a field of values as represented in Figure 2-7 [21].  $S_D$  would be the displacement vector for that pair of interrogation windows. Once all the nearby windows have been cross correlated then the highest correlation value is selected and the displacement vector is set.

The problem with this method is it is computationally slow. However applying the Fourier Transformation greatly reduces the calculation time, this method is called the Fast Fourier Transformation (FFT), which transforms convolution equations shown in equation 2.8 to equation 2.9 [22]. The cross correlation equation 2.7 has the same form as the convolution equation 2.8 so FFT may be applied to it removing one of the integrals. The cross correlation still needs to scan all the nearby interrogation windows of the paired image, however FFT removes the need to integrate through the domain of  $X$  for each window.

$$C_{fg}(\Delta x) = \int_{-\infty}^{+\infty} f^*(x)g(x + \Delta x)dx \quad (2.8)$$

$$C_{fg}(\Delta x) = \mathbb{F}^{-1}[F^*(k)G(k)] \quad (2.9)$$

Using this method one can get the instantaneous velocity field, however sometimes the time-averaged velocity field is of interest particularly if testing for statistically steady state. There are different methods for time averaging[23]. There are three primary steps in PIV: Obtain the particle images, generate the correlation functions, and then run the peak detection which essentially is generating the velocity vectors. One time-averaging method is the Average Velocity Method, which averages the instantaneous velocity measurements. Instantaneous velocity measurements will have some erroneous velocity vectors, but they can be removed by filters that compare the velocity vectors with

nearby vectors and removes them if they vary significantly from the standard deviation of the neighboring images. This study uses this method for the time-averaged velocity field. Another method is to average the images themselves. This can be beneficial when the particle density is low or if the interrogation window is small, although can be detrimental if there is a large number of images. The last method is to average the instantaneous correlation functions for each image pair. This method is good for reducing the noise to signal ratio and also reduces the probability of erroneous measurements, but must be implemented directly in the PIV code.

When running PIV analysis there can be false or spurious vectors that do not follow the flow regime, by either varying greatly with the neighbor vectors or not being physically possible. These vectors will occur when either there are an insufficient number of particles or there is a low signal to noise ratio [24]. To correct this an algorithm can be developed to correct the false vectors. The first step in this algorithm is to find a region of coherent vectors. To do this an equation is used to compare one vector with its neighboring vectors,

$$val = \frac{\sum_i |v_i - v_0|}{\sum_i |v_i|} \quad (2.10)$$

Where  $v_0$  is the vector of interest and  $v_i$  represents the neighboring vectors. Where this value reaches a minimum represents a region of uniformity. Once found the algorithm sweeps the vector field finding all vectors coherent with the first group by checking the neighboring vectors and seeing if they differ by less than a given amount specified by the user. Once the region has expanded until the neighboring vectors differ too largely the

algorithm searches for another region to build off of. The sizes of the region generated will vary in size depending on the uniformity of the flow; in highly turbulent areas the regions may only contain a few vectors. Once all the regions have been generated they are checked again for any deviant vectors. The vectors that do not make it into any regions are removed. This method does require user input values that impact the sensitivity of the algorithm, but experiments have shown the impact to be low.

A study in Japan performed PIV and planar laser induced fluorescence (PLIF) for the mixing process of a turbulent jet[25]. The jet was ejected at a Reynolds number of  $2 \times 10^3$  with a jet velocity of 2 m/s. Small particles were injected for PIV and a fluorescent dye was added for PLIF. During the experiment the dye and the particles were recorded separately. The dye was not used to measure temperature but to measure the concentration, 67 frame pairs were averaged at several cross section locations. Using this several profiles of the mean velocity, turbulent intensity, Reynolds shear stress, mean concentration, concentration fluctuation, and the turbulent flux were obtained and validated by comparing the results with previous studies. Due to the short duration of the experiment not enough data was gathered and there was significant discrepancy with some of the data, particularly with the turbulent flux and concentration fluctuation. To correct this the study suggested to simply extend the duration of the experiment and to modify the ratio of fluorescent dye and exposure time of the camera.

For normal operation the core operating temperature profile is important, and there may be severe thermal stresses in the lower plenum, but there isn't

much of interest in the upper plenum as the coolant is coldest there. For the Depressurized Conduction Cooldown scenario the air ingress occurs in the lower plenum, and slowly diffuses into the core where it oxidizes with the fuel. Multiple computer codes have ran simulations to monitor the phenomena in the core and the lower plenum for both normal operation and a DCC accident scenario, and experimental models have been built to validate the codes. There has been some CFD analysis for the upper plenum for a PCC scenario; however there is no benchmark experimental data to validate the results. The experimental facility that was designed, constructed, and tested in this study can produce results to fill this deficiency of data.

### **3 PROJECT DESIGN**

#### **3.1 Solidworks Design Phase**

INL initially provided a rough design shown in Figure 3-1. Initially a 1/8<sup>th</sup> scaled design was considered however the required heat input for modeling a VHTR was too large, so a 1/16<sup>th</sup> scale design was chosen. The basis for the design was a closed loop system where the flow was driven purely by natural circulation. The inlet to the test section would go into the lower plenum where the water is then drawn up through heated pipes by natural convection. The water would then leave the pipes simulating slow jets into the upper plenum, the region of interest. The water would then exit the upper plenum into the downcomer, the region between the modeled core and the outer containment. A heat sink, which they called a water cooling jacket, would need to remove the majority of the heat input so that the system could reach a statistically steady state and to help induce natural circulation. As it goes to the downcomer the water will lead to the outlet and into a reservoir of water from which the inlet pulls water through.



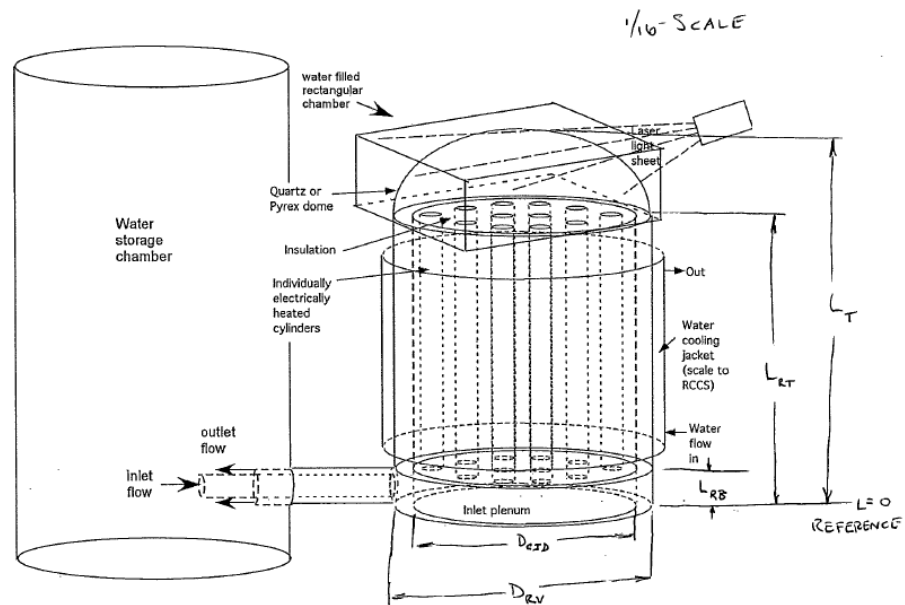


Figure 3-1: Initial Design Geometry

Initially the design had a concentric pipe that would contain both the outlet and inlet. But during the design phase in Solidworks this was determined to greatly complicate the model and would make the assembly and fabrication challenging. Two separate pipes for the inlet and outlet were used since the region of interest was the upper plenum and having the inlet and outlet be two separate pipes wouldn't affect the experimental testing or results. Next the pipe layout needed to be determined. Through collaboration INL made the final design of 25 pipes with a  $\frac{3}{4}$  inch inner diameter arranged in a hexagonal pattern equidistant from each other, as shown in Figure 3-2. Initially an annular pattern was

considered however the pipes needed to be equidistant and that wasn't possible for the annular design, so a hexagonal pattern was used instead.

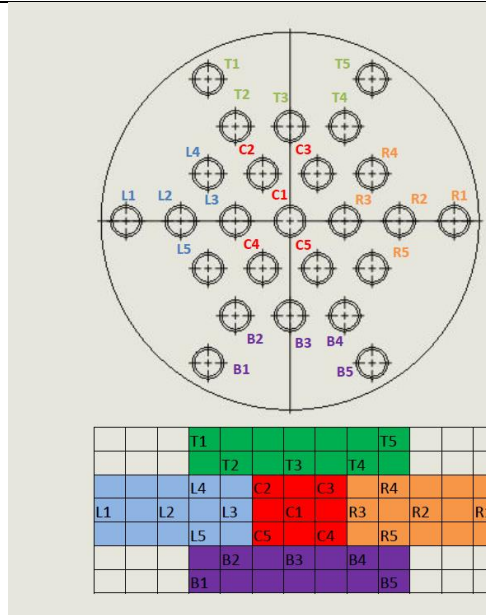


Figure 3-2: Pipe Layout

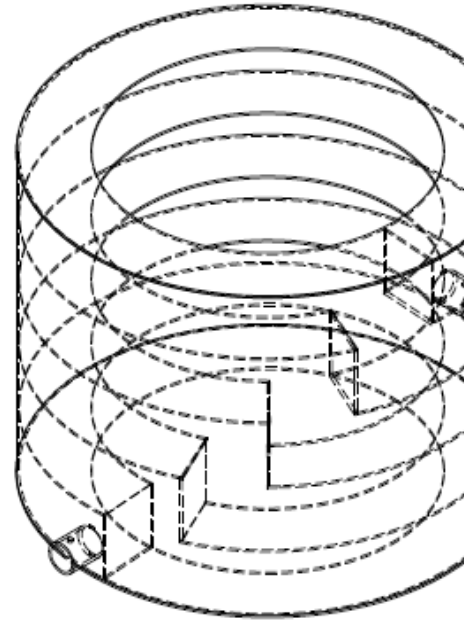


Figure 3-3: Cooling Jacket Design

For the heat sink multiple methods were considered. Typically to remove heat from fluid a series of coiled tubing is built into the flow path and cold water is pumped through them. For our design the tubing would go between the outer containment and the core containment. However that would create a large pressure drop for our system which is already at a low pressure differential since there is no pump being used. This means that the heat removal must be external. To design an external uniform heat removal cooling jacket a series of baffles that would be connected to the outside of the containment. This means the material needed a high thermal conductivity, stainless steel was chosen. The

final design included a series of five baffles where the water would be pumped into the bottom, circulate around the containment, and then rise 3.5 inches and repeat the process until it reached the outlet of the cooling jacket, shown in Figure 3-3.

Next the design process for all the parts began. The geometry from INL included only the measurements for the fluid region. Free reign was given for designing the experimental components. When designing the largest parameters were how to have waterproof access to the core for wiring, fabrication limitations, ease of assembly and disassembly, and data acquisition. Four iterations of designs were considered and discussed with the fabricators and colleagues, mainly deciding how to waterproof and have access for wiring, until the final design was chosen and shown in Figure 3-4 and Figure 3-5.

All grey parts are made of polycarbonate and the blue parts are stainless steel. Polycarbonate was chosen for its opaqueness and the ability to withstand high temperatures, as well as ease to manufacture. Stainless steel was chosen for its conductivity, durability, and price. The lower plenum was straightforward, the inner diameter and height were determined by the reference geometry. On top of the lower plenum sits the core containment which is connected by a flange and sealed with an O-ring. The core containment starts with a two inch plate. In the center of the plate there are 25 x 3/4 inch holes that match the ID of the piping chosen. At the edge of the plate 10 holes located radially are drilled in from the edge, and then holes are drilled on the top of

the plate that intersects with the other holes. This is used for wire access to the core. A one inch high cylinder is cut into the center of the plate which will be discussed later. Next a large hollow cylinder was welded onto the plate which acts as the core containment.

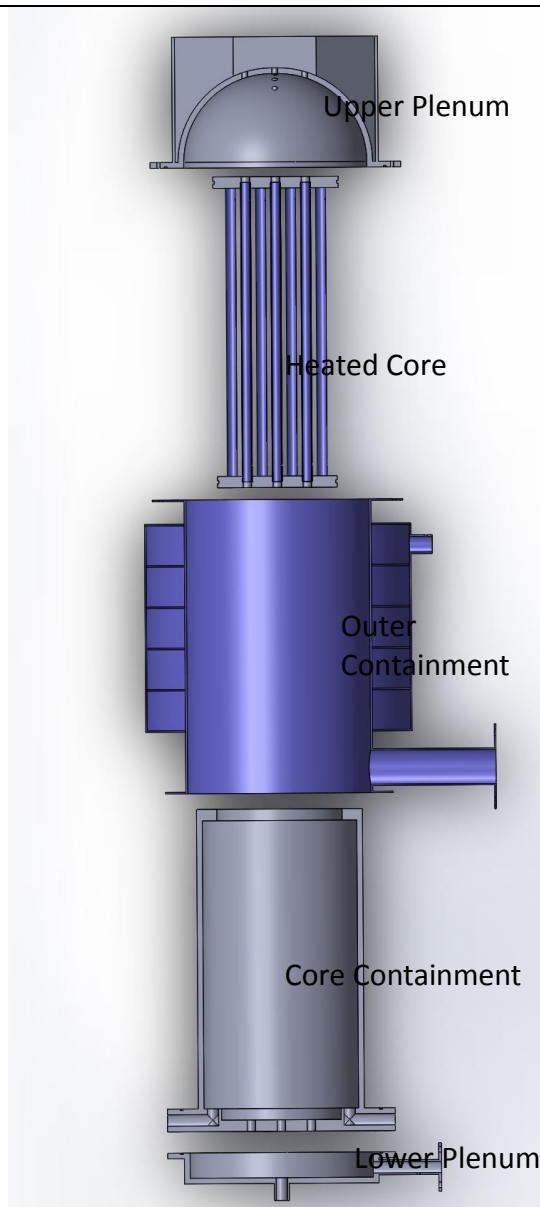


Figure 3-4: Exploded cross section

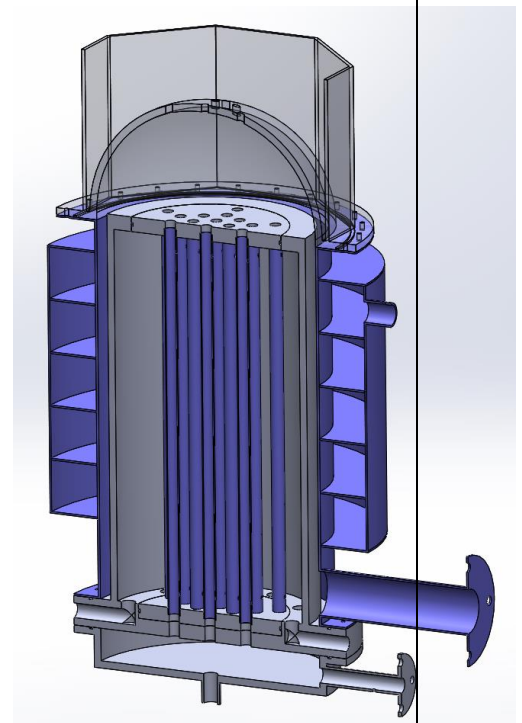


Figure 3-5: Cross section after assembly

Next is the outer containment to which the cooling jacket is welded. It sits on the core containment and is sealed with an O-ring. A 3/4 inch gap exists between the core containment and the outer containment as given by the INL geometry, this acts as the downcomer for the fluid. A large diameter outlet was chosen so the fluid may enter it easily. The cooling jacket was not placed at the exact exit top of the containment because the last baffle wouldn't be perfectly uniform since the temperature of the fluid will rise as it circulates the downcomer, lowering it a few inches would inhibit the affect it will have. Next the core can be inserted. The core consists of a bottom plate with a 10.5" diameter and 1" thickness. It has 25x 3/4" holes that are countersunk 1/2" to match the outer diameter of the steel pipes. The twenty five steel pipes are inserted into these holes each of which has their own O-ring. The steel pipes have two threaded holes near the top and bottom of the pipe that can be used for compression fittings for thermocouple access. The top of the pipes are then inserted into the top plate which is similar to the bottom plate but has a diameter of 11". Once the core is assembled it may be dropped into the core containment. The top and bottom plates seal the containment with O-rings.

Finally the upper plenum is placed on top of the steel containment where it is sealed with a flange and O-ring. Again the half-sphere geometry was designed to match INL's specification. The top of the sphere has nine threaded holes for compression fittings for thermocouple access to the upper plenum. A correction box is glued outside the dome which is used to correct the distortion from looking onto a curved surface filled with water. Once the correction box is filled with water a flat surface is presented that can be used for imaging. Originally a square box was used but this limited pictures to be taken on four

planes and had bolts for the flange inside the correction box which would be difficult for assembly. Instead an Octagonal shape was chosen. With this the final design was sent to the fabricators.

### **3.2 Project Assembly**

As the parts were being fabricated the thermocouples were made to measure the temperature rise in the piping, cooling jacket, and inlet and outlet of the system. After consulting with Omega, a thin T-type thermocouple was selected. The wire was cut into approximately seven foot lengths. One end was stripped and welded together with an arc welder. The thermocouples were hooked up to a National Instruments data acquisition system and measured with Labview. They were then calibrated with a Fluke Thermometer at the approximate temperatures of 20 °C and 80 °C. Once this was completed the steel piping with the threaded holes were acquired early since their machining process was simple and short. Compression fittings were screwed into the pipes and thermocouples were installed. To test for leaks one end of the pipe was sealed while the other end had an extended pipe attached to it to simulate the head pressure it would be operating under. Originally Teflon tape was used to seal the thread, however only nine out of ten were successfully sealed. Different techniques were considered such as using epoxy but eventually it was decided to take them to a welding shop and weld the compression fittings to the pipes to fully ensure they wouldn't leak. After this the scaffolding to house the experiment was designed and constructed. Unistrut beams were used to construct it, the

design is shown in Figure 3-6. Many supports were built under the experimental facility and the water reservoir.

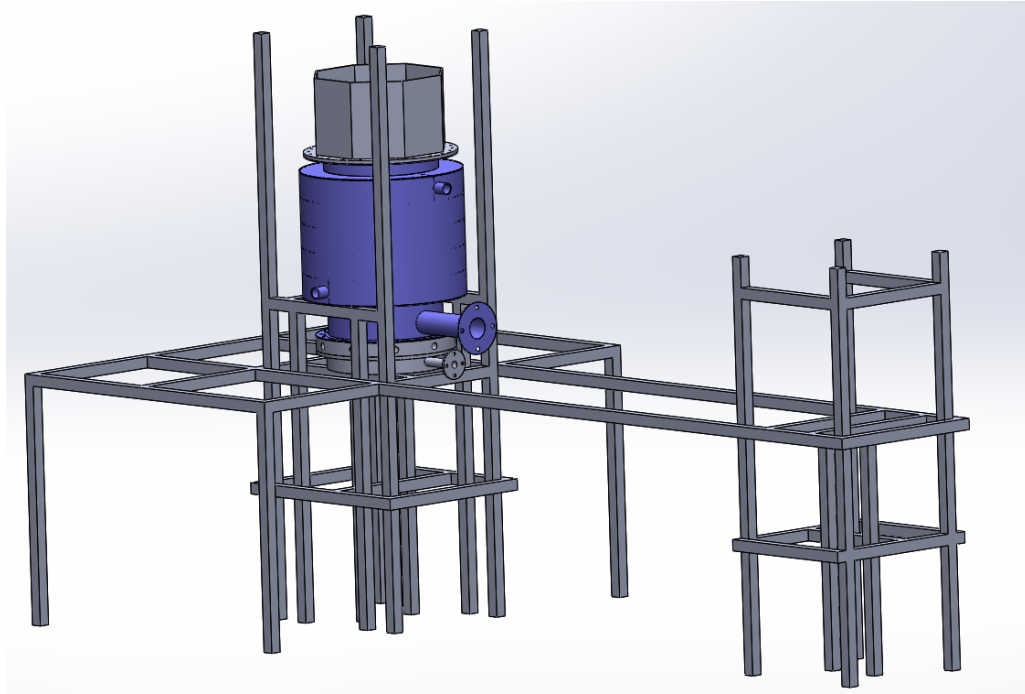


Figure 3-6: Experimental scaffolding

Next the twenty five heating tapes were acquired and tested. The average resistance was approximately 89 ohms with a standard deviation of 2. The heating tapes would be controlled by five variable voltage transformers. The piping was broken into five groups of five as shown in Figure 3-2. The heating tapes were grouped by similar resistances. When we finished testing the heating tapes the machining of the experiment's parts completed. Figure 3-7 shows the pipes with heating tapes and thermocouples inserted into the bottom plate. Figure 3-8 shows the core containment on top of the lower plenum. The design allows the core pipe configuration to be oriented with the inlet in different

patterns. One could either have three pipes in line with the inlet and seven pipes in the symmetric plane, or vice versa. This assembly had the core containment bolted onto the lower plenum such that the seven pipes would be in the symmetric plane. Figure 3-9 shows the reservoir tank which was selected so the height would be greater than the experimental facility's height.



Figure 3-7:  
Piping,  
heating  
tape, and  
thermocouples



Figure 3-8:  
Lower plenum  
and core  
containment



Figure 3-9:  
Reservoir  
tank



Next the insulation for the core was installed. The insulation was important to keep any heat from leaving the core and heating the downcomer which would inhibit the natural circulation. A high temperature ceramic insulation that uses aluminum silica was selected. It was cut into strips and inserted between the pipes. Then a larger sheet was wrapped around the core and taped as shown in

Figure 3-10. Ropes were looped down one pipe and up a different pipe to lift the core and drop it into the containment wherein the ropes would be extracted. The core was slowly lowered into the containment and the wires were drawn out through the holes. Once installed more insulation was stuffed around the outside shown in Figure 3-11.



**Figure 3-10: Insulated core**



**Figure 3-11: Core and containment**

Once installed the top plate of the core needed to be sealed. With a coordinated effort the twenty five pipes were line up with the plate and force was applied till the O-rings were sealed and the plate was flush shown in Figure 3-12. Next a lift was used to

lower the steel containment around the core containment shown in Figure 3-13. Once the lower flange was sealed the upper plenum was placed onto the steel containment and bolted in. A custom gasket was made to seal the upper plenum and steel containment since the flange on the steel containment was wavy and not level.



Figure 3-12: Top plate flush with containment

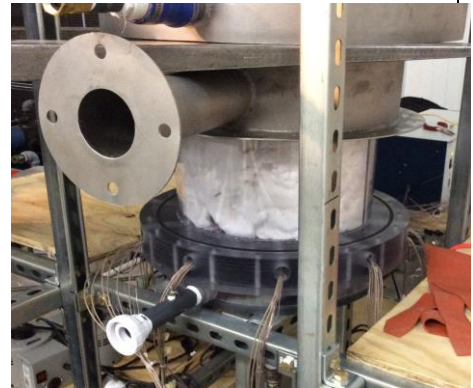


Figure 3-13: Outer containment being lowered

Now the test facility was ready to be attached to the reservoir and filled with water. Figure 3-14 shows the view of the assembled facility filled with water and Figure 3-15 shows the top view of the upper plenum to show the inlet pipes and the downcomer. It should be noted that there was one difference between the design and machined parts. When forming the dome of the upper plenum a sheet of polycarbonate is heated till its malleable and then sucked into a vacuum creating a bubble. The height of the dome is determined by how much the plastic could deform before it hardened. The dome size made by the fabricators was insufficient to match the height of the design. To compensate for the difference in height between the design and the fabricated dome the remaining height

was glued on as a cylinder. This was deemed insignificant in altering the fluid behavior for generating benchmark data. Once the facility was attached to the reservoir and filled there were some external leaks in the piping but they were fixed by adding additional Teflon tape and gaskets where needed. Once the leaks were fixed a few tests were run to perform the shakedown of the test facility. A shakedown is essentially a process where the facility is tested to confirm everything is working in proper order. A few thermocouples had broken in the installation process. Most could be



Figure 3-14: Assembled Facility



Figure 3-15: Top view of upper plenum

fixed externally by splicing the break in the wire, but two remained broken inside the core and inaccessible. After the facility was filled about five times we noticed

something was wrong with the heating tapes. When five heating tapes are grouped in parallel the total resistance is approximately 18 ohm. However two of the groups read around 22 ohms indicating that two heating tapes had failed. Moisture had slowly leaked into the core, soaked into the insulation, and gotten some heating tapes wet. This caused the heating tapes to fail. Unable to operate with a non-uniform core and the risk of shorting more heating tapes meant the facility had to be disassembled and the leak addressed.

The source of the leak could not be determined from the disassembly, but it was likely from the bottom of the core as the insulation was moister and was at a higher pressure. There were several possible causes though. One was the thermocouples connected to the compression fittings. They were originally sealed into the fittings using Teflon tape and they passed the test but over time a few of them may have begun leaking. Another possibility was the pipes connection to the bottom plate using the O-rings. No lubricant was used when inserting the pipes into the O-rings so some of them got damaged in the assembly. The last possibility was the groove on the bottom plate for the large O-ring was close to the countersunk holes for the pipes furthest from the center. To account for this possibility a thin layer of epoxy was applied at possible leak locations. For the O-ring problem the damaged O-rings were replaced, and a lubricant could be used in the next assembly. To prevent the leaking from the compression fitting would require extra work.

First no matter what precautions were taken there would still be the possibility something would fail. To protect the heating tapes each heater was water sealed individually. To accomplish this first heat shrink tubing was used to seal the leads coming

from the heaters. Next high temperature silicon tubing was wrapped around the heaters and sealed with a high temperature adhesive. The pipe was clamped until the adhesive was dry as shown in Figure 3-16. This tubing sealed the pipes from water and also acted as insulation. Once this was completed for all 25 pipes a partial reassembly was done. It was the same as the previous assembly except lubricant was used and the assembly stopped before the core was sealed off. The facility was filled up to the top of the pipes. This confirmed that there was some leakage from the thermocouples. Thermocouples are two wires with a plastic coating holding them together. Between the wires there is a groove that may have been the cause of the leak. The next step was to seal off the thermocouples.



Figure 3-16: Sealing the heating tapes with silicon tubing and adhesive

Once all the broken thermocouples were replaced a new method of inserting the thermocouples into the compression fitting was devised to prevent leaks. Fine steel tubing was cut into short lengths and the thermocouples were threaded through them. The thermocouple was then sealed on both ends of the tubing with a UV epoxy. UV epoxy

is liquid until a UV light is shone on it which causes it to harden in a few seconds. After this ferrules are slid over the tubing. When the compression fitting is tightened the ferrule clamps down on the tubing causing it to compress and seal. The final result is shown in Figure 3-17.

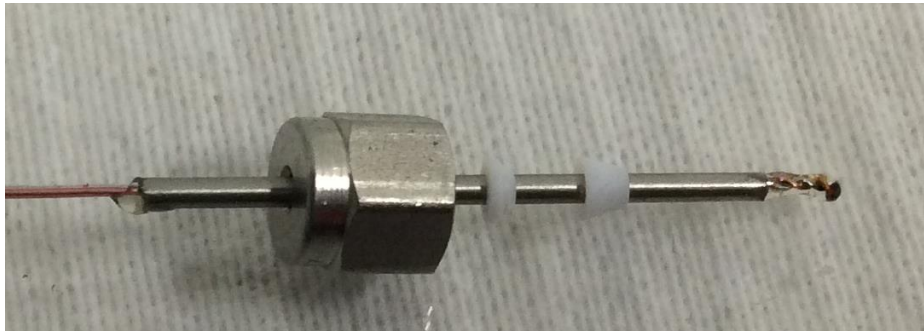


Figure 3-17: Thermocouple with tubing, epoxy, and ferrules

Once completed for all 50 thermocouples a few more tests needed to be performed before reassembly. The heating tapes and thermocouples were tested and all functioned properly. A partial reassembly was performed and tested for leaks and none shown. Satisfied a ring of insulation was added around the core, and the top plate was inserted sealing off the core shown in Figure 3-18. This was much more difficult as the silicon tubing had to be compressed slightly to allow all 25 pipes to simultaneously line up with their holes, but was accomplished using clamps. Once completed the upper plenum was installed and the reassembly finished, the facility was ready to start testing.





Figure 3-18: Core top view after reassembly

### 3.3 Data Acquisition

The experimental facility has several data acquisition devices installed to monitor the test that can be used to produce benchmark data for CFD validation. This is outlined in Figure 3-19. The first measurement is the thermocouple to read the temperature at the inlet to the facility. Then as the water flows up through the core thermocouples measure the temperature rise in all 25 pipes. When the fluid enters the upper plenum PIV is performed to record the velocity flow field. The fluid then goes to the downcomer and to the outlet. A pressure transducer will measure the pressure difference between the inlet and the outlet. On the outlet pipe an ultrasonic flowmeter will measure the total flow rate of the system.

Since the thermocouples were made and not purchased there is no accuracy range. To calculate the precision of the thermocouples the standard deviation

may be calculated post-test. The accuracy can be calculated by inserting a trusted reference thermocouple into the upper plenum and measure the temperature at the outlet of the pipes during the test, and comparing that measurement with the thermocouples that were made. For all data recording a SCXI -1600 model DAQ with three control modules was used. The differential pressure transducer is from Honeywell and could measure a range of  $\pm 0.5$  PSID with an accuracy of  $\pm .25\%$  of the full scale. The cooling jacket used a paddlewheel flowmeter that had a range of 3-30 GPM and an error of  $\pm .06$  GPM. The flowmeter for the coolant loop of the system was an ultrasonic flowmeter from Krohne. An ultrasonic flowmeter was used because it is non-intrusive. It was attached to the 3" outlet pipe to obtain a better signal and higher accuracy. The flowmeter had an error of  $\pm 1\%$  if the flow was greater than 0.5 m/s. However since the natural circulation flow was much less than that it was calibrated with a Optiflux 1000 Electromagnetic flowmeter that had an accuracy of 3% at the slow flow rate the experiment was running at.



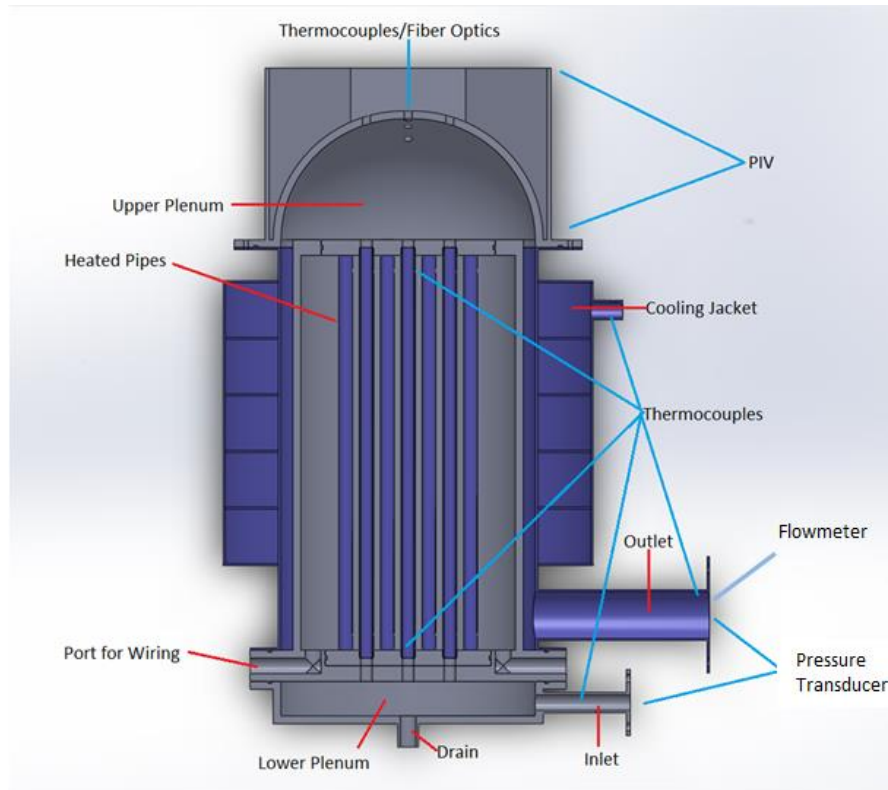


Figure 3-19: Cross section for data acquisition

A separate pipe was connected in line with the Optiflux flowmeter as shown in Figure 3-20. The ultrasonic flowmeter measured significantly but consistently different from the electromagnetic flowmeter. The ultrasonic flowmeter recorded the flow for seven minutes and the averaged flow rate was compared to the flow rate measured by the electromagnetic flowmeter. This was performed at six different flow rates between 0.2 and 1 GPM. Shown in Figure 3-21 the data fit a linear trendline well, and the equation was used to correct the flow rate measured in the tests.

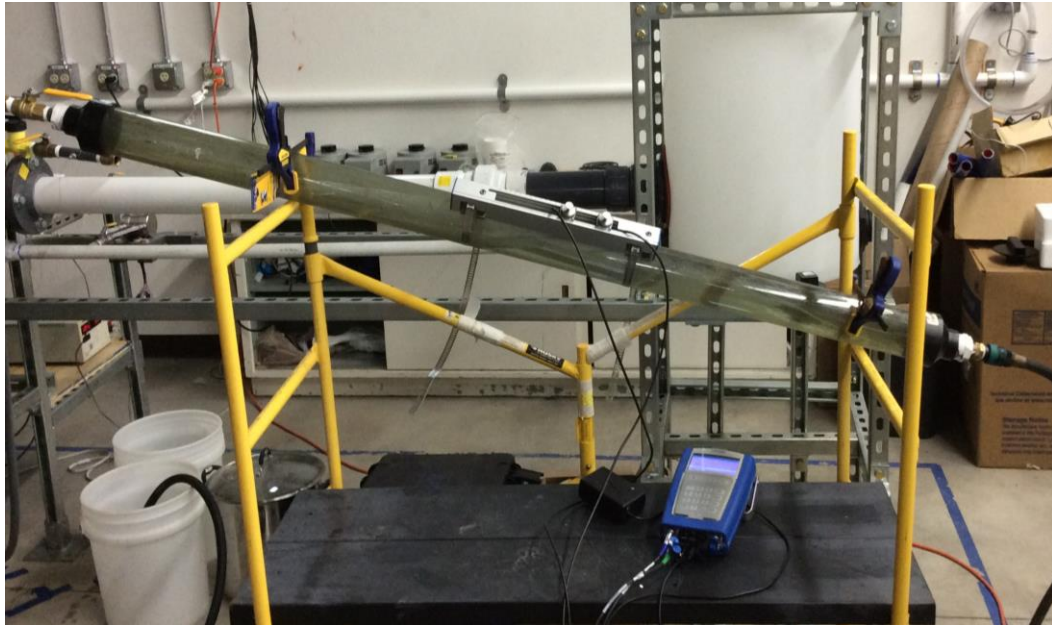


Figure 3-20: Calibration test for flowmeter

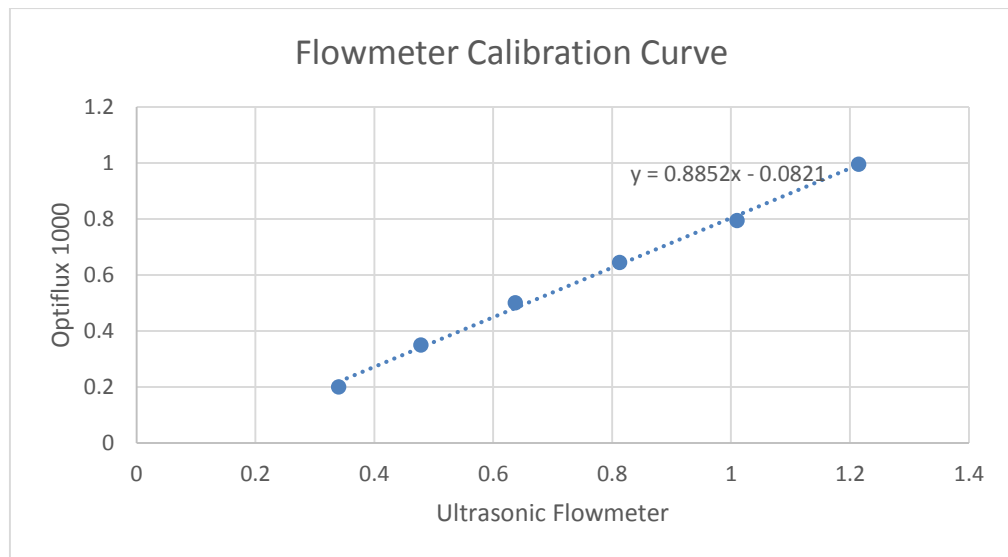


Figure 3-21: Calibration curve for flowmeter

For the PIV system a Vlite series dual pulse laser system that operated at a wavelength of 532 nm and had a frequency range of 1-15 Hz was used. A High speed camera MEMRECAM GX-3 was used for the imaging. It produced high definition images with 1280x1024 pixel size. The camera and laser were connected to a waveform generator that timed the pulse and the shutter of the camera to activate simultaneously. Next the correct particles needed to be chosen. Initially 20 micron glass bead particles were used. However the pictures taken had light "noise" from the laser reflecting off parts of the experiment and illuminating small scratches on the plastic which would block vision of the particles. The final particles used were fluorescent polyethylene microspheres which ranged from 20-40 microns. The densities of these microspheres were 1.002 g/cc so the difference in density with the fluid would have a negligible effect on the particles tracking the fluid. The fluorescent particles would reflect the light from the laser as a different color so a filter could be used on the camera that would remove the 532 nm wavelength green color of the laser. This resulted in a much clearer image, as shown in Figure 3-22.

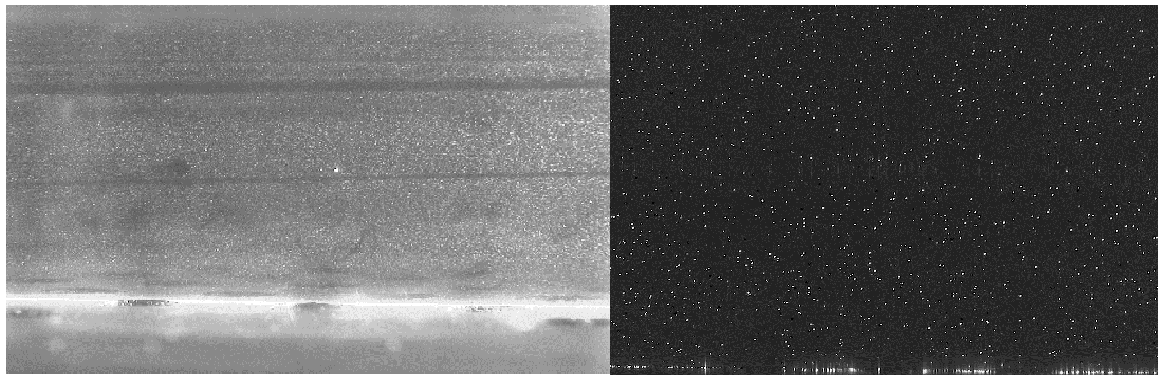


Figure 3-22: Glass bead particles vs Fluorescent particles



## **4 TESTS AND RESULTS**

### **4.1 Testing**

When booting up a test water is pumped into the reservoir which simultaneously fills the experiment equaling a total of approximately 50 gallons. Once filled and no leaks were detected the heaters were turned on. The heating tapes are essentially electric coils around the pipes. When 25 of the electric coils are turned on an electromagnetic field is generated. This put a small voltage in the water. The thermocouples uses a voltage signal so whenever the heaters are on the thermocouple values are greatly skewed, however as soon as the heaters are off they function normally. This means that measurements can't be made continuously for transient measurements, but the heaters could be turned off, data recorded, and turned on again for steady state measurements. Additionally touching the cooling jacket and another metal object would induce a small shock.

For this study only one group of five pipes were turned on and the outlet of three of the pipes were studied, as shown in Figure 4-1 and Figure 4-2. Initially the testing was focused on generating quality images that could be processed with PIV software. Several parameters were tested until an optimal setting was chosen. The laser power level was adjusted till the optimal power output was found. Too much and there would be noise and the particles could not be detected, too little power and the particles wouldn't reflect enough light to be detected. Next the camera was tested. A mount for the

camera was constructed that allowed it to move in three dimensions until the desired window was chosen. Eventually the camera was mounted approximately 90 cm away from the correction box and a magnification lens was used to record the region shown in Figure 4-2. The cross section includes three adjacent jets. Because PIV gives 2-D components for the velocity vectors the other two pipes should have an insignificant effect on the velocity profile. If stereoscopic PIV was used that returned 3-D components then the flow profile may be altered.



Figure 4-1: Pipe layout with closed pipes

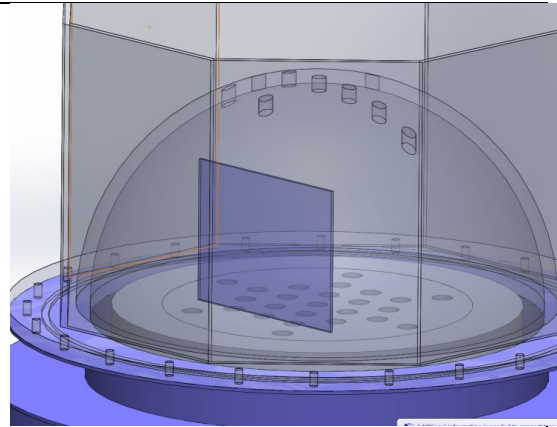


Figure 4-2: Analysis region

Once the camera and laser were mounted appropriately the test was prepared for steady state data recording. Previous testing revealed that steady state was

when the outlet of the pipes into the upper plenum reached  $45^{\circ}\text{C}$ , this is when the cooling jacket was turned on. The maximum flow rate for the cooling jacket was approximately 10.7 GPM determined by the head pressure at the research building. The flow could be controlled by opening and closing a valve, but the tests were run with the full flow rate. To monitor reaching steady state the outlet of the core piping was monitored, as well as the inlet and outlet of the apparatus. The cooling jacket removed a sufficient amount of heat such that the inlet and outlet temperatures were less than  $1^{\circ}\text{C}$  different. It took approximately 90 minutes to reach steady state.

Once steady state was achieved particles were injected into the inlet of the experimental apparatus. This was allowed sufficient time to circulate into the upper plenum before data was recorded. Then the camera began logging pictures at a rate of 10 Hz, and the flowmeter began logging data. The camera memory can hold approximately 2200 images so the memory is full after four minutes of logging data. Once full the laser was turned off, the flowmeter stopped logging data, and the heaters were turned off so that Labview could record the temperature and pressure differential. This was run five times with the camera in the same position, however two of the times the flowmeter didn't save the data so three sets of data were analyzed for this study.

## **4.2 Analyzing**

Now that the images were acquired the PIV software needed to be selected. After trying different open-source programs PIVlab was selected. PIVlab was written with a Matlab script. It has good processing speeds, data output format, image pre-

processing, vector validation, and can make videos of the vector fields. It is also easy to use with minimal experience. Using PIVlab the 2000 images were imported into PIVlab with a 1-2, 3-4 format giving 1000 image pairs as it was estimated that 1000 image pairs would be more than enough to record statistically steady state. Before running the image pre-processing may be modified, such as the interrogation window size. For this test ran two passes with 64 and 32 pixel sizes. When ready all thousand images are processed and a vector is generated for each image pair. Next is the vector validation. PIVlab runs through all the images with an algorithm as described in the literature review. This removes the false vectors, which would result with NaN values in the output files. Instead the removed vectors are replaced with interpolated vectors. Figure 4-3 shows a vector field of one image pair after vector validation. The orange vectors are the ones that were replaced.



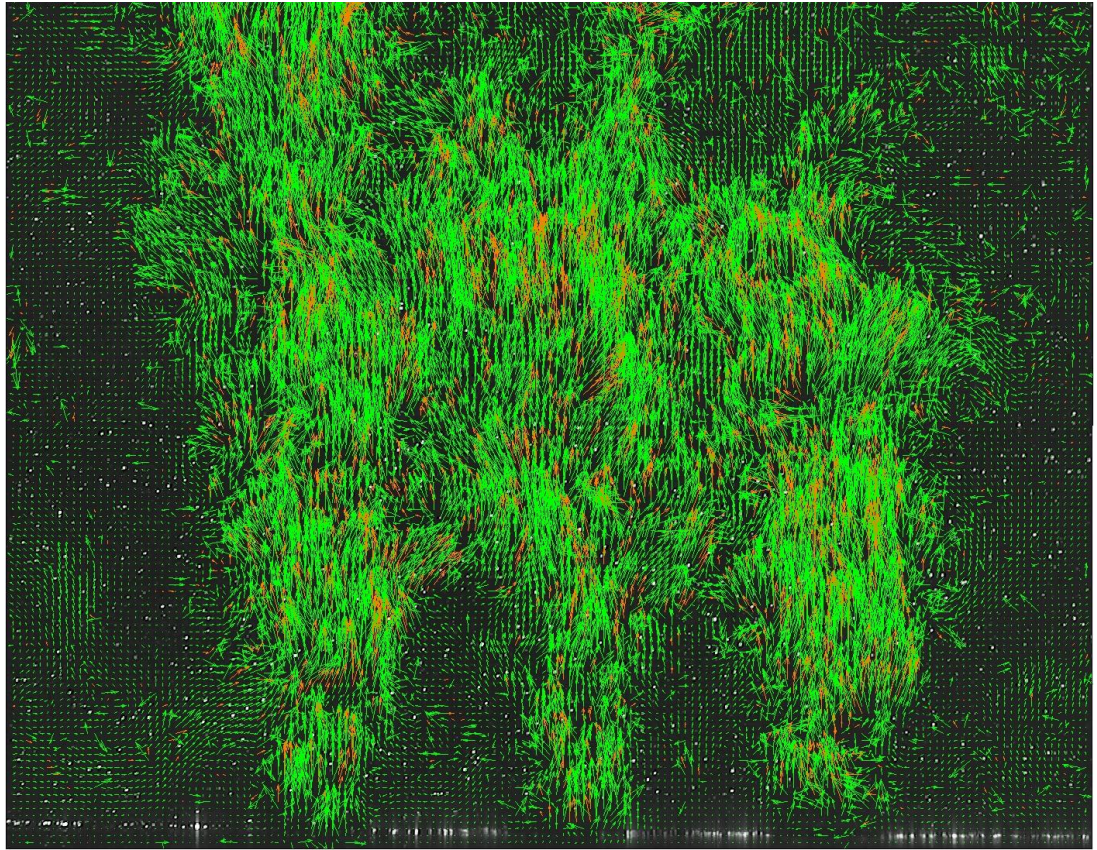


Figure 4-3: PIVlab vector field output

Once all the image pairs are fully processed the flow fields can be saved as a movie, image sequence, or saved as separate text files. The text file data is saved in five columns: x coordinate, y coordinate, x-velocity  $u$ , y-velocity  $v$ , and vorticity  $w$ . This study is interested in analyzing the statistically steady state. To do this the data must be averaged over a set of image pairs. A sensitivity analysis must be performed to determine how many image pairs are necessary to appropriately model the statistically steady state.

### 4.3 Results

First a Matlab program was developed to average the velocity vectors generated by PIVlab. This was performed for varying numbers of velocity fields from 20 up to 1000. The 1000 averaged velocity vector field was uploaded into Tecplot where the velocity magnitude was calculated. Next a 100x100 grid is created and the data is interpolated for each grid point. The velocity magnitude is plotted in Figure 4-4. Because PIVlab was written in a Matlab code it sets  $y=0$  at the first row of the matrix and  $y$  increases with each successive row.

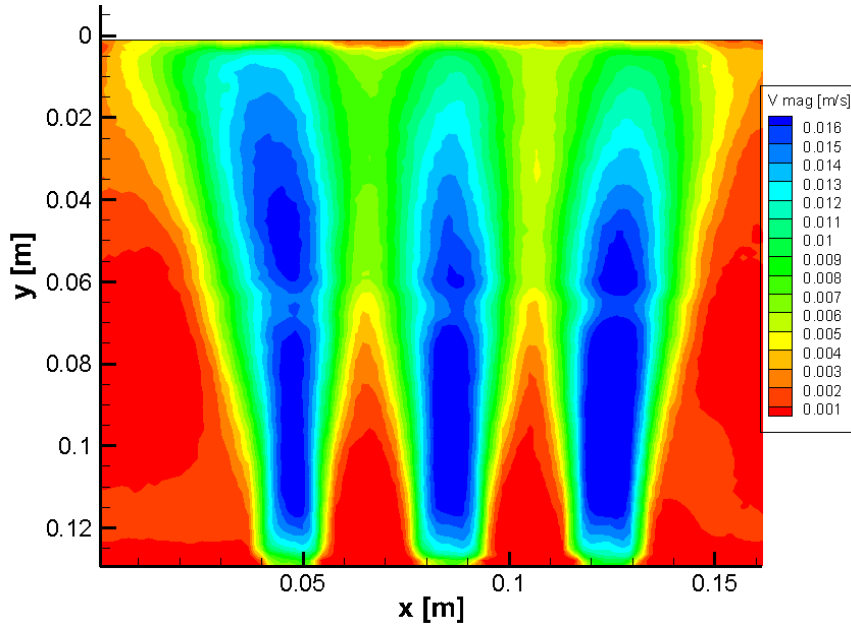


Figure 4-4: Velocity magnitude for set 2

From this contour a few distortions are apparent. First is the distortion at  $y=0.06$  m. This is due to the glued section between the curved part of the dome and the cylinder

in the upper plenum which blocks the laser sheet. This casts a shadow where particles would not be illuminated. If the particle can move past the shadow it may still be tracked. This isn't a large issue, when extracting data for benchmarking data at the distortion will be avoided. Another irregularity is the maximum velocity should be at the outlet of the pipes, however the outlet velocity is about half that of the maximum velocity. This may be due to poor seeding in the experiment.

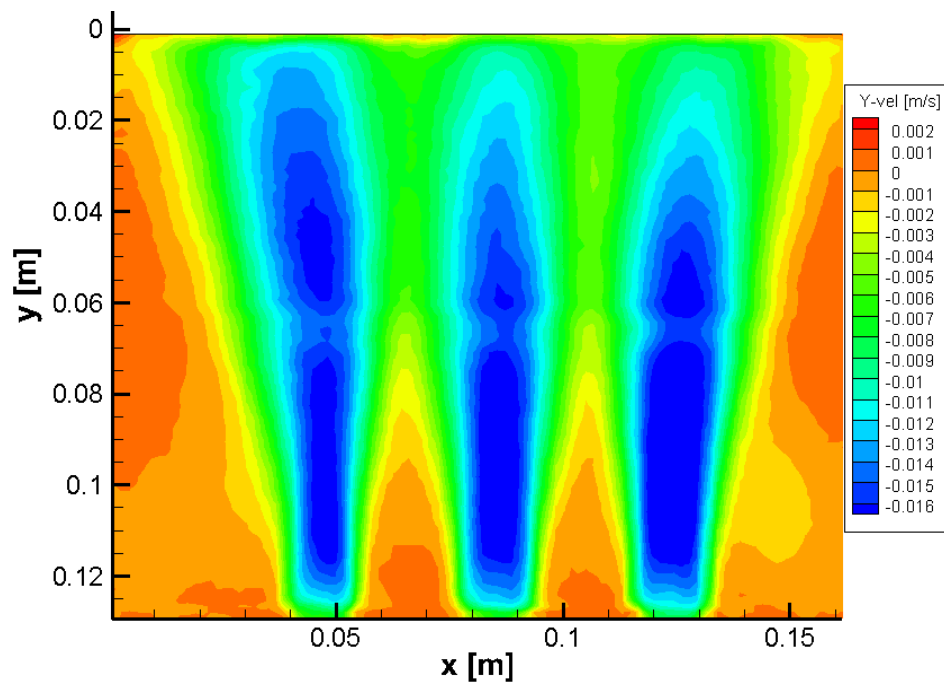


Figure 4-5: Y-velocity contour for set 2

With insufficient particles leaving the pipes PIVlab occasionally may not have a sufficient particle density to run the PIV. This would result in assigning a zero vector there. If this happens regularly then when the averaged velocity vectors over multiple image pairs the representative velocity would be lower than that of the actual velocity.

There are multiple possible methods to correct this. One is to increase the number of particles that are seeded, although this would likely only reduce the error, and the value would still be misrepresentative. Another option is to use a PIV code that recognizes when there are no particles to track and either interpolate it from neighboring interrogation windows, or apply a NaN value. Lastly and likely the surest method would be to use Particle Tracking Velocimetry (PTV) which follows the individual particles and does not use interrogation windows. Similar to the last misrepresentation, data can be extracted elsewhere that PIV functioned properly. Almost all of the flow is in the y-direction, the Y-velocity contour in Figure 4-5 nearly matches the velocity magnitude contour.

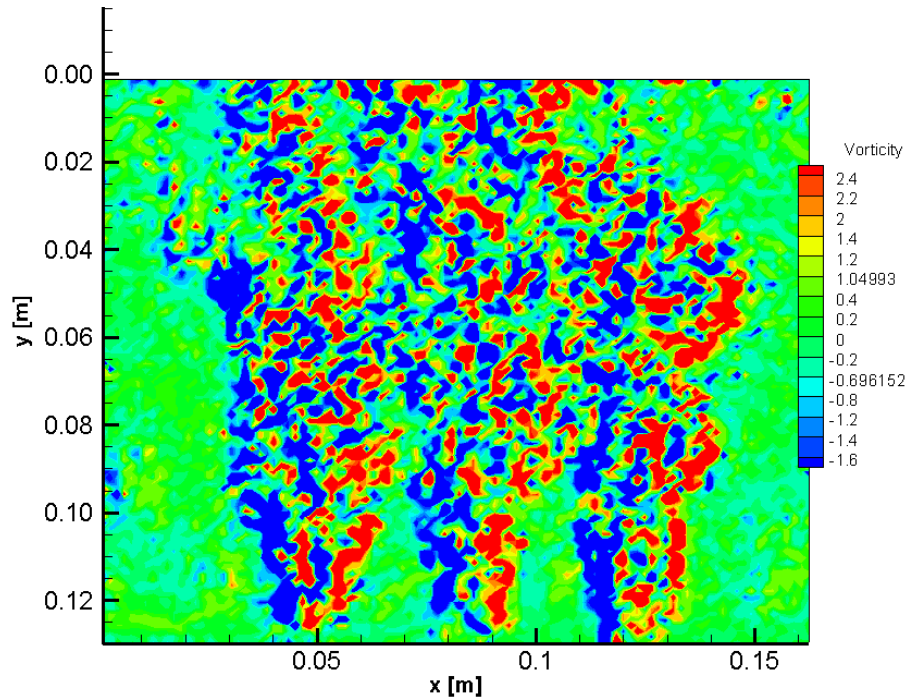


Figure 4-6: Vorticity for single image pair

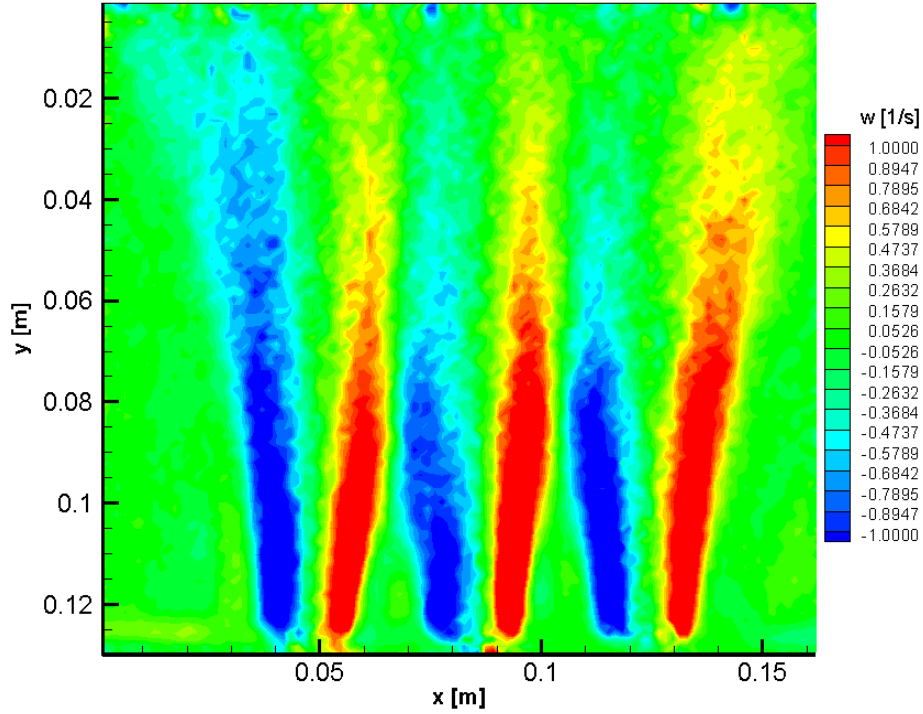


Figure 4-7: Vorticity contour for set 3

Figure 4-6 shows the vorticity field for a single image pair. The negative values represent counter-clockwise rotation or eddies, and the positive would be clockwise eddies. There is some disorder but a trend can be seen. Once averaged over 1000 image pairs shown in Figure 4-7. This shows the expected antisymmetric behavior expected from jets. Next a scaling analysis was performed to determine the required number of frames to correctly model steady state. The root-mean-squared (RMS) deviation was applied for varying numbers of frames.

$$Error = \sqrt{\frac{\sum_{i,j=1}^n \left( \frac{v_{i,j} - \overline{v_{i,j}}}{v_{\max}} \right)^2}{N}} \quad (4.1)$$

In this equation  $v_{i,j}$  represents the Y-velocity field for each frame,  $\overline{v_{i,j}}$  represents the averaged Y-velocity field for 1000 frames,  $v_{\max}$  is the maximum velocity along the jet, and N is the number of frames or image pairs. The percent error is graphed in Figure 4-8. Set 1 differs greatly from sets 2 and 3 which behave as expectedly with the error decreasing exponentially. After reviewing the images from the tests set 1 has less particle density than the other tests, which is likely the cause of the difference and suggests it may not be representative of the flow. More tests would need to be done to confirm this. However they both show approximately a 5% difference between a 700 frame and 1000 frame average.

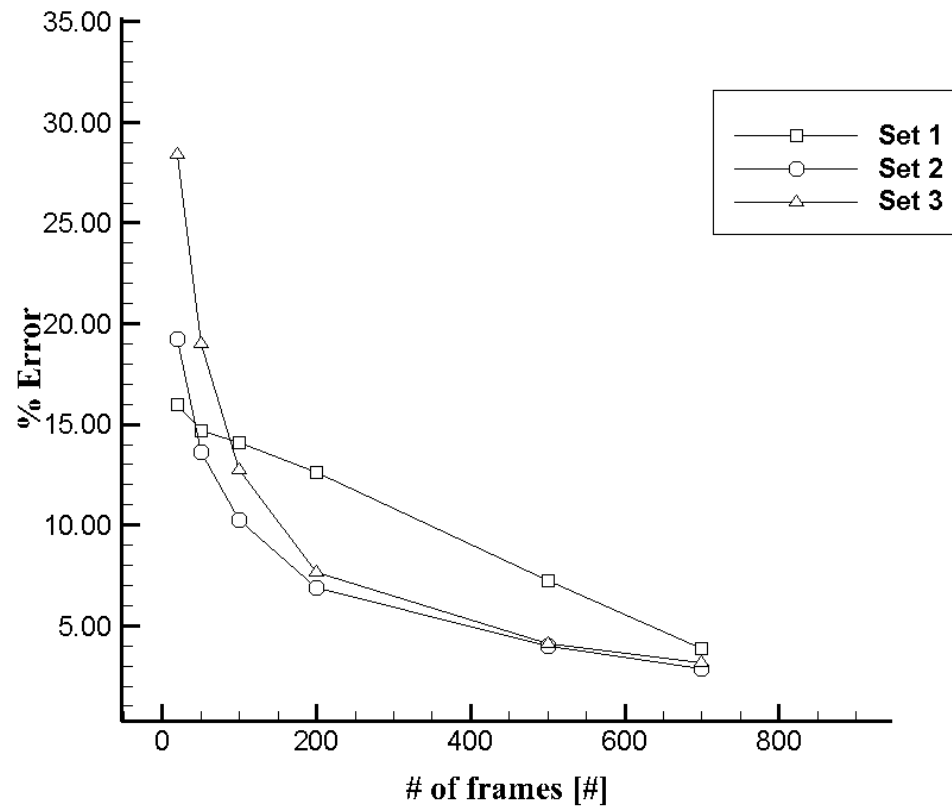


Figure 4-8: Percent error of Y- velocity field for different numbers of image pairs

To further analyze the discrepancies between the sets, lines of data were extracted at different distances from the outlet depicted in Figure 4-9. The sensitivity analysis at the closest slice in Figure 4-10 shows near the outlet pipe a smaller batch of frames can still be representative of the flow.



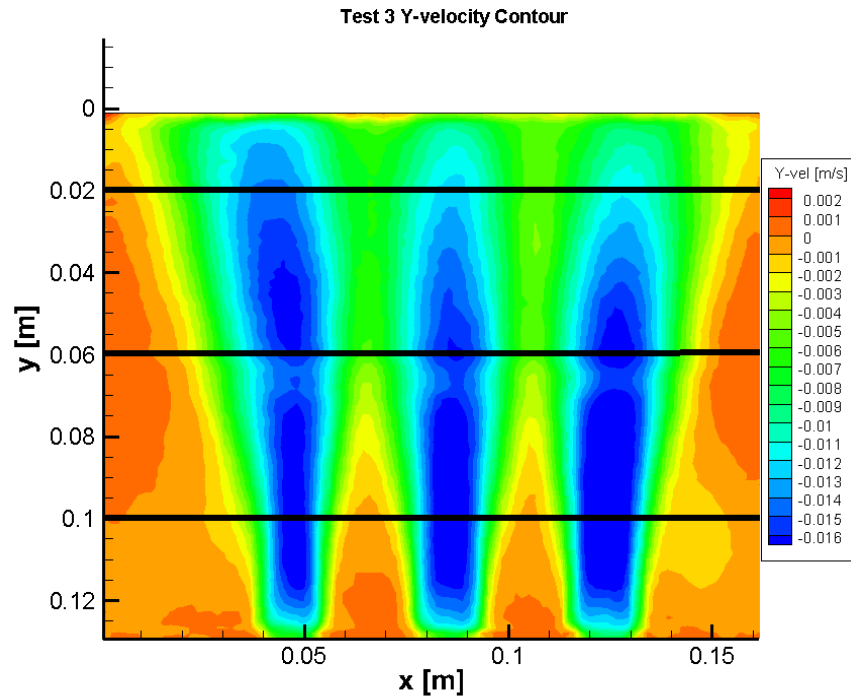


Figure 4-9: Line extraction locations for sensitivity analysis

As the flow goes further from the pipe there is a more significant difference between the frame counts. The extracted data from Figure 4-11 shows that 500 and 700 frames still follow the curve closely and would be sufficient to represent the steady state flow. However the data in Figure 4-12 shows that at about 11 centimeters from the outlet there is a significant difference between 700 and 1000 frames. This suggests that 1000 frames may not be sufficient to correctly model the fluid flow when benchmarking data far from the outlet, and would have to be tested by using more



frames. Additionally the peaks and valleys begin to merge suggesting they will eventually become indiscernible and the flow would consist purely of turbulent eddies. The sensitivity analysis was performed for the other sets and shows similar behavior as set 2, the figures may be found in the appendix.

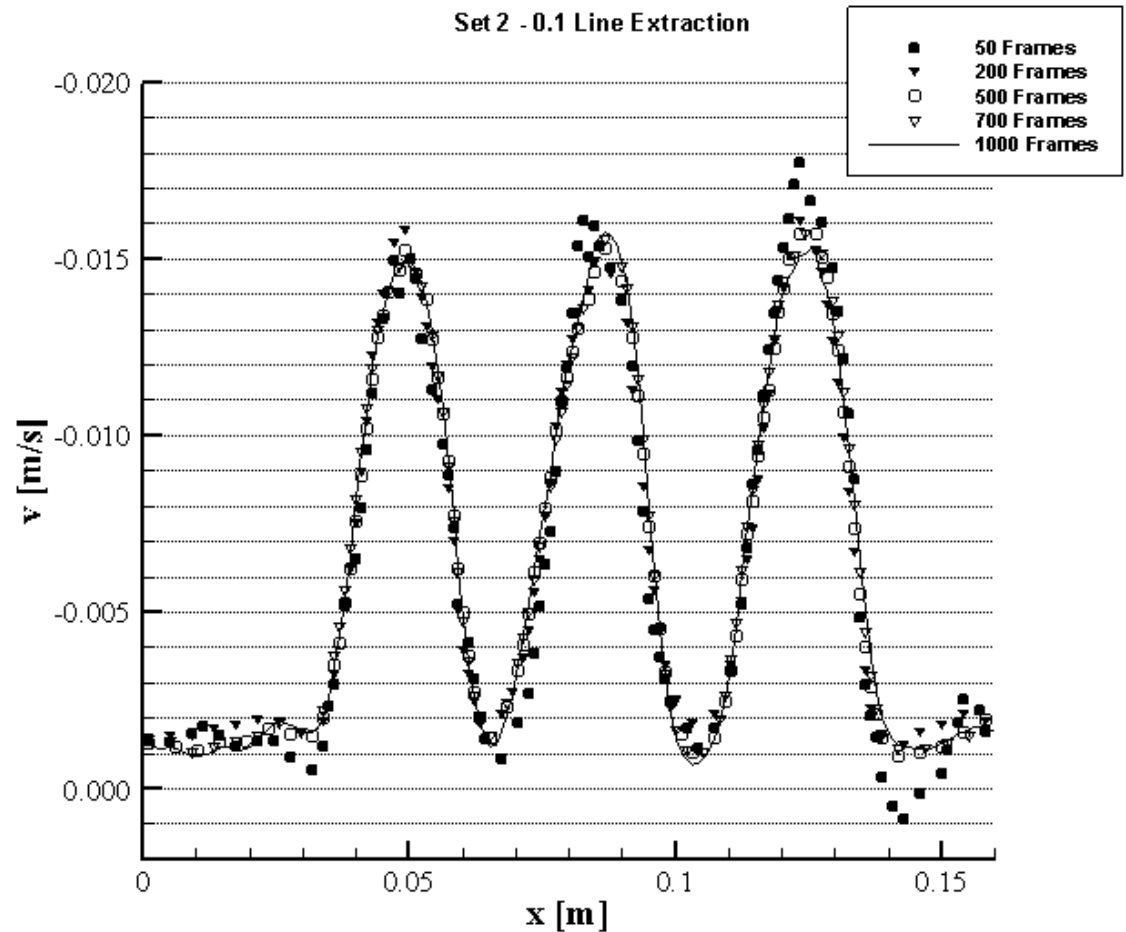


Figure 4-10: Sensitivity analysis for set 2 - 0.1m line

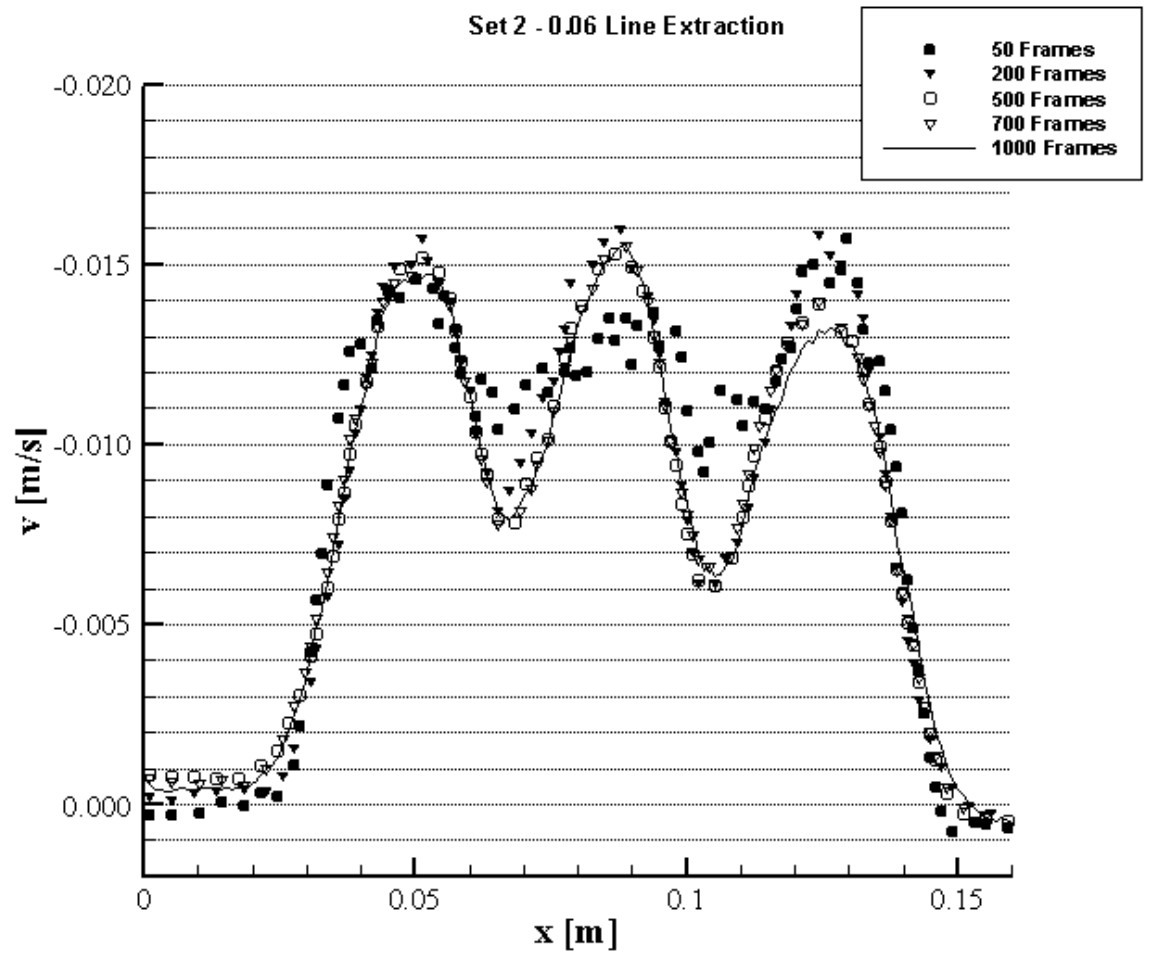


Figure 4-11: Sensitivity analysis for set 2 - 0.06 m line

Repeatability is important for testing to be valid. Test results in general will never perfectly match. For this test facility repeatability error could be due to multiple issues; the water being pumped through the cooling jacket may be colder one test

than the other, or the ambient temperature may vary. As long as the tests are close the results can be compared. However the larger the deviation between the tests the lower the accuracy of the benchmark values the tests would produce. To evaluate the repeatability, RMS was calculated for the Y-velocity line extraction at 0.1 m for all three tests. This value is representative of the error. This was then plotted with the velocity as the error bar in Figure 4-13. The error at the peaks range from 9-12% which isn't optimal but sufficient to state the tests are repeatable. From the sensitivity analysis set 1 has shown to have more error due to the poor particle density. With more tests the repeatability error should decrease.

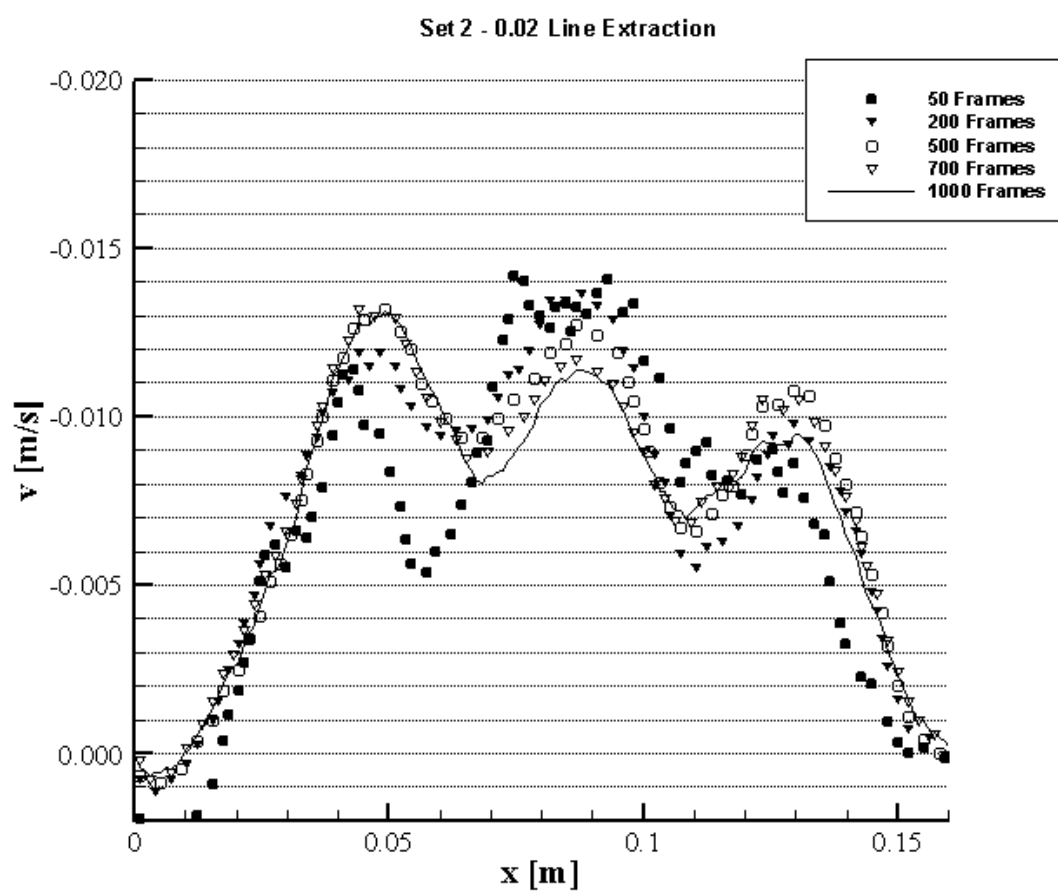


Figure 4-12: Sensitivity Analysis for set 2 - 0.02 m line

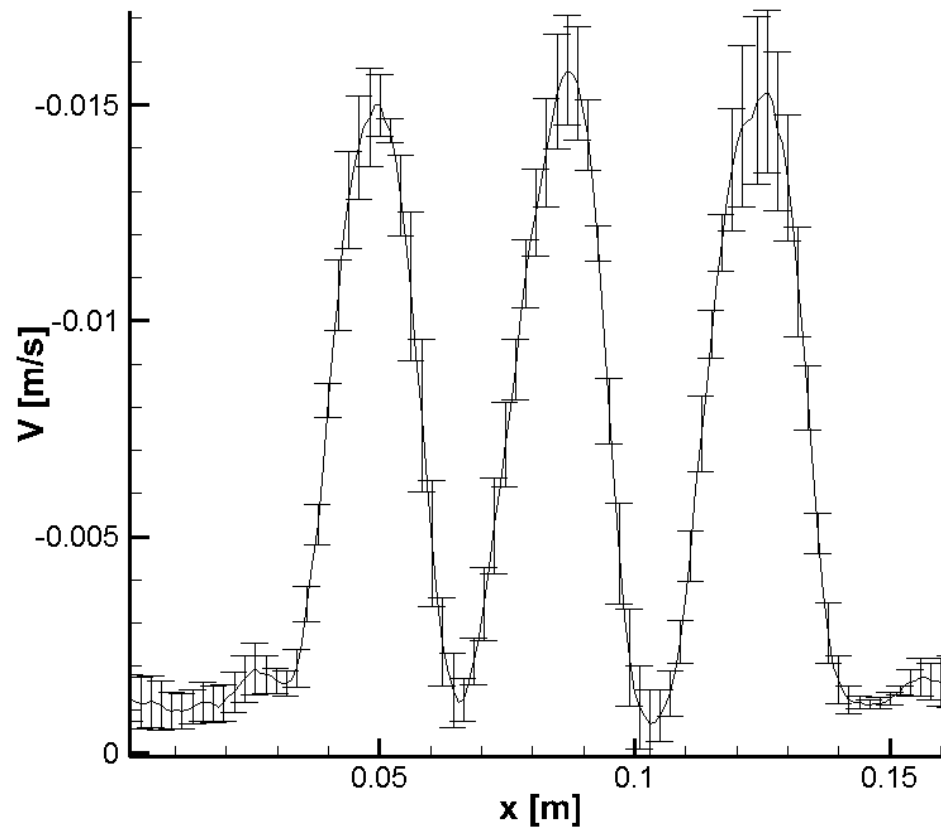


Figure 4-13: Repeatability

The pipe flow in the core piping is laminar with a Reynolds number around 200. However when it enters the upper plenum and the jets interact the fluid likely turns turbulent, but how turbulent. Turbulence intensity (TI) is a useful indicator for predicting how turbulent the flow is. Turbulence intensity is the standard deviation of the velocity fluctuation divided by the average velocity over the same time period. To test this when the line data was extracted the standard deviation of the velocity fluctuations was

also calculated, shown in Figure 4-14. At the peak velocities the deviation was approximately 40% of the averaged velocity, so  $TI=0.4$ . This means the flow becomes turbulent despite being laminar in the core piping. As the jets continue to mix the TI increases to 46% at 11 cm from the outlet.

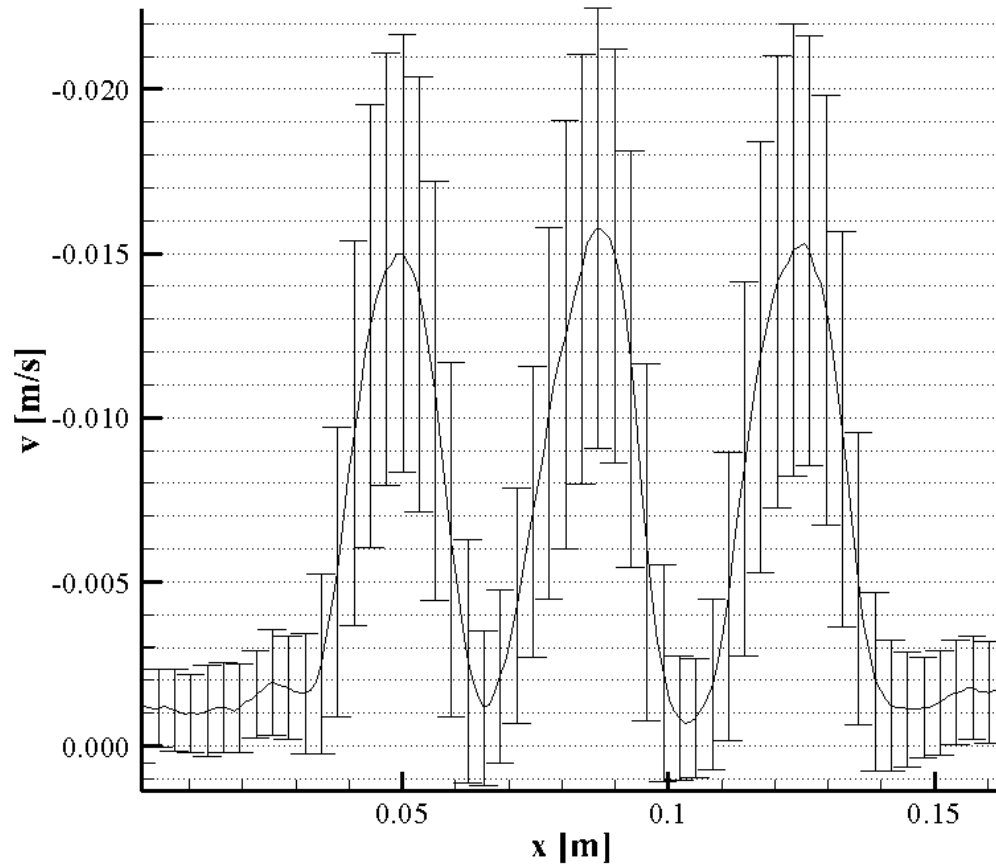


Figure 4-14: Standard deviation of turbulent velocity fluctuations for set 2 at  $Y=0.1\text{m}$ .

In order for the PIV results to be trusted they must be validated. This can be done both by calculation and experimentally. The flow rate of a single pipe may be calculated using,

$$Q = \dot{m}c_p\Delta T \rightarrow \dot{m} = \frac{Q}{c_p\Delta T} \quad (4.2)$$

In this equation  $Q$  is the heat input (Watts),  $\dot{m}$  is the mass flow rate (kg/s),  $c_p$  is the specific heat (J/K), and  $\Delta T$  is the temperature rise in the core piping (K). The accuracy of this value is determined by the accuracy of the thermocouples. The ultrasonic flow rate is the averaged flow rate from the flowmeter over the time the images were being taken, and then divided by five to account for the flow rate of a single pipe. For the PIV flow rate the velocity data at the outlet for all three pipes in the velocity contour was extracted. Then the mean of these averages was used as the average velocity for the outlets of the pipes. Using the average velocity for the outlets of the pipes flow rate could be determined by the equation  $\dot{m} = v\rho A$ . Because the velocity immediately above the outlet in the PIV velocity contour is false, the data was extracted slightly above the outlet once the flow profile was fully developed. The error was calculated for all three methods to determine if the measurements were within the error range of each other. As shown in Figure 4-15 these values match each other closely, the largest difference is between the calculated flow rate and the PIV flow rate in test one, which differ by 8%, however test 1 has shown to possibly be unreliable. Overall this is sufficient to validate the PIV results.

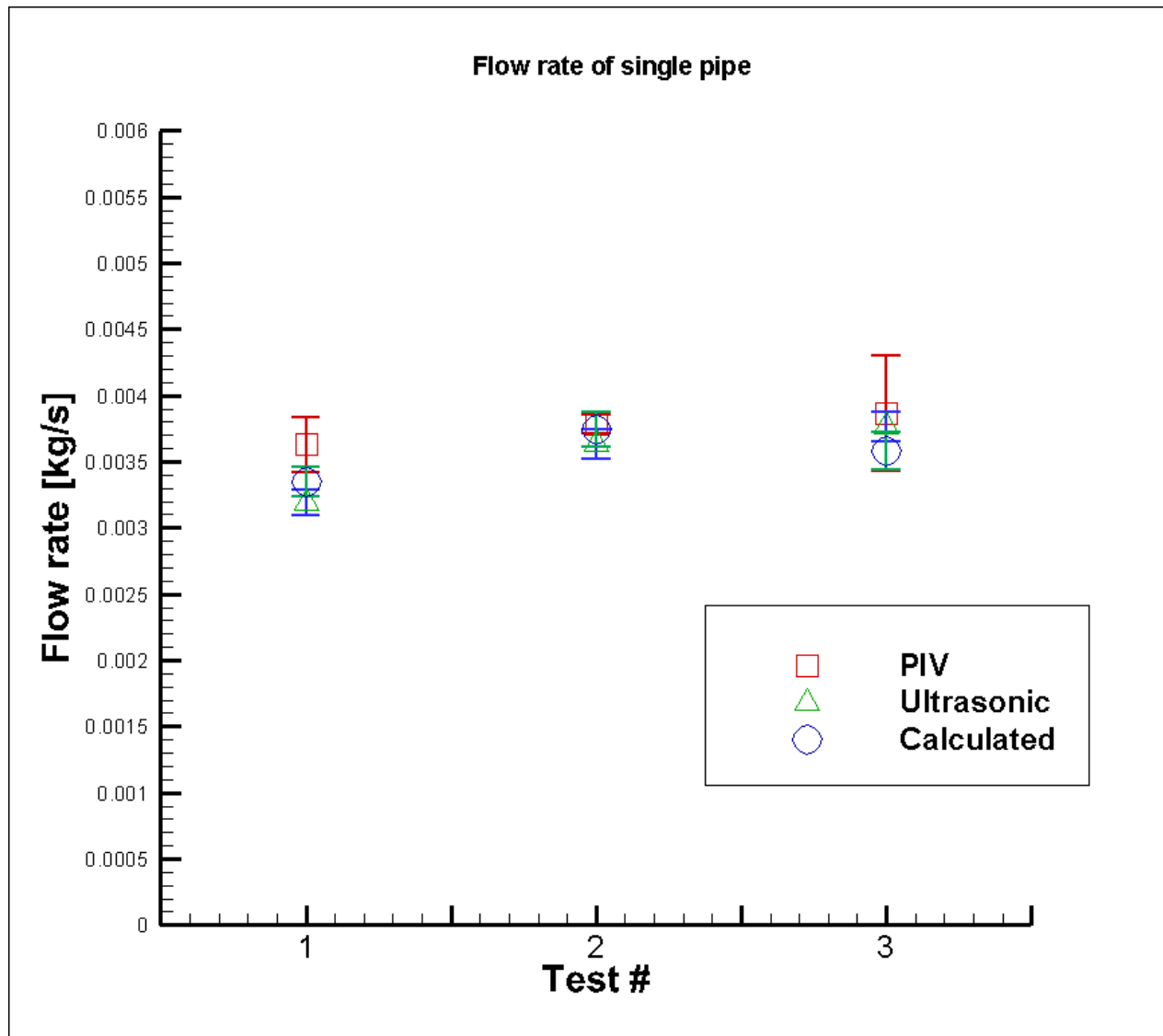


Figure 4-15: Flow rates for single pipe with different methods

For the ultrasonic flowmeter the error was matched to the electromagnetic flowmeter, which is 3%. The PIV error was calculated from the standard deviation of the average velocity of the three jets. The error for the calculated flow rate



comes from the error in the thermocouples. The error caused by the thermocouples in equation 4.2 may be calculated using equations 4.3 and 4.4.

$$\xi_{\dot{m}} = \sqrt{\left(\frac{d\dot{m}}{dT_i}\right)^2 \sigma_{T_i}^2 + \left(\frac{d\dot{m}}{dT_o}\right)^2 \sigma_{T_o}^2} \quad (4.3)$$

$$\xi_{\dot{m}} = \sqrt{\left(\frac{Q}{c_p} \frac{1}{(T_o - T_i)^2}\right)^2 0.5^2 + \left(\frac{Q}{c_p} \frac{1}{(T_o - T_i)^2}\right)^2 0.5^2} \quad (4.4)$$

#### 4.4 Computer Fluid Dynamics Modeling

The endgoal of this experiment is to supply benchmark data that may be used to validate CFD models. To properly design the facility and run tests that would sufficiently produce benchmark data an understanding of CFD is necessary. To accomplish this a Star-ccm+ CFD model was generated that models the fluid region of the experimental test facility. Star-ccm+ uses three continuity equations: mass, momentum, and energy. These equations are evaluated using finite volume discretization. The equations may be solved simulanesously with the coupled energy model, or separately with the segregated energy model. A mesh of the experimental facility has been developed using Star-CCM+ in Figure 4-16. The mesh consists of three regions. The main gas reactor fluid region, the cooling jacket fluid region, and a steel region between them. Interfaces were created for both fluid reagions and the steel section that allows for heat transfer from one region to another. For all regions a polyhedral mesher was used with a prism layer mesher that generates cells a thin layer of cells at the boundaries of the regions. A denser

mesh was used for the gas reactor region, particularly in the upper plenum. The final mesh contains approximately 2.5 million cells.

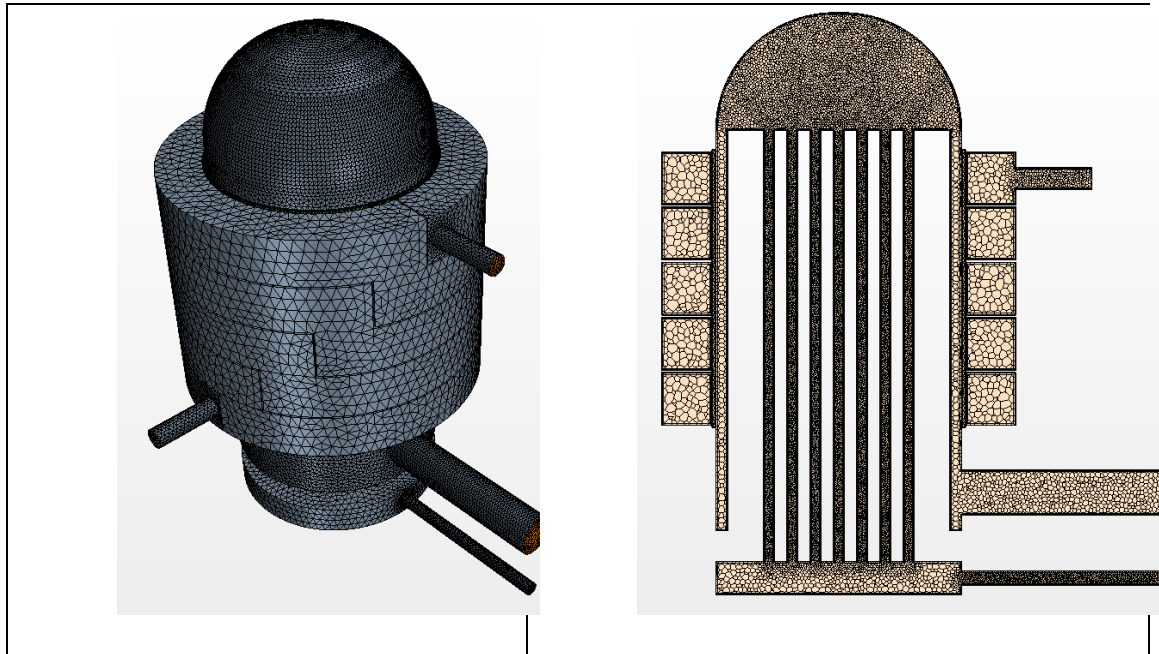


Figure 4-16: Test facility CFD model

For this study the segregated energy model was chosen so the energy equation would be solved separately. For the main loop a laminar model was chosen as the flow rate for the experiment is slow. As this study has shown the flow in the upper plenum is actually turbulent, but once the turbulent fluctuations are averaged out and the statistically steady from the PIV analysis may be similar to the laminar results for cfd modeing. For natural convection the Boussinesq Approximation is applicable, however for a model of this scale applying such an approximation as the driving force for the fluid is challenging and it usually causes the residuals to quickly diverge. Additionally a study has shown that

using the incompressible flow assumption in high heat flux situations may lead to misrepresentative results [26]. Instead boundary conditions were derived from the experimental set up to perform a forced convection simulation with a constant density model. The inlet has a mass flow boundary condition that was taken from one of the pre-calibration ultrasonic flowmeter measurements. A total of 10 kW heat input was evenly distributed on the surfaces of the 25 pipes. The outlet condition was a pressure outlet set to zero.

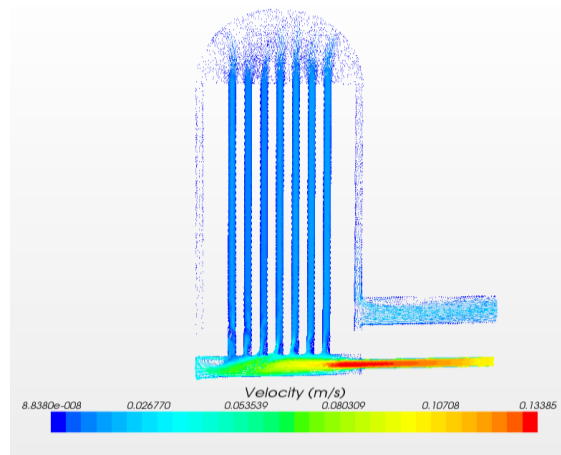


Figure 4-17: Velocity field of gas reactor fluid region

The cooling jacket inlet was set to 10.5 GPM. The physics models were the same as the gas reactor fluid region except a k-epsilon turbulence model was chosen instead of laminar. As stated before the experimental design allows the pipe orientation in respect to the inlet to have either three or seven pipes aligned with the inlet. This determines the number of pipes the symmetric plane would have. The orientation for this simulation is

the opposite of the experimental set up which has seven pipes in the symmetric plane. With these conditions the simulation was run.

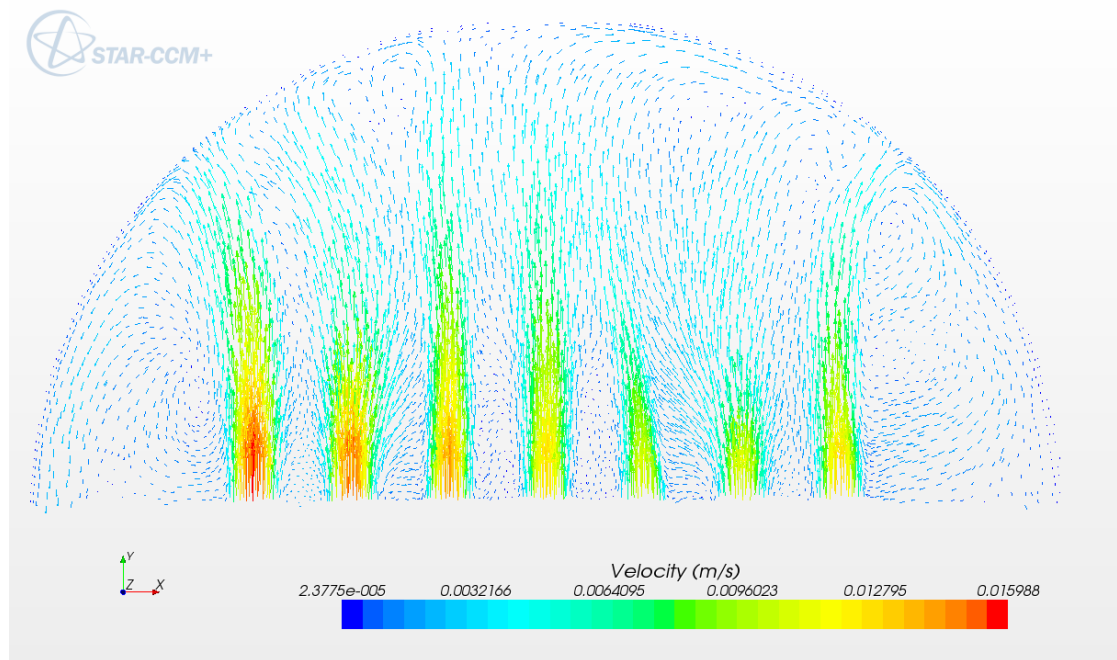


Figure 4-18: Non-symmetric cross section of upper plenum

Figure 4-17 shows the velocity cross section of the gas reactor fluid region. It shows the velocity profile in the lower plenum, however since the inlet has a velocity 25 times greater than the individual core piping, the scaling doesn't reveal much about the velocity behavior in the rest of the model. Figure 4-18 shows the velocity profile of the non-symmetric cross section of the upper plenum. Since the flow is laminar there is little jet to jet interaction, although some eddies are generated between farther from the

inlets. Figure 4-19 shows the symmetric plane of the upper plenum. Apparently the flow isn't perfectly symmetric as the flow in the right jet is stronger than that of the left, suggesting that even though the mass and momentum equations converged the simulation may be misrepresentative of the actual flow profile in the experimental facility.

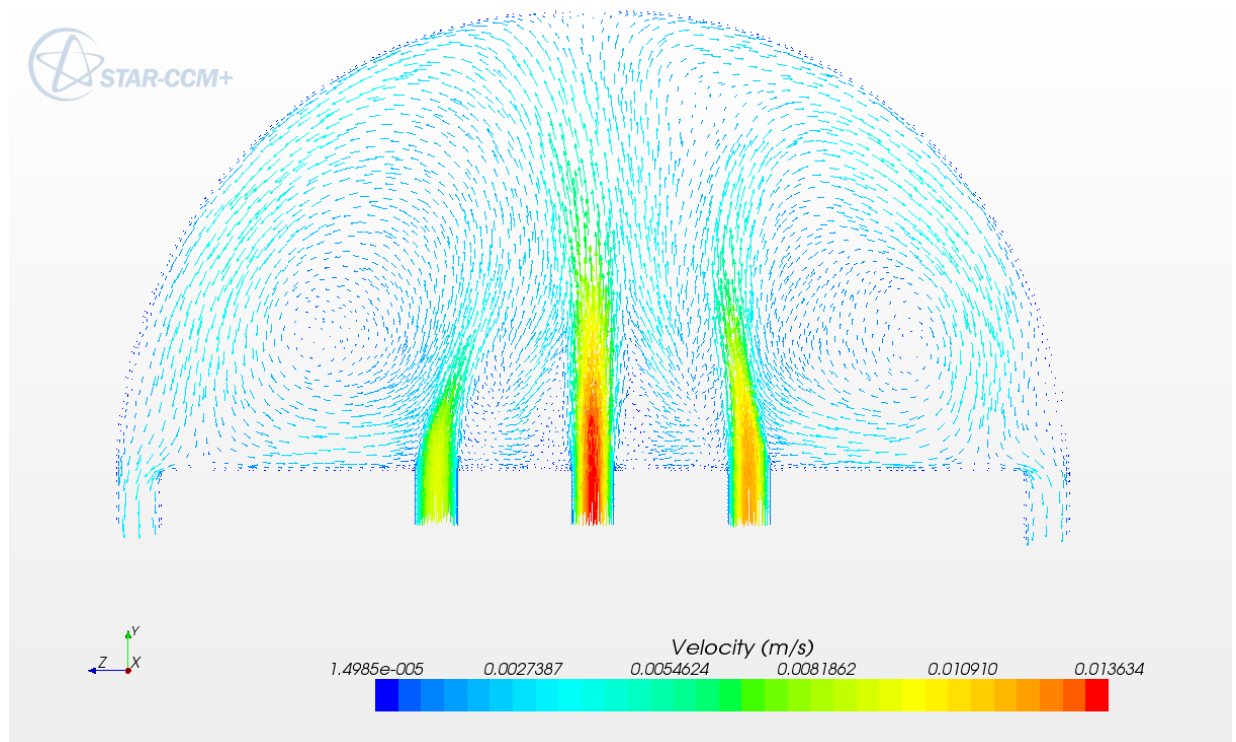


Figure 4-19: Symmetric cross section of upper plenum

The energy equation did not converge. The residuals fluctuated around 0.01. The under-relaxation factor for the fluid was lowered to 0.1 however this did not do much to reduce the energy residual. The model is large and rather ambitious. To properly simulate a much finer mesh is likely needed, perhaps at least five times the cell

count. Another option would be to only model the upper plenum and just use boundary conditions from the experimental facility to the pipe inlet velocity profile. If this does not work a half model upper plenum with a symmetric boundary condition could be modeled. Further research into modeling natural convection is necessary to determine how to model it.

## **5 CONCLUSION AND FUTURE WORK**

### **5.1 Conclusion**

Currently there is no benchmark experimental data to validate CFD codes modeling the upper plenum of a VHTR after a PCC accident scenario. The goal of this study was to build an experimental facility that could fill this deficiency of data. To accomplish this a 1/16<sup>th</sup> scaled geometry from Idaho National Laboratories was incorporated into a design that can model a VHTR under a PCC condition, and allows for proper data acquisition for validation and obtaining benchmark data. The design was then approved and forwarded to the fabricators. Once the parts were machined the experimental facility was then assembled. Problems such as leaks and burnt out heating tapes were encountered, and corrective action was taken until the facility was functional again.

The testing procedure was explained and particle images for PIV analysis as well as other corresponding data that could be used for analyzing a statistically steady state condition for partial operation. Three separate steady state tests were processed using PIVlab to generate the vector fields and exported them to text files. A Matlab code was used to average the varying batch sizes of text files. A sensitivity analysis was performed to determine the number of image pairs needed for the PIV system to obtain benchmarking data. When the flow is close to the jet outlet 500 frames are sufficient, however once the jets start mixing at about twelve centimeters from the outlet at least 700

image pairs are required. This is due to the turbulent behavior of the fluid. After taking the standard deviation of the fluid velocity for 1000 image pairs the turbulence intensity of the jets was approximately 0.4 or 40% of the flow velocity, which increased to 46% at 13 cm from the pipe outlet. Next the repeatability of tests was validated by comparing the standard deviation of the averaged velocity fields between the tests. The relative standard deviation was approximately 10% at the jet peaks but may be reduced if more tests are run. Next the flow rate of a single pipe was measured with three methods: ultrasonic flowmeter, PIV velocity extraction, and calculated using the temperature rise of the core piping. The flow rates matched and will all lie within their error boundary.

A CFD model and simulation was tested to provide insight on proper methods of modeling the experimental facility. Applying the Boussinesq approximation for natural convection to a full scale model of the test facility is unrealistic. A forced convection simulation may be possible if a very large number of cells were used. An easier solution would be to model only the upper plenum and assigning the velocity profiles measured with PIV to the pipe outlets in the upper plenum of the CFD model.

The test facility constructed in this study can produce reliable particle imaging for PIV analysis for natural convective flow. With this benchmark data may be produced for CFD code validation. This includes data modeling the mixing of a select number of natural convective jets, as well as modeling a VHTR during a PCC scenario.



## 5.2 Future Work

First more tests should be run to further evaluate the repeatability. Next the images collected should be processed with different codes, primarily with Particle Tracking Velocimetry. The PIV results were validated using experimental data, but PTV may prove more effective at processing the images than PIV, and if not it would still be beneficial to further validate the PIV results. Also more statistically steady state tests may be run to test the repeatability of the experiment. Next a full scale test may be run with all 25 pipes operating.

Planar laser induced fluorescence (PLIF) is a process used to record the temperature field of a 2-d planar cross section that can be performed simultaneously with PIV. This has great applications for this test facility and can be used to provide benchmark data for CFD code validations. Also more advanced methods exist for measuring the velocity field. Stereoscopic PIV uses multiple cameras to measure all three velocity components of the planar cross section illuminated by the light sheet. And beyond that is topographic mapping that can measure the velocity behavior of a 3D volume.

CFD simulations need to be run and compared to the results of this experiment. This includes the results from this study, as well as the full scale tests. This will determine the quality of benchmark data that the test facility can produce.

The novelty of this test facility is that it has the flexibility to be modified to test different scenarios and configurations the user chooses. It has applications beyond the scope of this study, and will continue to be beneficial to fluid modeling.

## References

1. *Primary Energy Overview*, U.S.D.o. Energy, Editor. 2014, U.S. Energy Information Administration: Washington DC.
2. Nuclear, W., *AP 1000 Brochure*. 2007.
3. Doug Chapin, S.K., Jim Nestell, *The Very High Temperature Reactor: A Technical Summary*. 2004: MPR Associates Inc.
4. Birkhofer, A., *Advanced power reactors with improved safety characteristics*. Applied radiation and isotopes, 1995. **46**(6): p. 701-706.
5. MacDonald, P.E., et al., *The next generation nuclear plant—insights gained from the INEEL point design studies*. INEEL, INEEL/CON-04-01563, 2004.
6. Khamis, I. *Nuclear power plants can produce hydrogen to fuel the “hydrogen economy”*. in *ACS Press Conference*. 2012. San Diego, California: American Chemical Society
7. Ehresman, T., *Very High Temperature Reactor [VHTR]*. 2014, Idaho National Laboratory.
8. Reyes Jr, J., et al., *Scaling analysis for the high temperature Gas Reactor Test Section (GRTS)*. Nuclear Engineering and Design, 2010. **240**(2): p. 397-404.
9. Haque, H., W. Feltes, and G. Brinkmann, *Thermal response of a modular high temperature reactor during passive cooldown under pressurized and depressurized conditions*. Nuclear Engineering and Design, 2006. **236**(5–6): p. 475-484.
10. Schürenkrämer, M., *Theoretische und experimentelle Untersuchungen der Naturkonvektion im Kern des Kugelhaufen-Hochtemperaturreaktors*. 1984, Zentralbibliothek d. Kernforschungsanlage.
11. Tung, Y.-H. and R.W. Johnson. *CFD calculations of natural circulation in a high temperature gas reactor following pressurized circulator shutdown*. in *ASME 2011 International Mechanical Engineering Congress and Exposition*. 2011. American Society of Mechanical Engineers.
12. Tauveron, N., *Thermal fluctuations in the lower plenum of an high temperature reactor*. Nuclear engineering and design, 2003. **222**(2): p. 125-137.
13. Barre, F. and M. Bernard, *The CATHARE code strategy and assessment*. Nuclear engineering and design, 1990. **124**(3): p. 257-284.
14. Chang, H.O., C. Davis, and R. Moore, *Development of Safety Analysis Codes and Experimental Validation for a Very High Temperature Gas-Cooled Reactor*. 2004, Idaho National Laboratory (INL).

15. McCreery, G.E., K.G. Condie, and R.R. Schultz. *Scaled experimental modeling of VHTR plenum flows*. in *Proceedings of the 15th International Conference on Nuclear Engineering (ICONE 15)*, Nagoya, Japan. 2007.
16. Tritton, D.J., *Physical Fluid Dynamics*. 1977, New York: Van Nostrand Reinhold.
17. McCreery, G.E. and K.G. Condie, *Experimental modeling of VHTR plenum flows during normal operation and pressurized conduction cooldown*. 2006, INL/EXT-06-11760, Idaho National Laboratory, Idaho Falls, Idaho 83415.
18. Aldridge, R.J., *Scaling study of the depressurized conduction cooldown event in the high temperature test facility using RELAP5-3D/ATHENA*. 2013.
19. King, B., *Natural Circulation Scaling of a Pressurized Conduction Cooldown Event in the Upper Plenum of the Modular High Temperature Gas Reactor*, in *Nuclear Engineering*. 2012, Oregon State University. p. 78.
20. Jahanmiri, M., *Particle Image Velocimetry: Fundamentals and Its Applications*. 2011, Chalmers University of Technology.
21. Keane, R.D. and R.J. Adrian, *Theory of cross-correlation analysis of PIV images*. Applied scientific research, 1992. **49**(3): p. 191-215.
22. Bastiaans, R.J., *Cross-correlation PIV; theory, implementation and accuracy*. 2000: Eindhoven University of Technology, Faculty of Mechanical Engineering.
23. Meinhart, C.D., S.T. Wereley, and J.G. Santiago, *A PIV algorithm for estimating time-averaged velocity fields*. Journal of Fluids Engineering, 2000. **122**(2): p. 285-289.
24. Nogueira, J., A. Lecuona, and P. Rodriguez, *Data validation, false vectors correction and derived magnitudes calculation on PIV data*. Measurement Science and Technology, 1997. **8**(12): p. 1493.
25. Fukushima, C., L. Aanen, and J. Westerweel, *Investigation of the mixing process in an axisymmetric turbulent jet using PIV and LIF*, in *Laser Techniques for Fluid Mechanics*. 2002, Springer. p. 339-356.
26. Martineau, R.C., et al., *Comparative Analysis of natural convection flows simulated by both the conservation and incompressible forms of the Navier-Stokes equations in a differentially heated square cavity*. in Nucl. Eng. Des, 2009.

## Appendix A    Figures

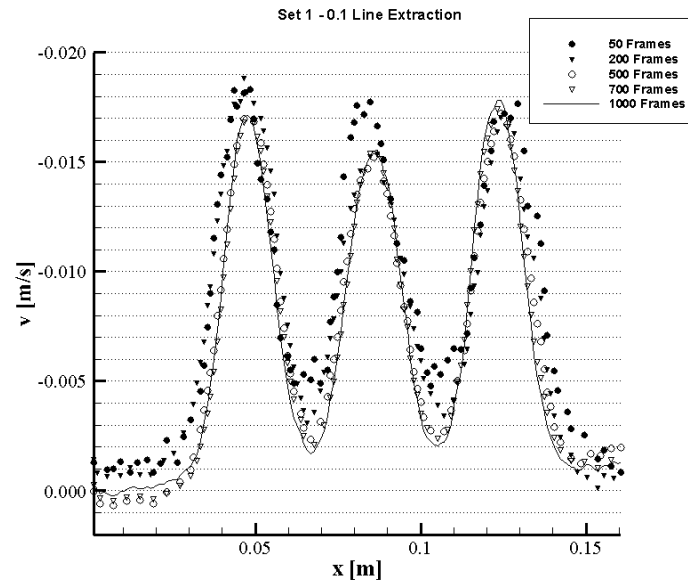


Figure A-1: Sensitivity Analysis for set 1 - 0.1m line extraction

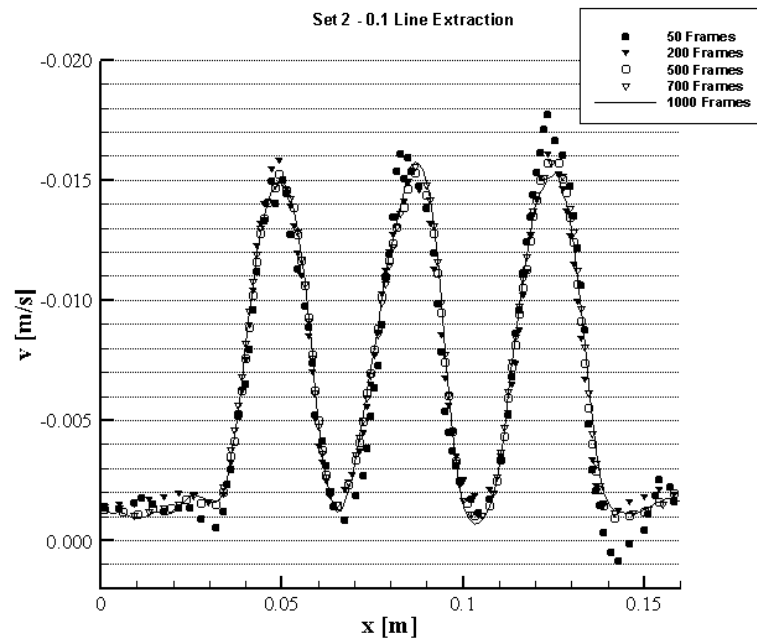


Figure A-2: Sensitivity analysis for set 2 – 0.1 m line extraction

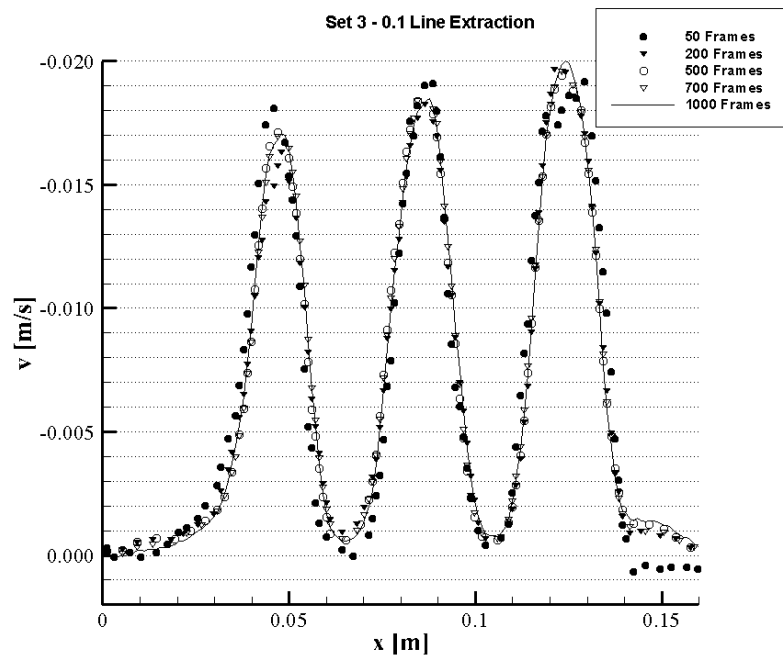


Figure A-3: Sensitivity analysis for set 3 – 0.1 m line extraction

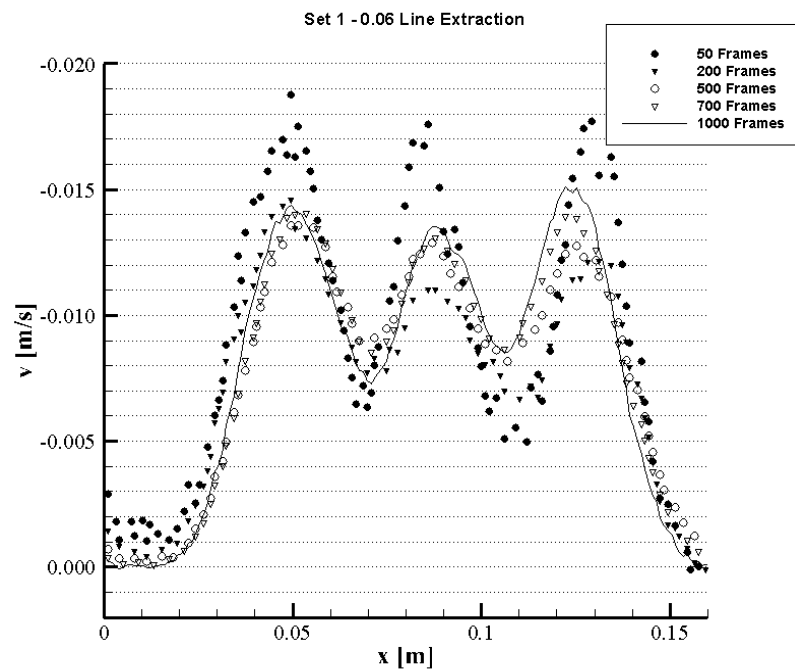


Figure A-4: Sensitivity analysis for set 1 – 0.06 m line extraction



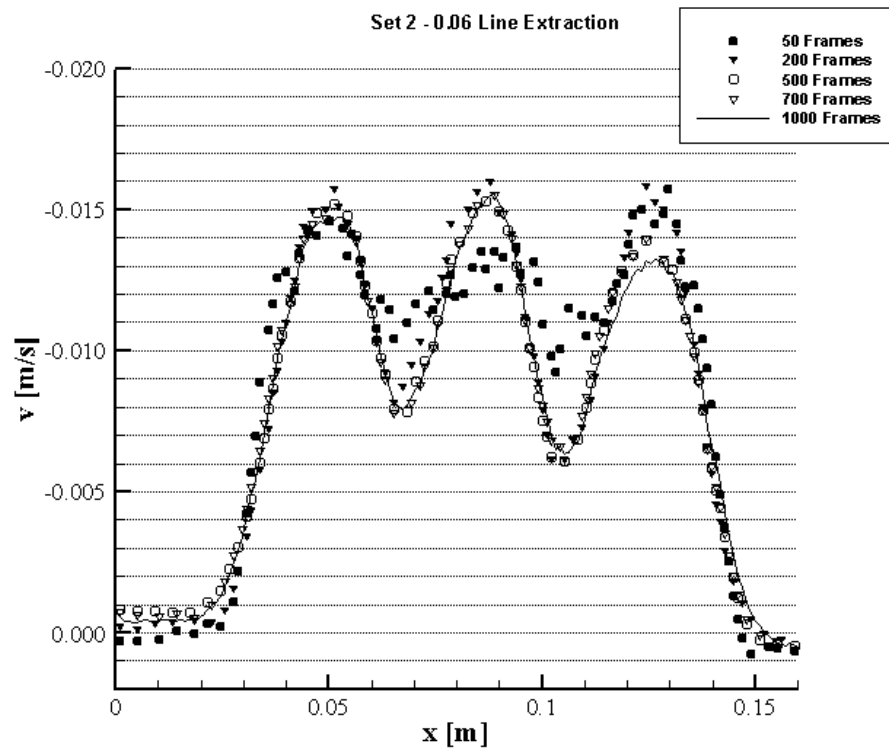


Figure A-5: Sensitivity analysis for set 2 – 0.06 m line extraction

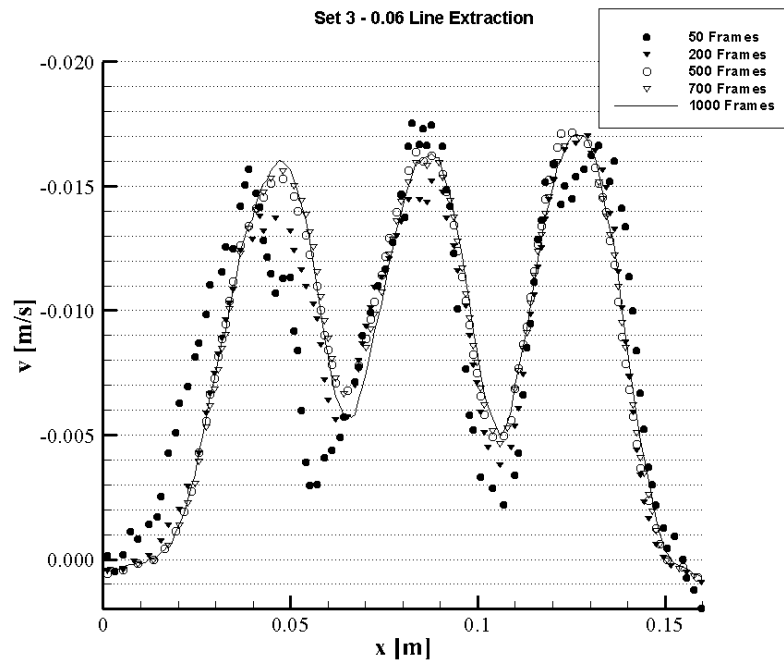


Figure A-6: Sensitivity analysis for set 3 – 0.06 m line extraction

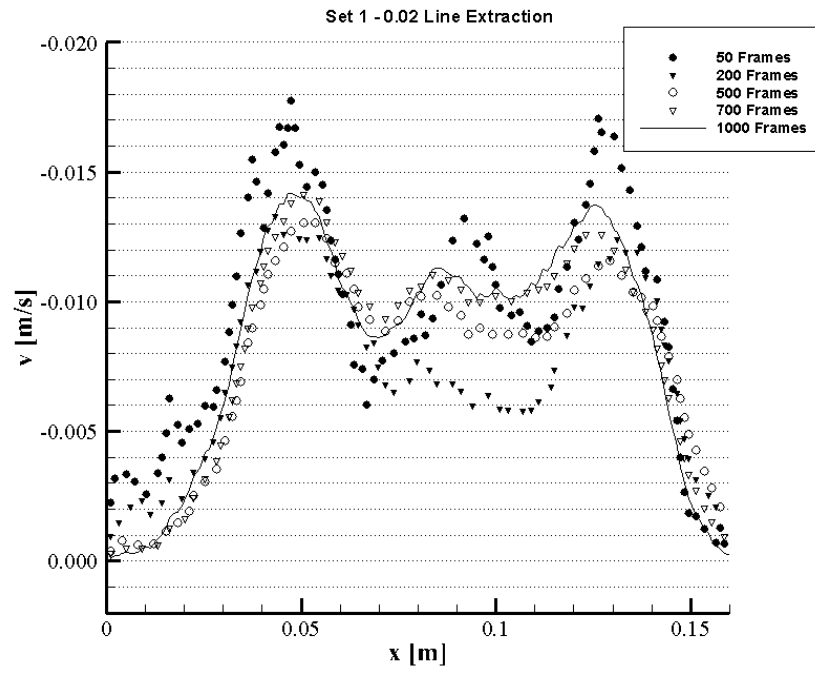


Figure A-7: Sensitivity analysis for set 1 – 0.02 m line extraction

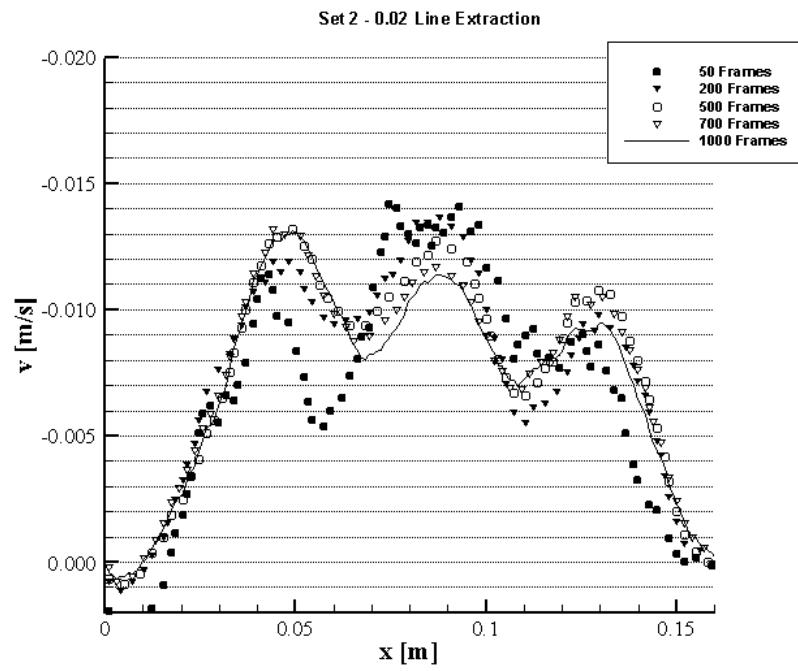


Figure A-8: Sensitivity analysis for set 2 – 0.02 m line extraction

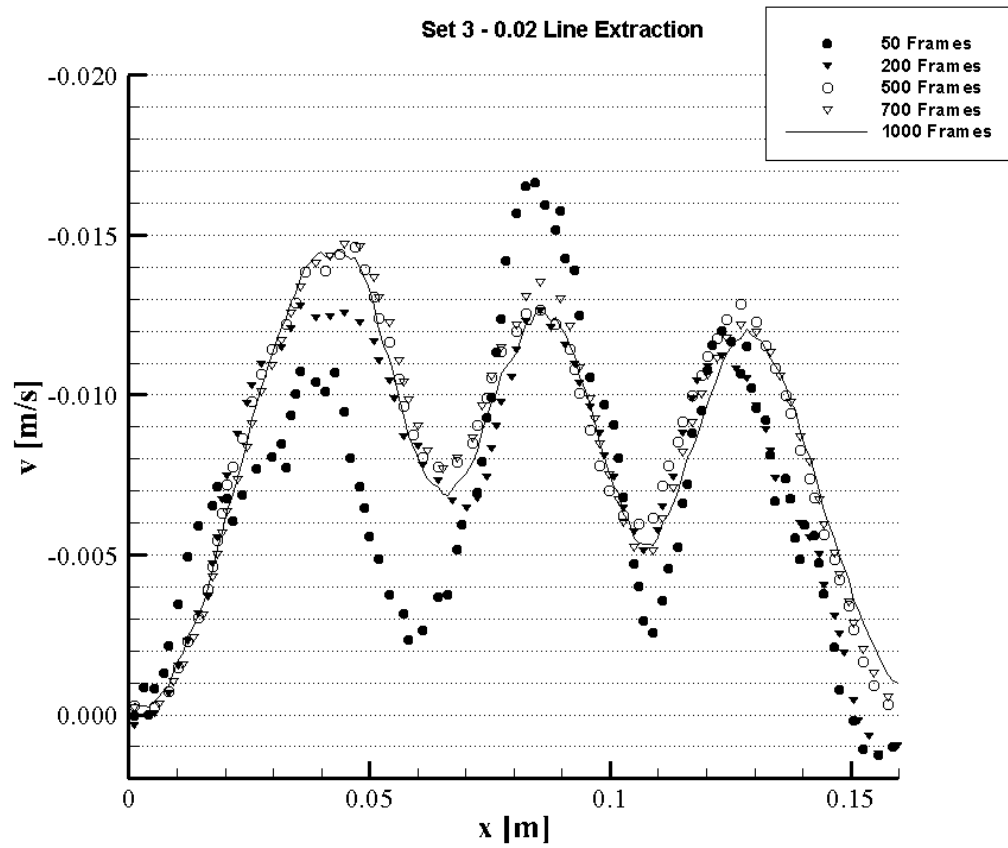


Figure A-9: Sensitivity analysis for set 3 – 0.02 m line extracti





## **ATTACHMENT 1**





